Statistical Estimation of Atmospheric Transmission Parameters

by

Eric Lawrence Miller

S.B., Massachusetts Institute of Technology (1990)

Submitted to the Department of Electrical Engineering and Computer Science
in partial fulfillment of the requirements for the degree of

Masters of Science in Electrical Engineering

at the

MASSACHUSETTS INSTITUTE OF TECHNOLOGY

November 1991

Author .....
Department of Electrical Engineering and Computer Science
November 15, 1991

Certified by .....
Alan S. Willsky
Professor
Thesis Supervisor

Certified by .....
David M. Reilly
Senior Engineering Fellow, Loral Infrared and Imaging Systems
Thesis Supervisor

Accepted by .....
Campbell Searle
Chairman, Departmental Committee on Graduate Students

Statistical Estimation of Atmospheric Transmission Parameters

by

Eric Lawrence Miller

Submitted to the Department of Electrical Engineering and Computer Science
on November 15, 1991, in partial fulfillment of the
requirements for the degree of
Masters of Science in Electrical Engineering

Abstract

Knowledge of the parameters describing the scattering and absorption of radiation propagating through the atmosphere may of practical use in a variety of fields including optical communication, remote sensing, and position/motion detection. The object of this investigation is the construction of mathematical models and algorithms for use in estimating of a vector of atmospheric transmission parameters.

We begin the investigation by defining the operating characteristics of the receiver and transmitter used to generate the data upon which the estimates are based. A multiple wavelength approach is used to take advantage of information on the transmission processes which is available at different frequencies. Subsequently, a single-scatter radiative transfer model is developed to describe the power incident upon the receiver as a function of time for a given transmitted pulse.

This power function gives rise to observed photocounts which are modeled by a Poisson process. The rate function associated with this process encompasses the propagation equation of the single scatter model. Under the assumption that the parameters to be estimated are non-random, the Maximum Likelihood (ML) estimator and associated Cramer-Rao Lower Bound (CRLB) are derived. Next, assuming that the parameters may be modeled as functions of time, a state space model is derived based upon the single scatter propagation equation and the Poisson observation process used with the ML estimator. This model is utilized in the development and evaluation of an Extended Kalman Filter (EKF) for use in estimating the parameters of interest.

Thesis Supervisor: Alan S. Willsky
Title: Professor

Thesis Supervisor: David M. Reilly
Title: Senior Engineering Fellow, Loral Infrared and Imaging Systems

Acknowledgments

I would like to thank my thesis supervisors Professor Alan Willsky and Mr. David Reilly for their guidance and support throughout this project. Mr. Reilly initially formulated the problem to be addressed, but allowed me to pursue its solution in directions of interest to me. Professor Willsky provided immeasurable aid with respect to the myriad of issues surrounding the theory, implementation an analysis of the estimation techniques used throughout this project.

Additionally, I owe special thanks to Mark Luettgen. His wisdom, experience, and patient help were of incalculable assistance to me throughout all stages of this effort.

To my family and Meryl

There is no text material missing here.
Pages have been incorrectly numbered.

Contents

List of Figures

List of Tables

Chapter 1

Introduction

Knowledge of the parameters describing the scattering and absorption of radiation propagating through the atmosphere is of great practical use in a variety of fields. Information regarding these processes can be used to enhance the performance of atmospheric optical communications systems as well as remote sensing systems. The collection of radiation which has been transmitted through the atmosphere can yield information regarding the concentrations of molecular and aerosol pollutants within the medium. Finally, radar and other position and motion detection systems would benefit from an accurate description of the state of the atmosphere.

The object of this investigation is the construction of mathematical models and estimation algorithms for determining a vector of parameters governing the propagation of radiation through the atmosphere. It is felt that useful estimates must deviate by no more than 20% from the true parameter values. While this work may be undertaken with respect to propagation phenomena in most any spectral region, for the purposes of this thesis, we restrict attention to an atmospheric monitoring system operating in the middle ultraviolet region of the spectrum. The near total absorption of solar radiation in this region by the earth's ozone layer means that very low background noise conditions exist. Thus, optical communications systems employing a middle UV channel have been explored by Reilly [43], Sperry [51], Linnell

[28], and Luettgen [27]. Furthermore, the spectral characteristics of species such as ozone, nitrogen dioxide, and sulfur dioxide in the middle ultraviolet make possible the use of pollution monitoring systems operating in this region of the spectrum [13]. Finally, the low background noise property of the middle ultraviolet provides an ideal setting for exploring the feasibility of the estimation techniques developed here in that additional noise sources would only act to degrade the performance of the estimators.

The transmitter/receiver of interest in this investigation is different from the lidar systems commonly used to probe the atmosphere. Lidar systems employ coherent sources and complex optical receivers to determine the structure of the atmosphere at distances of up to 40 km from the source [36]. Furthermore, the data analysis algorithms are based on inversion methods of the lidar equation [25, 36]. The algorithms to be used in this thesis assume a portable, monostatic atmospheric monitoring system composed of a low power, incoherent source capable of emitting pulses at multiple wavelengths and a low-noise, direct detection receiver responsible for converting the optical data (i.e backscattered photons) into electrical signal useful for computing the estimates. Under these assumptions, it is shown that determination of atmospheric transmission parameters to within 20% accuracy for regions close to the transmitter/receiver may be obtained through the use of classical statistical estimation procedures.

The parameters to be estimated in this investigation characterize the scattering and absorption processes distinctive of middle ultraviolet atmospheric radiative transfer. The first parameter of interest is the aerosol scattering coefficient, k_{sa} , which is used to describe the magnitude of scattering events associated with relatively large atmospheric constituents such as dust and hydroscopic particles. The second parameter is the ozone number density, N_{O_3} , which is a measure of the percentage of O_3 present in the atmosphere. This quantity is important in accounting for the absorption of middle ultraviolet radiation as it traverses the atmosphere.

The spectral characteristics of the scattering and absorption processes of interest

suggest that different information concerning the state of the atmosphere is available based upon the wavelength associated with the transmitted pulse. Specifically, the ozone absorption process displays a strong wavelength dependence while aerosol scattering is relatively independent of the wavelength of the transmitted pulse. Thus, pulses whose wavelength lie outside of the ozone absorption band do not suffer significant attenuation due to molecular absorption. Instead, they are impacted most heavily by aerosol scattering. Thus, data collected from pulses whose wavelength is out of the ozone absorption band should be most useful in ascertaining k_{sa} . Alternatively, the effect of ozone absorption is most prominent when the wavelength of the probing pulse is in the ozone absorption band. Even here, the available information is affected by the aerosol scattering process thereby creating a certain degree of coupling associated with separating the effects of ozone from those of the aerosol. To alleviate this problem as well as take advantage of the information available at different frequencies, estimates of the atmospheric transmission parameters are based upon observed backscatter corresponding to multiple wavelengths. Specifically, it is assumed that the transmitter is capable of emitting pulses at two wavelength: an in-band wavelength, λ_{in} , and an out-of-band wavelength,λ_{out} .

This thesis is organized as follows. Chapter 2 is devoted to the derivation of the atmospheric propagation model to be employed in the estimation procedures. This model is based on the single scatter model developed by Reilly [43] for a coaxial source/detector geometry and subsequently generalized by Linnell [28] and Luettgen [27]. Given the characteristics of the source, receiver, and intervening medium, the single scatter model allows for the determination of the power incident upon the detector as a function of time under the assumption that radiation traveling from the transmitter to the detector is scattered at most one time. Double, triple, and higher order scattering effects are assumed negligible. Because of the monostatic arrangement of the source and receiver, the mathematical structure of the propagation equation in this thesis differs from those obtained by Reilly; however, the motivation

behind each step in the construction of the model is identical to that found in [44].

In Chapter 3, the estimation algorithms to be used in this thesis are presented. The chapter opens with a brief review of those elements of probability, stochastic processes, and statistical estimation theory relevant to the remainder of the thesis. Subsequently, it is shown that the power incident on the direct detection receiver gives rise to photocounts which are modeled by a Poisson process where the rate function associated with this process encompasses the propagation equations derived in Chapter 2. Under the assumption that the parameters to be estimated are deterministic, the Maximum Likelihood (ML) estimator and associated Cramer-Rao Lower Bound (CRLB) are derived.

In Chapter 4, the performance of the ML estimator is analyzed. While the equations of Chapter 2 provide the structure for the propagation model, they provide no indication as to realistic values for the many auxiliary parameters associated with the transmitter/receiver system under investigation. Thus, the first portion of this chapter is devoted to a determination of these quantities such that (1) the specifications associated with the system are met and (2) the single scatter assumption upon which the propagation model is based is not violated. Once a base configuration of the auxiliary parameter set is determined, the performance of the ML estimator is examined in two ways. First, the matrix CRLB on the variances and covariance of an unbiased estimator is presented. Additionally, Monte Carlo simulations are used to obtain "real" bias, variance, and mean square error information. This data indicates that the ML scheme easily can meet the 20% desired accuracy in the estimates for most points of interest in the $N_{O3} - k_{sa}$ plane. For both N_{O_3} and k_{sa} , the bias is under 10% and the Cramer Rao bound provides an excellent indication as to actual root mean square error behavior. Second, elements of the auxiliary parameter set are varied from their base values to explore the manner in which the estimator's performance is affected by deviations from the the initial parameter configuration. It is shown that lengthening the interval over which photons are collected and increasing

the power in the pulse serve to improve the performance of the estimator over the base case. The one drawback to the ML estimation technique is its sensitivity to modeling errors. Even small errors in assumed values for the auxiliary parameter set cause large degradation in the estimator's performance. Adequate behavior is only regained through a configuration of the auxiliary parameters which may violate the single scatter assumption present in the underlying propagation model. Further work is needed here before strong conclusions may be drawn.

Recursive estimation of the k_{sa} and N_{O_3} is the subject of Chapter 5. The assumption that N_{O_3} and k_{sa} are constants is replaced by the supposition that their values are time varying. Thus, the Maximum Likelihood estimator of Chapter 4 is replaced by an Extended Kalman Filter (EKF). In the first portion of this chapter, a state space model necessary for implementing the EKF is constructed. The temporal variations of N_{O_3} and k_{sa} are modeled as first order Gauss-Markov processes while the measurement process is based heavily upon the photodetection theory from Section 3.3. Second, the mechanics of the filtering algorithm are briefly discussed. Derivation of this algorithm is not presented here but may be found in [12, 61]. Finally, the performance of the EKF algorithm is examined. It is shown that the response time of the filter to abrupt changes in the parameters can be made rather fast without violating any modeling or systemic restrictions. Furthermore, in steady state situations where the parameters assumed constant values, the error in the filter was consistently less than 20%. Lastly, from a computational standpoint, the EKF was less intensive than the ML estimator and produced comparable if not better results.

Finally, in Chapter 6, the major conclusions obtained from this investigation are presented and recommendations are made as to further work which may be performed relating to the problem addressed in this thesis.

Chapter 2

An Atmospheric Propagation Model

2.1 Introduction

The general form of the atmospheric propagation problem of interest in this investigation is as follows:
Given:

1. A device to be called the source or transmitter, which is capable of emitting electromagnetic radiation,

2. A second device termed the receiver or detector, which collects electromagnetic radiation,

3. Knowledge of the spatial relationship between the transmitter and receiver,

4. Knowledge of the transmitted signal as a function of time,

5. Knowledge of the intervening medium,

Determine:

The electromagnetic power incident upon the detector as a function of time.

An exact, quantitative solution to this problem is difficult to obtain in general. First, one must be able to describe the operating characteristics of the transmitter and receiver. In the most general case, these models are stochastic in nature [48]. Second, a description of the medium separating the source and the detector must be available to account for effects such as scattering and absorption which may take place as the radiation propagates from the transmitter to the receiver. Because the atmosphere is composed of a spatially inhomogeneous, time varying distribution of particles, a model of the medium is itself nontrivial to construct [23, 17, 56, 21]. Even when the transmitter, receiver, and atmosphere are adequately modeled, an arbitrary geometrical arrangement of the source and detector may make determination of the received power function difficult to determine [27, 44]. Due to the complexity of the problem at hand, solutions are often obtained under a variety of simplifying assumptions and reasonable approximations.

For the purposes of this investigation, the choice of assumptions and approximations is driven by the desire to develop a propagation model appropriate for the overall problem of estimating a set of atmospheric transmission parameters. On the one hand, the model must be of sufficient detail to encompass the parameters to be estimated. On the other hand, the computational complexity associated with the model must be such that the incorporation of the model in conventional estimation techniques allows the estimates to be generated in a timely manner.

The goal of this chapter is the construction of a propagation model which balances the need for detail with the problems of undo complexity. This derivation is presented in three steps. First, the nature of the transmitter/receiver system is discussed. Second, a model for the atmosphere is presented. Finally, the function describing the

power incident upon the detector is derived.

2.2 The Transmitter/Receiver System

As shown in Figure 2-1, the receiver and transmitter are assumed to be co-located with coincident fields of view (i.e. it is a monostatic system). The solid angle field of view of the transmitter is denoted by Ω_T and is related to the half field of view angle, θ_T, by the equation

$$\Omega_T = 2\pi(1 - \cos\theta_T) \tag{2.1}$$

An analogous equation holds for the receiver's solid angle field of view, Ω_R, and half field of view angle, θ_R. The source and detector are assumed to operating in the middle ultraviolet region of the spectrum (170 - 340 nm).

The monostatic assumption is made for two reasons. First, many lidar systems used for atmospheric constituent analysis employ this transmitter/receiver arrangement [36, 52, 3]. Because the system in this investigation is to perform the same task, the monostatic configuration seems reasonable. Secondly, the received power function to be derived under the monostatic assumption is far simpler than would be the case for other arrangements [44, 27]. Once the estimation algorithms are evaluated for this geometry, further work may be pursued to determine if alternate source/detector arrangements offer improved performance.

The middle ultraviolet has been chosen because its unique background characteristics make this spectral region ideally suited to a variety of applications. In most every region of the spectrum, photodetection systems suffer due to background noise generated by the sun. The near total absorption of radiation in this band by the earth's ozone layer means that the middle ultraviolet is essentially noise free. Thus, optical communications systems employing a middle UV channel have been explored in [44, 27]. Furthermore, the spectral characteristics of compounds such as ozone,

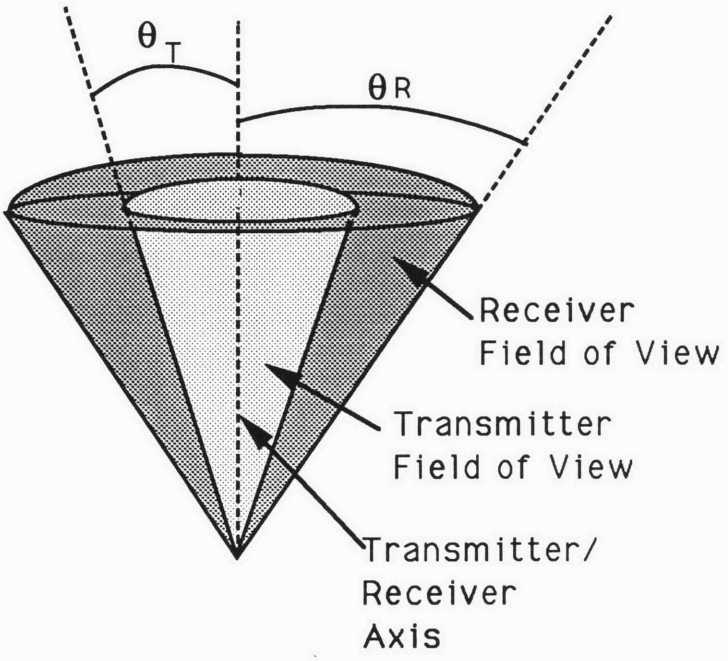

Figure 2-1: Monostatic Transmitter/Receiver Geometry

nitrogen dioxide, and sulfur dioxide in the middle ultraviolet make possible the use of pollution monitoring systems operating in this region of the spectrum [12].

For the purposes of determining the received power as a function of time, the following assumptions are made:

1. The transmitter is capable of emitting incoherent, monochromatic radiation uniformly over its entire field of view. While a rigorous, statistically based definition of incoherency is beyond the scope of this thesis, incoherent radiation is taken as radiation generated by a large number of independent sources. Thus, incandescent and flourescent light are considered incoherent while laser light is not. A more detailed treatment of this topic is found in [47]. The assumption of uniform irradiance over the transmitter's field of view is made to simplify the derivation of the received power function and follows the approach taken in [43] and [26]. Monocromicity is also assumed for the sake of convenience.

2. As shown in Figure 2-2, the transmitted signal is taken to be a rectangular

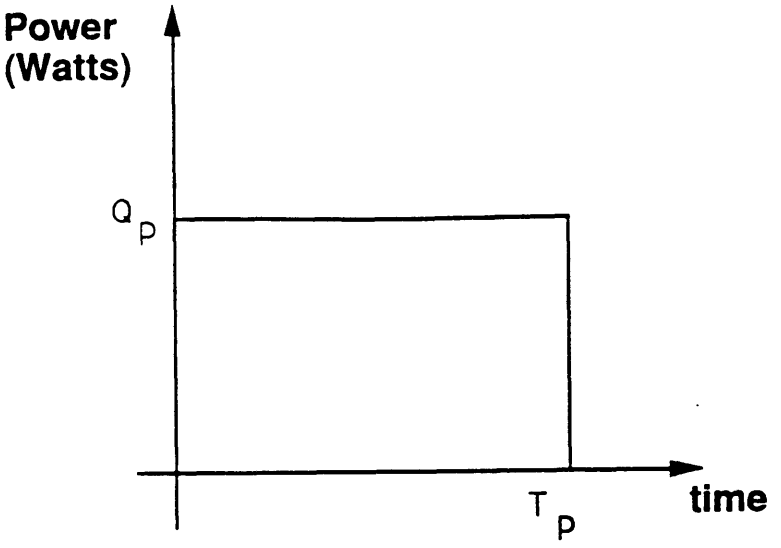

Figure 2-2: Waveform of Transmitted Pulse

pulse of magnitude Q_p Watts and duration T_p seconds. While a more general signal shape is easily incorporated in the model, the rectangular pulse provides the most convenient point at which to begin analysis.

3. The receiver has an angular response function, $a(\theta)$, defined as:

$$a(\theta) = \cos\theta \tag{2.2}$$

where θ is the angle between the incident radiation and the detector's surface normal. This function represents the effective area of the receiver seen by radiation incident at and angle θ.

2.3 Atmospheric Optics: Particles and Processes

Determination of the received power function requires an understanding of the manner in which propagating radiation interacts with the constituents of the atmosphere. Indeed, in the monostatic source/detector geometry described in the preceding section, there exists no direct path from the transmitter to the receiver. The presence

of any received signal requires interaction between the transmitted energy and the atmosphere. Thus, an analytical description of the power present at the detector must include a mathematical model describing atmospheric interaction processes.

A description of these processes is presented in two steps. First, the particulate composition of the atmosphere is discussed. Second, models for the two interaction phenomena of interest in this thesis, scattering and absorption, are constructed.

2.3.1 Atmospheric Particles

In general, the particulate composition of the atmosphere admits no simple description. The concentrations of the constituents is dependent on a wide variety of conditions including altitude above sea level, season of the year, and geographical location [44]. While a universal model for the makeup of the atmosphere is beyond the scope of this investigation, certain general characteristics of this medium are relevant.

The atmosphere is composed of two classes of particles: molecules and aerosols. Molecular constituents include nitrogen, oxygen, water, carbon dioxide, carbon monoxide, nitrogen oxide, and ozone. From Table 2.1, it is evident that nitrogen and oxygen are the most plentiful of these species. The remaining molecular species exist only in trace amounts. From a physical perspective, the most important characteristic of molecules is that their sizes are much less than the wavelength of the radiation of interest in this investigation. This fact plays a major role in describing the manner in which molecules interact with middle ultra-violet radiation.

In contrast to molecules, aerosol sizes are on the order of or greater than UV wavelengths. Typically the mean radius of these particles ranges from $10^{-3}\mu$m to $10^{2}\mu$m. Aerosols include hydroscopic particles, dust, and organic particles. and are found in a variety of sizes and shapes. In practice, it is assumed usually that these particles are spherical and can be described by a size distribution function, $N(r)$. This function specifies the concentration of aerosols (in number of particles per unit volume),

Molecule	Chemical Formula	Number Density (molecules/cm^3)
Nitrogen	N_2	2.10×10^{19}
Oxygen	O_2	5.63×10^{18}
Water Vapor	H_2O	1.17×10^{17}
Carbon Dioxide	CO_2	8.87×10^{15}
Methane	CH_4	4.30×10^{13}
Nitrous Oxide	N_2O	7.28×10^{12}
Carbon Monoxide	CO	2.03×10^{12}
Ozone	O_3	6.70×10^{11}

Table 2.1: U.S. Standard Atmosphere Molecular Constituents at Sea Level [44]

whose radii fall between r and $r + dr$ [44, 57, 33]. For the purposes of this thesis, the structure of $N(r)$ is not of interest. Only the effects on radiative transfer of the aerosols present in the atmosphere are of concern where the mathematical description of these effects does not require knowledge of the underlying size distribution.

2.4 Interaction Processes

The fundamental difficulty in describing the propagation of radiation through the atmosphere arises from the complexity associated with quantifying the manner in which the molecules and aerosols interact with the transmitted energy. In principle, because Maxwell's equations must be satisfied by the propagating electric and magnetic fields, a solution to this set of coupled partial differential equations could be generated as a means of solving this problem. In light of the highly complicated structure of the atmosphere, such an approach is intractable. Furthermore, the level

of detail resulting from such a solution (i.e. knowledge of the fields) is unneeded in the present case. All that is of interest is the power transfered from one point in space to another. A common approach to describing these processes involves solving Maxwell's equations to determine the way in which radiation is affected by a single molecule or a single aerosol particle and then generalizing the result to describe the power transfer process for an agreggation of particles [18, 20].

2.4.1 Scattering

The first interaction process of interest is scattering. Scattering is defined as an event in which a portion of the energy prior to the occurrence is lost and the remainder is spatially redistributed (Figure 2-3). Energy which is lost may have been converted to a different form (heat, rotational, vibrational, etc.), but in any event is unavailable for detection at the receiver. Energy which has not undergone any scattering events is said to be in the primary field while energy which has been scattered one or more times makes up the scattered field.

There are two forms of scattering. For conservative scattering, the wavelength of the incident energy is identical to the wavelength of the scattered energy. In the case of nonconservative (also called Raman) scattering, the wavelength of the radiation is changed as a result of the scattering event. For the purposes of this thesis, only conservative scattering is of concern. The effects of Raman scattering are ignored.

The scattering process is characterized by two quantities: the scattering coefficient and the scattering phase function. The scattering coefficient determines the quantity of radiation which is redistributed rather than lost and is defined as:

$$k_s = k_{sa} + k_{sm} \tag{2.3}$$

where

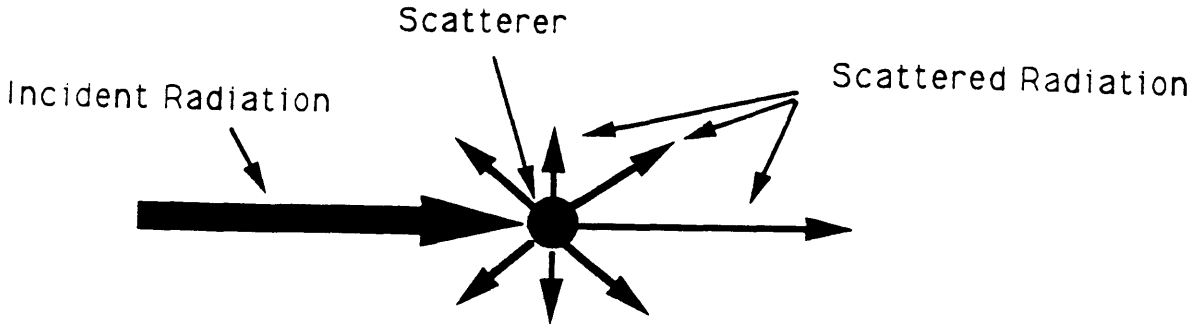

Figure 2-3: A Scattering Event

k_s is the overall scattering coefficient

k_{sa} is the scattering coefficient due to all aerosol components in the atmosphere

k_{sm} is the scattering coefficient due to all molecular components in the atmosphere

In the general case of an inhomogeneous atmosphere, k_s is a function of position. It is assumed for the remainder of this thesis that the distance the radiation travels from the source to the detector are short enough to approximate the atmosphere as homogeneous (see Section 4.2.1). Hence, k_s is merely a constant.

The mathematical structures of k_{sm} and k_{sa} can be obtained through the use of of Maxwell's equations for the single particle case and appropriately generalized for the multi-particle situation. In the case of molecular scatterers where the size of the particle is much less than the wavelength of interest, Rayleigh theory describes the scattering process. Here, k_{sm} is given by [9]:

$$k_{sm} = \frac{8\pi^3(n^2-1)}{3\lambda^4 N_s}\frac{6+3\delta}{6-7\delta} \tag{2.4}$$

where

n is the index of refraction and is assumed to be 1.0003 [9]

λ is the wavelength of the radiation (m)

N_s is the molecular number density (m^{-3}). Following Elterman [9], this quantity is taken as 2.55×10^{25} m^{-3}.

δ is the depolarization factor. For this thesis, $\delta = 0.035$ [9]

The form of k_{sa} can be obtained through the use of Mie scattering theory [18]. The resulting closed form expressions for this quantity are given in [18] but are not of interest here. For the purposes of this investigation, k_{sa} is assumed to be unknown and is estimated. Furthermore, it is supposed that k_{sa} is independent of the wavelength of radiation used in the transmitted pulse. While this assumption is not exactly true, Table 2.2 demonstrates that, relative to k_{sm} and for medium to high visual range[1], the aerosol scattering coefficient is influenced only slightly by wavelength. Thus, to a reasonable approximation, k_{sa} is taken as constant with respect to variations in wavelength across the middle UV.

Table 2.2 also provides an indication as to the range of values for k_{sa} in the middle ultraviolet under medium to high visibility conditions. The minimum value of the aerosol scattering coefficient is 2.8×10^{-4} m^{-1} and the maximum value is 1.6×10^{-3} m^{-1}. In an effort to take into account a wider variety of atmospheric conditions, this bound on k_{sa} is loosened for the remainder of this investigation. Specifically, it is assumed that $k_{sa} \in [0, 3.0 \times 10^{-3}]$ m^{-1}.

While k_s defines the magnitude of the scattering event interaction, the scattering phase function determines the manner in which the scattered radiation is spatially redistributed. This function is denoted by $p(\theta_s)$ where θ_s is the angle between the incident and scattered radiation for a differential volume element dV (Figure 2-4).

[1] Visual range provides an idea of how far one can see under a specific set of atmospheric conditions. A rigorous definition of this quantity may be found in [33].

Wavelength (nm)	k_{sm} (m^{-1})	Visual Range (km)	k_{sa} (m^{-1})
200	9.54×10^{-4}	23	3.2×10^{-4}
		5	1.6×10^{-3}
250	3.38×10^{-4}	23	3.0×10^{-4}
		5	1.5×10^{-3}
300	1.53×10^{-4}	23	2.8×10^{-4}
		5	1.4×10^{-3}

Table 2.2: Rayleigh and Mie Scattering Coefficients as a Function of Wavelength [44]

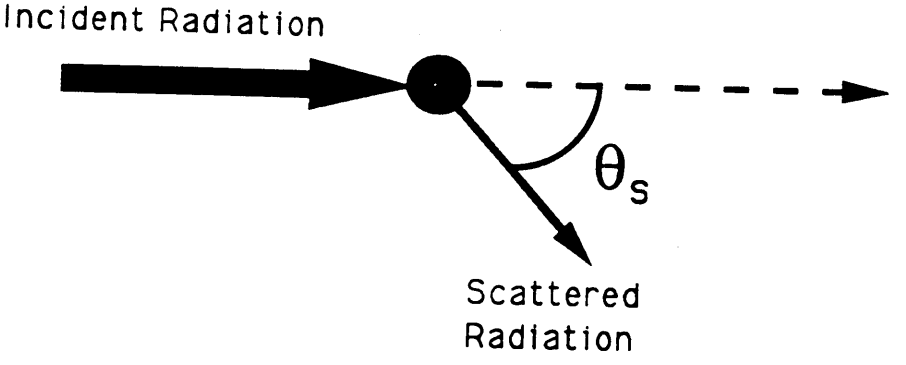

Figure 2-4: Definition of Scattering Angle (θ_s)

The phase function is normalized such that:

$$\frac{1}{4\pi}\int_0^{4\pi} p(\theta_s)d\omega = 1 \tag{2.5}$$

where $d\omega$ is the differential solid angle element having dimension of steradians.

As with the scattering coefficient, the phase function is dependent upon the type of particle under consideration. From Rayleigh theory, the molecular phase function, $p_m(\theta_s)$ is [44]:

$$p_m(\theta_s) = \frac{3}{4}(1 + \cos^2\theta_s) \tag{2.6}$$

Mie theory provides a closed form expression for the aerosol phase function, $p_a(\theta_s)$,

in terms of an infinite sum of Legendre polynomial and Bessel functions [44]. Rather than using these results, a common approximation to this function is made using the Heney-Greenstein function [63, 57]:

$$p_a(\theta_s) = (1-g^2)\left[\frac{1}{(1+g^2+2g\cos(\theta_s))^{3/2}} + f\frac{3\cos^2(\theta_s-1)}{2(1+g^2)^{3/2}}\right] \tag{2.7}$$

where g and f are parameters whose values are chosen based upon the specific atmospheric conditions under investigation.

Finally, the composite phase function is an appropriately weighted and normalized sum of the molecular and aerosol functions. The weighting factors are the corresponding scattering coefficients. To satisfy Equation 2.5, the resulting sum must be multiplied by $(k_{sa}+k_{sm})^{-1}$. Thus:

$$p(\theta_s) = \frac{k_{sa}p_a(\theta_s) + k_{sm}p_m(\theta_s)}{k_{sa}+k_{sm}} \tag{2.8}$$

2.4.2 Absorption

The second interaction process of interest is absorption. An absorption event is defined as one in which a portion of the energy is lost (i.e. transformed in a manner which makes it undetectable by the receiver). This process is characterized by a single quantity, the absorption coefficient, defined as:

$$k_a = k_{aa} + k_{am} \tag{2.9}$$

$$k_{aa} = \sum_i A_i(\lambda)N_i \tag{2.10}$$

$$k_{am} = \sum_j A_j(\lambda)N_j \tag{2.11}$$

$$\tag{2.12}$$

where

k_a is the overall absorption coefficient (m^{-1}).

k_{aa} is the absorption coefficient due to all aerosol species in the atmosphere (m^{-1}).

k_{am} is the absorption coefficient due to all molecular species in the atmosphere (m^{-1}).

$A_i(\lambda)$ is the absorption coefficient (m^{-1}) due to the i^{th} species of aerosol under the assumption that the atmosphere is composed of 100% of that particle and is a function of the wavelength. This notation and definition follows that of Elterman [9].

N_i is the number density of the i^{th} aerosol species. This is a dimensionless quantity representing the percentage of that species which actually exists in the atmosphere.

$A_j(\lambda)$ is the absorption coefficient (m^{-1}) due to the j^{th} species of molecule under the assumption that the atmosphere is composed of 100% of that particle.

N_j is the number density of the j^{th} molecular species.

Other definitions of absorption coefficients in terms of absorption cross sections may be found in [20].

In this investigation it is assumed that significant absorption is attributed to a single species: atmospheric ozone. Figure 2-5 shows that A_{O3} in the middle ultraviolet is strongly dependent upon wavelength. The other factor in the absorption coefficient N_{O_3} , is assumed to be an unknown quantity and, along with k_{sa} forms the vector of parameters to be estimated. Studies of the atmosphere have shown that N_{O_3} tends to lie between 0 and 100 ppb [9, 3].

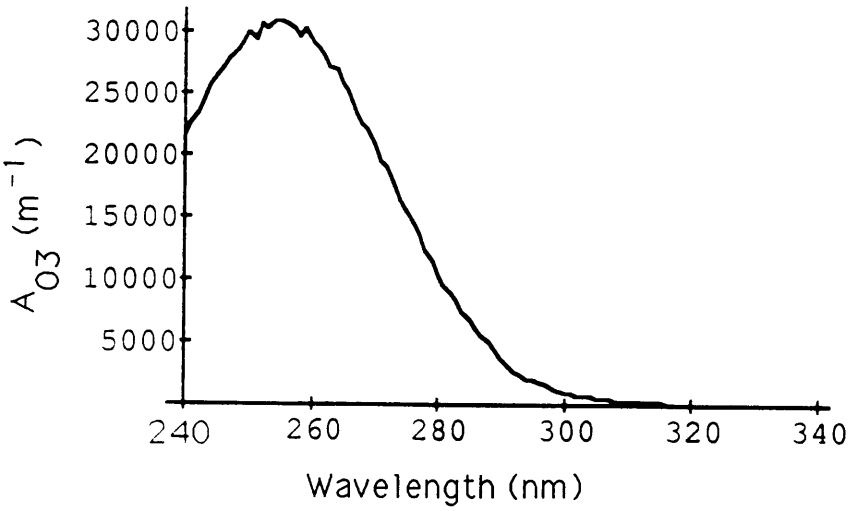

Figure 2-5: A_{O3} Curve As a Function of Wavelength

[18]

2.5 An Atmospheric Propagation Model

Armed with an understanding of both the transmitter/receiver system and the atmospheric interaction processes, a useful model of atmospheric transmission may be constructed. This derivation follows closely that of Reilly [43]. Reilly developed the single scatter model to describe the received power function of a coaxially arranged source and detector under the assumption that on its path from the transmitter to the receiver, the radiation is scattered at most one time. Thus, all collected energy originated from the primary or the once-scattered fields[2]. Under this model, the atmosphere is considered to be a linear time-invariant system. First, the atmospheric impulse response, $h(t)$ is determined (i.e. the power at the receiver when the transmitted waveform is an impulse.) Next the, response to an arbitrary waveform, $P_T(t)$ is obtained by convolving $P_T(t)$ with $h(t)$.

The monostatic geometry of the atmospheric monitoring system allows a spherical

[2]Bounds on the validity of the single scatter assumption are discussed in section 4.2.1

coordinate system to be used. From Figures 2-1 and 2-6 the axis of the transmitter/receiver is taken as the z axis of the coordinate system.

Under the single scatter assumption for a monostatic arrangement, only radiation scattered at an angle of π radians is observed at the detector. From Figure 2-7 any radiation initially scattered at any other angle would require two or more scattering events to reach the receiver and thus is not observed in a single scatter model. Because only backscatter is observed, it is assumed that $\theta_T = \theta_R \equiv \theta_{HFOV}$. If $\theta_T > \theta_R$ then some fraction of the transmitted pulse has no chance of being detected at the receiver and therefore is wasted. Similarly, if $\theta_T < \theta_R$, then a portion of the receiver's field of view is unilluminated. Thus, to take full advantage of the monostatic geometry, the fields of view of both the transmitter and receiver are assumed to be identical with a half field of view angle θ_{HFOV}.

To begin the development of the single scatter model, consider an impulse of energy, $Q_p\delta(t)$, emitted by the transmitter at time $t = 0$, uniformly over its entire field of view, Ω_S. Using the Beer-Lambert Extinction Law for diverging beams [44], the energy density, E_P, at a point P in the transmitter's field of view is:

$$E_P = \frac{Q_p \exp(-k_e r)}{\Omega_S r^2} \quad \frac{\text{Joules}}{\text{square meter}} \tag{2.13}$$

where

k_e is the atmospheric extinction coefficient which is defined as the sum of k_s and k_a.

r is the distance from the transmitter to the point P

A differential volume element, dV surrounding point P can be treated as a secondary source of radiation due to scattering of the primary field which occurs in dV. The quantity of energy, dQ_S, associated with this source is:

$$dQ_S = k_s\, E_P\, dV \quad \text{Joules} \tag{2.14}$$

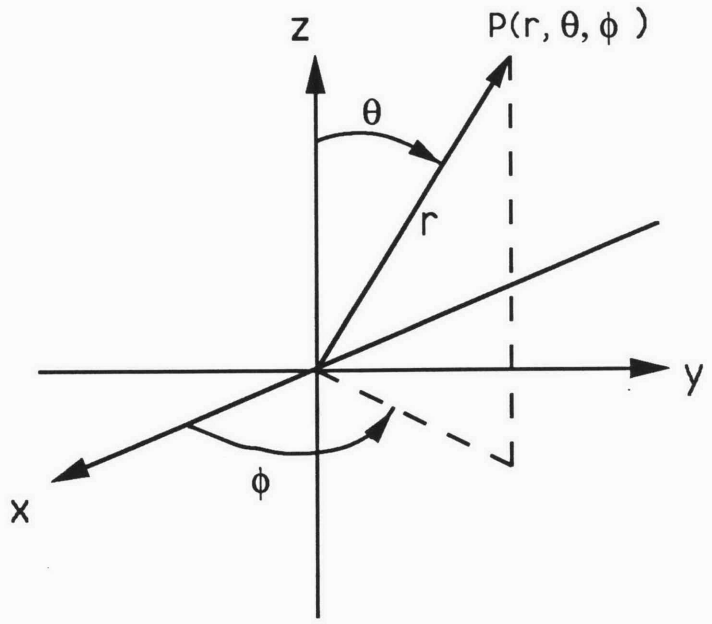

Figure 2-6: Spherical Coordinate System

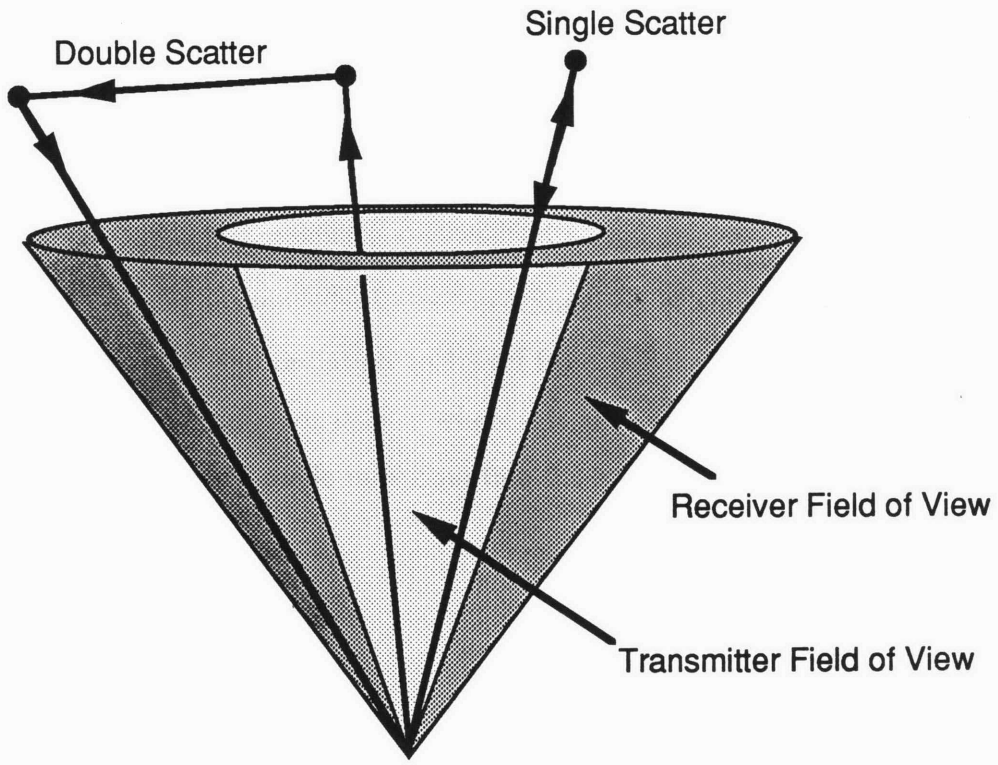

Figure 2-7: Why Only Backscatter is Observed

The spatial redistribution of dQ_S is governed by the scattering phase function given in Equation 2.8. For this volume element, the quantity of backscatter, dQ_{BS}, is given by:

$$dQ_{BS} = dQ_S \frac{p(\theta_s = \pi)}{4\pi} \quad \text{Joules} \tag{2.15}$$

Utilizing the Beer-Lambert law once again allows the energy density at the receiver due to the scattering from dV to be calculated as:

$$dE_R = \frac{dQ_{BS} \exp(-k_e r)}{r^2} \tag{2.16}$$

$$= \frac{Q_p k_s \exp(-2k_e r)}{4\pi\Omega_S r^4} p(\theta_s = \pi)\, dV \quad \frac{\text{Joules}}{\text{square meter}} \tag{2.17}$$

Recognizing that:

1. The differential volume element in spherical coordinates is given by

$$dV = r^2 \sin\theta \, dr \, d\phi \, d\theta \tag{2.18}$$

2. The impulse response is desired as a function of time, not distance. The time, t, it takes for the radiation to travel from the transmitter, to the point P and return to the detector is $2r/c$ where c is the speed of light. Thus, the following substitutions are made into Equation 2.17:

$$r = tc/2 \tag{2.19}$$

$$dr = (c/2)dt \tag{2.20}$$

which allow dE_R to be written as:

$$dE_R = \frac{Q_p k_s \exp(-k_e ct)}{2\pi c\Omega_S t^2} p(\theta_s = \pi) \sin\theta \, d\phi \, d\theta \, dt \quad \frac{\text{Joules}}{\text{square meter}} \tag{2.21}$$

Carrying out the following steps results in the final form for the differential impulse response, $dh(t)$, at the detector:

1. The quantity of interest is not energy density, but power density; thus, divide both sides of Equation 2.21 by dt.

2. Multiply Equation 2.21 by the receiver's angular response function, $\cos\theta$.

3. Under the assumption that the receiver is uniformly illuminated by the backscattered power, multiply dE_R by the area of the receiver, A_R.

4. Substituting the relationship $\Omega_S = 2\pi(1 - \cos\theta_{HFOV})$ for Ω_S

5. Strictly speaking, the impulse response should have dimensions of s^{-1}. Thus, divide Equation 2.21 by Q_p

The resulting function is given by:

$$dh(t) = \frac{A_R k_s p(\theta_s = \pi)\exp(-k_e ct)}{4\pi^2(1 - \cos\theta_{HFOV})ct^2}\sin\theta\cos\theta\, d\phi\, d\theta \quad \text{seconds}^{-1} \tag{2.22}$$

The impulse response is calculated by integrating Equation 2.22 over the receiver's field of view. From Figures 2-1 and 2-6, this involves integrating $dh(t)$ from $\phi = 0$ to $\phi = 2\pi$ and $\theta = 0$ to $\theta = \theta_S$. Performing the integration yields:

$$h(t) = \frac{A_R k_s p(\theta_s = \pi)(1 - \cos 2\theta_{HFOV})\exp(-k_e ct)}{8\pi(1 - \cos\theta_{HFOV})ct^2} \quad \text{Watts} \tag{2.23}$$

Finally, the power received at the detector, $P(t)$, due to a transmitted pulse of the type shown in Figure 2-2 is the convolution of h(t) with a square pulse:

$$P_R(t) = \frac{A_R k_s p(\theta_s = \pi)}{8\pi c}\frac{1 - \cos 2\theta_{HFOV}}{1 - \cos\theta_{HFOV}}\int_{t-T_p}^{t}\frac{\exp(-k_e c\tau)}{\tau^2}d\tau \quad \text{Watts} \tag{2.24}$$

2.6 Conclusion

The purpose of this chapter has been the derivation of a middle ultraviolet atmospheric propagation model for use in the estimation of N_{O_3} and k_{sa} . First, the characteristics of the receiver and transmitter relevant to the propagation model were presented. Subsequently, the composition and interaction processes of the atmosphere were discussed. It was assumed that this medium is composed of molecular and aerosol particles which conservatively scatter and absorb radiation. Finally, given the models for the source, detector, and atmosphere, the pulse response of the atmosphere was derived by first calculating the impulse response of the medium and then convolving this function with a rectangular pulse of amplitude Q_p Watts and duration T_p seconds.

Chapter 3

A Maximum Likelihood Estimator for N_{O_3} and k_{sa} : Theory

3.1 Introduction

The problem of estimating atmospheric transmission parameters has been widely explored in a variety of contexts [25, 24, 29, 49, 38, 1, 60, 14, 57]. Much of this analysis is centered around inversion techniques associated with the laser radar (lidar) equation [25, 26, 39, 65, 64]. This equation describes the backscattered power incident upon a detector when a laser source is used to generate the transmitted pulses. As in Equation 2.24, the lidar equation gives backscattered power, P_{bs} as a function of the atmospheric parameters of interest, $\mathbf{x}$:

$$P_{bs} = f(\mathbf{x}) \tag{3.1}$$

The goal of these inversion procedures is to find an approximate form of f^{-1} so that the value of the parameters may be deduced from backscatter observations. While these techniques have enjoyed a great deal of success, the object of the present investigation

is to pursue the atmospheric parameter estimation problem from a standpoint which exploits the stochastic relationship between the backscattered power incident upon the detector and the observed detector output.

The object of this chapter is to develop a Maximum Likelihood (ML) estimator for determining the ozone number density and aerosol scattering coefficient based upon the collection of backscattered radiation in a direct detection system. In a such a system, photons impinging upon the detector due to a known radiation field result in short pulses of energy as output from the detector. It can be deduced from quantum mechanical principles that a probabilistic relationship exists between the incident field and the number of pulses observed at the output of the detector [32, 31, 30, 48]. The stochastic nature of this relationship allows for techniques such as Bayes Least Squares, Linear Least Squares, Maximum Likelihood and Maximum *A Posteriori* estimation procedures to be employed as a means of determining the unknown model parameters.

The formulation of the ML estimator first requires the specification of the stochastic process linking the backscattered radiation field to the detector output. The results of this effort is a probabilistic model encompassing all the parameters of interest from which any estimator can be formed. Given this probabilistic model, the ML estimator and the associated Cramer-Rao bound on the mean square estimation error are formally derived. Before pursuing this task, a review of probability and estimation theory relevant to this thesis is in order.

3.2 Elementary Probability Theory

Probability is that branch of mathematics concerned with the quantification of uncertainty. For physical systems which are either too complex to model in a deterministic manner or which are inherently non-deterministic, probability theory is used

to determine the likelihood that the system will be found in a particular state. For the purposes of this document, it is assumed that the reader is familiar with basic probabilistic concepts such as random variables, distribution functions, conditional probability, moments of random variables etc. The purpose of this section is twofold. First a description of the probabilistic notation to be employed in this document is presented. Second, the basic characteristics of the Poisson process are discussed.

3.2.1 Notational Conventions

The probability density function (PDF) for a continuous random vector $\underline{x}$is defined by

$$p_{\underline{x}}(\underline{X})d\underline{x} = Pr[X_1 < x_1 < X_1 + dX_1, X_2 < x_2 < X_2 + dX_2, \ldots, X_n < x_n < X_n + dX_n] \tag{3.2}$$

The subscript $\underline{x}$ in $p_{\underline{x}}(\underline{X})$ represents the random variable and the dummy variable, $\underline{X}$, is the value which $\underline{x}$ assumes. The notation $Pr[X_1 < x_1 < X_1 + dX_1]$ is the probability that the i^{th} component of $\mathbf{x}$ assumes a value between X_i and $X_i + dX_i$. Similarly a discrete PDF is denoted by:

$$Pr[\underline{y} = \underline{Y}] = Pr[y_1 = Y_1, y_2 = Y_2, \ldots, y_n = Y_n] \tag{3.3}$$

where $Pr[y_i = Y_i]$ is the probability that the i^{th} component of the random vector $\mathbf{y}$ assumes a value Y_i.

The expected value of a function of a random variable $\underline{z} = f(\underline{x})$ is calculated according to:

$$E[\underline{z}] = E[f(\underline{x})] = \int_{-\infty}^{\infty} f(\underline{x}) p_{\underline{x}}(\underline{X}) d\underline{x} \tag{3.4}$$

with an analogous formula for discrete type random variables. Letting $f(\underline{x}) = \underline{x}$ gives rise to the mean of a random variable which is denoted as $E[\underline{x}]$ or $\overline{\underline{x}}$. Alternatively,

$E[f(\underline{x})]$ for $f(\underline{x}) = (\underline{x} - E[\underline{x}])(\underline{x} - E[\underline{x}])^T$ yields the covariance matrix, Λ_x, of the random vector $\mathbf{x}$. (The superscript "T" denotes the transpose of a matrix or vector). The diagonal elements, $(\Lambda_x)_{i,i} = \sigma_x^2$ are the variances of the components of $\mathbf{x}$ and the off-diagonal elements, $(\Lambda_x)_{i,j} = \sigma_{ij}$, are the covariances between the i^{th} and j^{th} components of $\underline{x}$.

Finally, in the event that all components of a random vector, $\mathbf{x}$, are mutually independent, the joint PDF for $\mathbf{x}$ is the product of the marginal density functions for each x_i. Thus for a random vector of n elements,

$$p_{\underline{x}}(\underline{X}) = \prod_{i=1}^{n} p_{x_i}(X_i) \tag{3.5}$$

if all elements are mutually independent.

3.2.2 The Poisson Process

The Poisson process is a stochastic process used to describe the distribution of discrete points over some continuous domain of interest [50]. In this thesis the domain is temporal. The presence of a Poisson point at a particular time is called an arrival of the process. The full theory of Poisson processes allows for the description of many quantities associated with the arrivals including:

1. The probability that a given number of arrivals occur over some fixed time period,

2. The probability associated with the time from one arrival to the next arrival (also called the first order interarrival time) or from one arrival to the second, third or r^{th} next arrival (i.e. the r^{th} order interarrival time),

3. The joint probability density for the $N-1$ first order interarrival times given that N arrivals have occurred in some time period,

ad nauseum. The first item in the above list describes the interval characteristics of the process (i.e. the number of counts received in some time interval) while the last two elements of the above list provide information as to the location characteristics of the process (i.e. information concerning the timing of events) [50]. Of particular interest here are the interval characteristics of the Poisson process.

The count data of a Poisson process is described using a slightly different notation from that which was described in section 3.2.1. Specifically, the random variable representing the number of points observed in a given time interval is denoted using a capital N and the value of this RV is given y capital Y. The assignment of N to a Poisson RV and Y to the value of the same random variable will be used consistently throughout this document and will (hopefully) be the only break with the standard notation as presented above.

The PDF for the number of points observed from a Poisson process over some period of time, T_{obs}, is:

$$Pr[N = Y] = \frac{\Lambda^Y e^{-\Lambda}}{Y!} \qquad Y = 0, 1, 2 \ldots \tag{3.6}$$

In Equation 3.6, Λ is associated with the mean of the Poisson process and is called the Poisson rate parameter. This quantity may be written as

$$\Lambda = \int_{T_s}^{T_f} \lambda(\tau) d\tau \tag{3.7}$$

Where $T_{obs} = T_f - T_s$ represents the time interval over which the Poisson process is observed. The function $\lambda(t)$ is called the Poisson rate function and specifies the instantaneous average arrival rate of Poisson points.

A Poisson random variable has the interesting property that its mean equals its variance and both equal Λ. In the case that the rate function $\lambda(t)$ is the constant λ,

the process is termed *homogeneous*, and the mean and variance are

$$\overline{N} = \sigma_N^2 = \int_{T_s}^{T_f} \lambda d\tau = \lambda(T_f - T_s) = \lambda T_{obs} \tag{3.8}$$

A homogeneous Poisson process illustrates most clearly how λ may be interpreted as an average arrival rate. In the case where $\lambda(t)$ retains its dependence on time, the process is termed *inhomogeneous.*

Another useful feature of the Poisson process is that it possesses independent increments. This implies that PDF's for the number of arrivals in m non-overlapping time periods are independent. Thus,

$$Pr[N_{\Delta t_1} = Y_1, N_{\Delta t_2} = Y_2, \ldots, N_{\Delta t_m} = Y_m] = \prod_{i=1}^{m} Pr[N_i = Y_i] = \prod_{i=1}^{m} \frac{\Lambda_i^{Y_i} e^{-\Lambda_i}}{Y_i!} \tag{3.9}$$

The quantity $\Delta t_i = T_{f_i} - T_{s_i}$ is the i^{th} observation interval where all such intervals are mutually exclusive. In the above equation,

$$\Lambda_i = \int_{T_{s_i}}^{T_{f_i}} \lambda(\tau) d\tau \tag{3.10}$$

3.3 The Photodetection Process

Estimates of the ozone number density and the aerosol scattering coefficient will be based upon data gathered using a monostatic, direct detection measurement system (see figure 3-1). In such a system (also called a photodetection or photocounting system) there exists an electro-magnetic field incident upon a receiver which is composed of a photosensitive material, an amplifier and processing electronics [36]. In response to the photons comprising the incident radiation field, the receiver outputs voltage pulses. These pulses are referred to as photocounts and represent the measurable quantity which will be used to formulate the estimates of k_{sa} and N_{O_3} . In

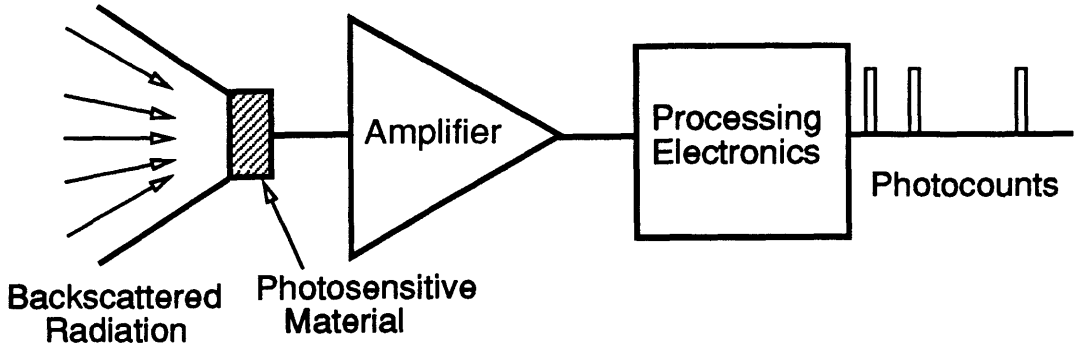

Figure 3-1: A Direct Detection Measurement System

this section, the stochastic relationship between the incident field and the photocounts is explored first assuming an ideal photodetection system and then supposing a simplified model for a real direct detection system.

3.3.1 An Ideal Photocounting System

In an ideal photodetection system there is no noise or other external processes associated with the receiver. As was discussed in the introduction to this chapter, there exists a non-deterministic relationship between the radiation field incident upon a photodetector and the photon counts which represent the output of the detector. Such a relationship seems reasonable given that the objects being observed in this case are photons, which according to the basic principles of quantum mechanics can only be described in a probabilistic manner. Clearly, because individual quanta of energy are counted, the random process will be discrete in nature, but determination of its exact form depends on a variety of exogenous factors. Given the following assumptions:

1. Atmospheric transmission can be described using an linear, time-invariant impulse response as derived in Chapter 2,

2. The source itself is deterministic (i.e. the amplitude and duration of each pulse are not random quantities) and

3. An ideal photodetection system,

it can be shown that a Poisson random process provides an excellent description of the photon counting problem [48]. The rate function $\lambda(t)$ associated with this process corresponds to the number of photons per unit time from the incident field impinging upon the receiver's photosensitive surface.

To obtain the expression for $\lambda(t)$, it is not necessary to have a full description of the electro-magnetic field. Rather, it is sufficient to start from the function, $P_R(t)$, describing the field's power which is incident upon the detector. Because

1. $P_R(t)$ gives the energy per unit time incident upon the detector

2. The energy in a single photon is:

$$E_p = \frac{hc}{\lambda} \tag{3.11}$$

where

E_p = The energy per photon [Joules/count]

h = Planck's constant ($6.63 * 10^{-34}$ [Joules seconds])

c = the speed of light ($3.0 * 10^8$ [meters/second])

λ = The wavelength of the radiation.

the rate function for the photodetection Poisson process due to $P_R(t)$ is

$$\lambda(t) = \frac{\lambda}{hc} P_R(t) \tag{3.12}$$

The power function corresponding to radiation field of interest in this investigation was derived in Chapter 2. This function of time, $P_R(t)$, determines the quantity of directly backscattered energy per unit time incident on the detector in response to an energy pulse transmitted from the same location a short time earlier under the single scatter approximation. Thus, given equations 2.24 and 3.12, the Poisson rate function for an ideal monostatic direct detection system is:

$$\lambda_I(t) = \frac{A_d \lambda}{8\pi hc^2} \frac{1-\cos(2\theta_{HFOV})}{1-cos(\theta_{HFOV})} (\beta_m k_{sm} + \beta_a k_{sa}) \int_{t-T_P}^{t} \frac{\exp(-(k_{sa}+k_{sm}+N_{O3}ka_{O3})c\tau)}{\tau^2} d\tau \tag{3.13}$$

Where the subscript I indicates that this is the rate function corresponding to the ideal photon arrival Poisson process.

3.3.2 Non-Ideal Photodetection

In actual direct detection system, there exists noise and other external processes associated with the receiver which may destroy the Poisson nature of the photocounting process. A common assumption is that there is a constant quantity known as the detection efficiency, ξ, which represents the ratio of the number of photocounts observed in the actual system to the number of counts which would be observed in an ideal detection system. The non-ideal photocounting process may now be redefined using Figure 3-2. In this figure, a radiation field is incident upon an ideal photodetector. The output of this system is a Poisson process $N_I(t)$ which serves as the input to a system $H(N_I, \xi)$. The output of H is the number of photocounts observed in the actual direct detection system. The cascade of the ideal receiver and the system H represents the non-ideal photodetector.

H operates on its input in the following manner. When an arrival from the process $N_i(t)$ is input to H a decision is made. With probability ξ the input pulse will be passed through H and appear as an observed photocount. With probability $1-\xi$

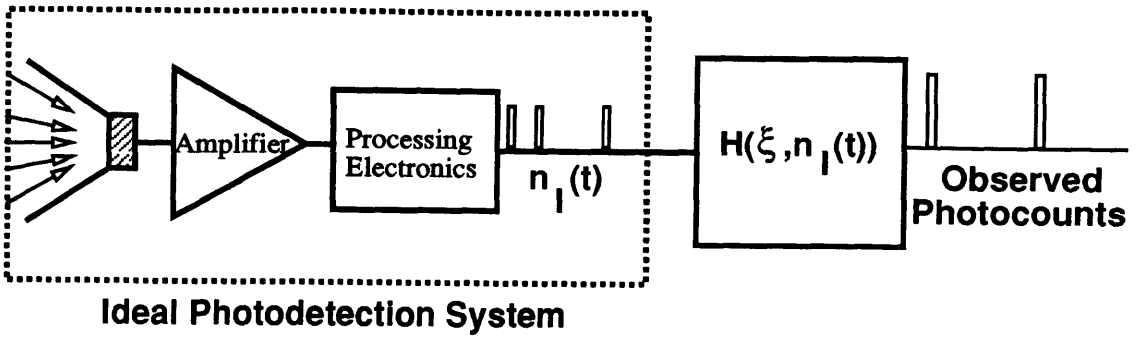

Figure 3-2: A Non-Ideal Direct Detection Measurement System

the count from $N_i(t)$ will result in no output from H (i.e. no observed count will be registered).

Given this probabilistic interpretation of ξ, the non-ideal pulse counting process may be thought of as a Poisson process with random erasures. That is, for each arrival of the underlying Poisson process (i.e. each photocount from the ideal system), there is a probability ξ that an actual photocount will be observed and a probability $1 - \xi$ that that the underlying arrival will not appear in the observed process. It can be shown [8] that this type of random process is still Poisson whose rate function, $\lambda(t)$, is

$$\lambda(t) = \xi\lambda_I(t) \tag{3.14}$$

where λ_I is the rate parameter of the ideal photodetection process. This conclusion makes intuitive sense. If, for example, $\xi = 0.5$ then on average, one would expect to see about half as many counts in the process suffering from erasures as would be observed in the underlying Poisson process. This is exactly what equation 3.14 indicates is the case.

From equations 3.13 and 3.14, the final form of the Poisson rate function to be

used in the estimation of N_{O_3} and k_{sa} is

$$\lambda(t) = \frac{A_d \lambda \xi}{8\pi hc^2} \frac{1-\cos(2\theta_{HFOV})}{1-cos(\theta_{HFOV})} (\beta_m k_{sm} + \beta_a k_{sa}) \int_{t-T_P}^{t} \frac{\exp(-(k_{sa}+k_{sm}+N_{O3}A_{O3})c\tau)}{\tau^2} d\tau \tag{3.15}$$

For the sake convenience in dealing with equation 3.15 the following notation is adopted:

$$\alpha = \frac{A_d \lambda \xi}{8\pi hc^2} \frac{1-\cos(2\theta_{HFOV})}{1-\cos(\theta_{HFOV})} \tag{3.16}$$

$$k_s = k_{sa} + k_{sm} \tag{3.17}$$

$$k_e = k_{sa} + k_{sm} + N_{O3}A_{O3} \tag{3.18}$$

$$\gamma_m = \beta_m k_{sm} \tag{3.19}$$

$$\gamma_a = \beta_a k_{sa} \tag{3.20}$$

$$\gamma = \gamma_m + \gamma_a \tag{3.21}$$

Incorporating this parameterization into the expression for $\lambda(t)$ yields:

$$\lambda(t) = \alpha\gamma \int_{\tau=t-T_p}^{t} \frac{exp(-k_e c\tau)}{\tau^2} d\tau \tag{3.22}$$

With equation 3.15 the statistical model encompassing the parameters to be estimated is complete. The next task is to use this model as the basis for algorithms which will extract the values of the atmospheric transmission parameters from observed count data.

3.4 Statistical Estimation

The object of the modeling process is to obtain a mathematical formulation corresponding to a physical situation such that, given the inputs to the process, the model

is able to predict in some sense the outputs which will be observed. Regardless of whether the model is deterministic or statistical, it is often the case that there exist in the model parameters whose values are not known. These parameters may be non-deterministic in that their values change randomly over time and space, or it may be the case that the parameters have fixed values which are unknown *a priori* to the modeler. Given the theoretical model which predicts how the system should behave and observations of the actual process which demonstrate how the system really acts, estimation techniques are often used to determine those values of the parameters which do the "best job" of matching the observed data to the form of the model. It is the formalization of the notion of "best job" which distinguishes different estimation techniques.

In the case of the pulse counting system, the model is stochastic in nature. Given a set of inputs to the system, such as pulses of radiation, the model can only predict statistical quantities associated with the system's output such as mean, variance, kurtosis etc. For modeling situations such as these there exist a wide range of parameter estimation techniques. In all cases the following assumptions hold.

1. There exists a vector of unknown parameters $\underline{x} \in \mathcal{R}^n$
2. There is a data vector $\underline{y}$ which is generated from a random process described by a PDF $p_{\underline{y}|\underline{x}}(\underline{Y}|\underline{X})$
3. It is desired to obtain an estimate of $\underline{x}$ which is as $\hat{\underline{x}}(\underline{Y})$ based upon the observations $\underline{Y}$. Where it shall cause no confusion the explicit dependence of the estimate upon $\underline{Y}$ will be dropped.

Given these basic commonalities, the various estimation schemes are differentiated according to assumptions made about the nature of the parameter vector $\mathbf{x}$ and the criterion used for choosing $\hat{\mathbf{x}}$ based upon $\mathbf{y}$. Some common options are:

1. **Bayesian estimation** [62] assumes that $\underline{x}$ is non-deterministic and can be described by a PDF $p_{\underline{x}}(\underline{X})$. The estimate $\hat{\underline{x}}$ is chosen to minimize the expected value of the cost function

$$C(\underline{x}, \hat{\underline{x}}) = \|\underline{x} - \hat{\underline{x}}\|^2 \tag{3.23}$$

conditioned on knowing $\underline{y} = \underline{Y}$. This basis for selecting an estimate is called the minimum mean square error criterion. In the Bayesian case, $\hat{\underline{x}}_B(\underline{Y}) = E[\underline{x}|\underline{Y}]$ where $E[A|B]$ is the conditional expectation of A given B. The Bayesian estimate tends to be difficult to find because it requires the explicit determination of $p_{\underline{x}|\underline{y}}(\underline{X}|\underline{Y})$. Furthermore, Bayesian analysis requires specification of $p_{\underline{x}}(\underline{X})$ which may not be available.

2. **Linear Least Squares Estimation** (LLSE) [62] also assumes that $\underline{x}$ has a PDF $p_{\underline{x}}(\underline{X})$ and chooses $\hat{\underline{x}}$ based on the same least squares criterion subject to the constraint that $\hat{\underline{x}}$ is of the form

$$\hat{\underline{x}}_L(\underline{Y}) = \mathbf{A}\underline{Y} + \mathbf{b} \tag{3.24}$$

where the matrix $\mathbf{A}$ and the vector $\mathbf{b}$ are chosen based upon the mean square error requirement. It can be shown that this estimate requires knowledge only of the second order statistics (means, variances, and covariances) associated with $\underline{x}$ and $\underline{y}$ rather than their complete joint distribution as would be required in the Bayesian case. Furthermore, the LLSE is linear by construction and therefore easier to formulate and work with than the Bayesian estimate. By constraining the form of $\hat{\underline{x}}$ to be linear it can be shown that the error variance of the LLSE can be no smaller than that of the Bayesian estimate. Thus the reduced complexity of the LLSE comes at a price of possibly reduced performance.

3. A **Maximum a Posteriori** (MAP) [62] estimator still assumes that $\underline{x}$ is probabilistic. The choice of $\hat{\underline{x}}_{MAP}$ is made according to the following rule:

$$\hat{\underline{x}}_{MAP}(\underline{Y}) = \arg\max_{\underline{x}} p_{\underline{x}|\underline{y}}(\underline{X}|\underline{Y}) \tag{3.25}$$

It can be shown that this manner of choosing an estimate may be derived by choosing $\hat{\underline{x}}_{MAP}$ to minimize the cost function

$$C(\underline{x}, \hat{\underline{x}}) = \begin{cases} K > 0 & \text{if } \hat{\underline{x}} \neq \underline{x} \\ 0 & \text{if } \hat{\underline{x}} = \underline{x} \end{cases} \tag{3.26}$$

This estimation technique involves finding maxima of the conditional distribution of $\underline{y}$ given $\underline{x}$. Assuming that $p_{\underline{y}|\underline{x}}(\underline{Y}|\underline{X})$ is differentiable in the parameter vector $\underline{X}$ and using Bayes' rule for calculating conditional PDF's, the necessary conditions for $\hat{\underline{x}}_{MAP}$ is reduced to finding that $\underline{X}$ which satisfies the following set of equations:

$$\frac{\partial}{\partial \underline{X}}(\ln p_{\underline{y}|\underline{x}}(\underline{Y}|\underline{X}) + \ln p_{\underline{x}}(\underline{X})) = 0 \tag{3.27}$$

which are called the MAP equations. The use of the log of the PDF is valid in the maximization procedure due to the fact that the natural logarithm function is non-decreasing over the set of non-negative real numbers. A solution to Equation 3.27 is a local maxima of $p_{\underline{y}|\underline{x}}(\underline{Y}|\underline{X})$ if it also satisfies the second order necessary condition:

$$\frac{\partial^2}{\partial \underline{X}^2} p_{\underline{x}|\underline{y}}(\underline{X}|\underline{Y}) < 0 \tag{3.28}$$

In the event of multiple maxima, the MAP estimate is taken as the largest of the maxima.

4. The final statistical estimation scheme to be covered here is the **Maximum Likelihood** (ML) [62] estimator. ML estimation is useful when the parameter

vector, $\underline{x}$, is a set of constants whose values are deterministic but unknown to the modeler. Like the other estimation schemes, the ML method starts with a set of observations, $\underline{Y}$, and a PDF, $p_{\underline{y}|\underline{x}}(\underline{Y}|\underline{X})$ describing the probability that the observation vector $\underline{y}$ assumes some value $\underline{Y}$ when the parameter vector $\underline{x}$ has the value $\underline{X}$. The ML estimate $\hat{\underline{x}}_{ML}$ is that value of $\underline{x}$ which makes the given observation vector $\underline{Y}$, most likely, i.e. that value of $\underline{x}$ which maximizes the probability of actually observing $\underline{Y}$. Mathematically, the ML estimator may be expressed as:

$$\hat{\underline{x}}_{ML} = \arg\max_{\underline{X}} p_{\underline{y}|\underline{x}}(\underline{Y}|\underline{X}) \tag{3.29}$$

or equivalently

$$\begin{aligned} \hat{\mathbf{x}}_{ML} &= \arg\max_{\underline{X}} \ln p_{\underline{y}|\underline{x}}(\underline{Y}|\underline{X}) \\ &= \arg\max_{\underline{X}} \ell(\underline{X}) \end{aligned} \tag{3.30}$$

where $\ell(\underline{X}) = \ln p_{\underline{y}|\underline{x}}(\underline{Y}|\underline{X})$ is called the log-likelihood function.

The ML estimate can be derived from the MAP estimate by assuming that the PDF for $\mathbf{X}$ is constant across its domain. Thus the derivative of $p_{\underline{x}}(\underline{X})$ with respect to $\underline{X}$ is zero and Equation 3.27 reduces to the ML equation:

$$\frac{\partial}{\partial \underline{X}} \ln p_{\underline{y}|\underline{x}}(\underline{Y}|\underline{X}) = 0 \tag{3.31}$$

for the vector $\underline{x}$. As in the case of the MAP estimate, a solution, $\hat{\underline{x}}$, of equation 3.31 will be the ML estimate if it also satisfies

$$\frac{\partial^2}{\partial \underline{X}^2} p_{\underline{y}|\underline{x}}(\underline{Y}|\underline{X} = \hat{\underline{X}}) < 0 \tag{3.32}$$

In the event that the log likelihood function has multiple maxima, the ML

estimate is taken as the largest of these extrema.

There are three criteria generally used as indicators of an estimator's performance. They are the bias, the error covariance, and the mean square error. The bias of an estimator is defined as:

$$\begin{aligned} b(\underline{X}) &= E[\underline{X} - \underline{\hat{x}}(\underline{y})|\underline{x} = \underline{X}] \\ &= E[\underline{e}|\underline{x} = \underline{X}] \end{aligned} \tag{3.33}$$

where $\underline{e}$ is called the error vector and is defined as the difference between the estimated value and the actual value of the parameter vector.

The error covariance matrix is:

$$\Lambda_e(\underline{X}) = E\{[\underline{e} - b(\underline{X})][\underline{e} - b(\underline{X})]^T\} \tag{3.34}$$

The $(i,i)^{th}$ diagonal element of this matrix is the error variance of the i^{th} parameter in $\underline{x}$ while the $(i,j)^{th}$ off diagonal entry of Λ_e is the error covariance between the i^{th} and j^{th} components of the parameter vector.

Finally the mean square error is given according to:

$$E[\underline{e}\underline{e}^T] = \Lambda_e(\underline{x}) + b(\underline{X})b(\underline{X})^T \tag{3.35}$$

Given that the estimator produces guesses with some bias, the error variance is a measure of how far from that bias point estimates may be expected to fall. If the variance is small then it would be unlikely for the estimates to be far from the bias point. On the other hand, a large variance would indicate that the estimates may be expected to be spread widely over the domain of interest (i.e not concentrated about the bias point). Assuming that the bias is small, then equation 3.35 demonstrates that a small variance would indicate that one may expect small errors in the estimates and

good performance from the estimator. Alternatively, a large variance would suggest that large errors and therefore poor performance may be expected.

Given that an unbiased estimator exists for a particular problem, the Cramer-Rao bound (CR bound) provides a lower bound on the mean square error matrix. This bound is calculated according to [62]:

$$\Lambda_e \geq I_{\underline{Y}}^{-1}(\underline{X}) \tag{3.36}$$

where $I_{\underline{Y}}(\underline{X})$ is called the Fisher information matrix and is given by:

$$\begin{aligned} I_{\underline{y}}(\underline{X}) &= E\{[\tfrac{\partial}{\partial \underline{X}} p_{\underline{y}|\underline{x}}(\underline{Y}|\underline{X})]^2 | \underline{x} = \underline{X}\} \\ &= -E\{\tfrac{\partial^2}{\partial \underline{X}^2} p_{\underline{y}|\underline{x}}(\underline{Y}|\underline{X}) | \underline{x} = \underline{X}\} \end{aligned} \tag{3.37}$$

Any unbiased estimator for which equation 3.36 is satisfied with equality is termed efficient. Furthermore, it can be shown that if an efficient estimator exists then it must be the ML estimator. Equations analogous to 3.36 and 3.37 can be formulated for the case of a biased estimator [50]. Such equations require the knowledge of both $b(\underline{X})$ and $\frac{\partial}{\partial \underline{X}} b(\underline{X})$ which in many cases cannot be obtained in closed form. For the problem of estimating the atmospheric transmission parameters, it will be shown from Monte-Carlo simulations that

1. The estimator is biased; however the bias is relatively small over the full range of both the ozone number density and aerosol scattering coefficient.

2. The unbiased form of the CR bound provides substantial information regarding the actual performance of the biased estimator

Given this situation, the CR bound for a biased estimator is neither presented nor discussed here.

3.5 The ML Estimator for k_{sa} and N_{O_3}

Because it is assumed that the ozone number density and aerosol scattering coefficient are non-random parameters in the atmospheric transmission model, the Bayesian, LLSE and MAP estimator are not applicable to the problem being addressed in this thesis. Thus of the four techniques for estimating a vector of unknown parameters given a stochastic model, the Maximum Likelihood scheme is most appropriate for the problem to be explored in this thesis.

This section will be devoted to the three facets of the Maximum Likelihood estimator:

1. The observation vector which provides the data used to formulate the estimates
2. The structure of the ML estimator
3. The Cramer-Rao bound on the variance of the estimator

3.5.1 The Observation Vector

The observation vector, $\underline{Y}$, contains the photocount data upon which estimates of k_{sa} and N_{O_3} are based. This vector is constructed to take advantage of two elements of the atmospheric model which allow for a wide range of information to be made available to the estimator: the spectral dependency of the ozone absorption process and the temporal characteristics of the backscattered power function.

The strong spectral characteristics of the ozone absorption process suggest that different information concerning the state of the atmosphere is available based upon the wavelength associated with the transmitted pulse. Pulses whose wavelength lie outside of the ozone absorption band do not suffer significant attenuation due to molecular absorption. Instead, they are impacted most heavily by aerosol scattering. Thus, detector counts collected from pulses whose wavelength is out of the ozone

absorption band should be most useful in determining k_{sa} . Alternatively, the effect of ozone absorption upon the number of observed detector counts is most prominent when the wavelength of the probing pulse is in the ozone absorption band. Even here, the counts are affected by the aerosol scattering process thereby creating a certain degree of ambiguity associated with separating the effects of ozone from those of the aerosol.

To alleviate this problem as well as take advantage of the information available at different frequencies, estimates of the atmospheric transmission parameters are based upon observed backscatter corresponding to multiple wavelengths. Specifically, it is assumed that the transmitter is capable of emitting incoherent, monochromatic pulses at two wavelength: an in-band wavelength, λ_{in} , and an out-of-band wavelength,λ_{out} . The observation vector is composed of backscattered detector counts arising from a single pulse at each of the two wavelengths. The choice of the wavelength pairs is a topic to be discussed in the following chapter.

In addition to the frequency of the probing pulse, the timing of the interval over which backscattered detector counts are collected may influence the information conveyed by the observed counts. From equations 3.7 and 3.14, the count rate parameter may be written

$$\Lambda = \alpha(\beta_a k_{sa} + \beta_m k_{sm}) \int_{t=T_s}^{T_f} \int_{\tau=t-T_p}^{t} \frac{\exp(-k_e c\tau)}{\tau^2} d\tau dt \tag{3.38}$$

From the above equations, it may be observed that the effects of molecular absorption on the magnitude of Λ are dependent upon the length of time the radiation has spent propagating through the atmosphere. Counts obtained during observation intervals directly after T_p will contain more information regarding the aerosol scattering process than the ozone absorption process because the radiation collected during these periods has not propagated sufficient distances through the atmosphere for sig-

nificant absorption to have occurred. Conversely, more information concerning the ozone number density will be available from count data collected during observation intervals long after the falling edge of the transmitted pulse. To obtain the information available from different intervals, the observation period for a single pulse is subdivided into n subintervals where the number of detector counts collected in each subinterval is placed in the observation vector.

An important issue with regard to the subinterval count collection scheme is the determination of how the overall observation interval is to be partitioned. One choice is to divide the interval $T_{obs} = T_f - T_s$ into equal subintervals of length T_{obs}/n. Such a scheme would lead to significant signal to noise problems. Specifically, because the rate function $\lambda(t)$ falls off faster than exponentially and it is desired to collect counts for times much greater than T_p, the later intervals in an equal length system would contain few counts. Such a situation would be tolerable except for the fact that unmodeled detector noise (shot noise, $1/f$ noise etc) would become an issue. Up to this point, it has been assumed that the number of counts obtained in any observation period would be high enough to allow detector noise to be ignored. To maintain this approximation, an alternative method to equal length subintervals is required.

Specifically, the length of subintervals is chosen so that the expected number of counts obtained in all subintervals is the same. Given some initial guess as to the values of N_{O_3} and k_{sa} and the starting and ending times, T_s and T_f of the overall observation period, the expected number of counts for the period T_{obs} is given by equation 3.38. Thus, the n subintervals are to be chosen such that the expected number of counts in each is Λ/n.

The beginning and ending times of the i^{th} observation interval (t_{s_i} and t_{f_i} respec-

tively) are calculated in an iterative manner. Assuming that

$$\begin{aligned} t_{s1} &= T_s \\ t_{s_i} &= t_{f_{i-1}} \end{aligned}$$

the ending time for the i^{th} interval is found by determining that value of t_{f_i} which satisfies:

$$\int_{t_{s_i}}^{t_{f_i}} \lambda(t)dt = \Lambda/n \tag{3.39}$$

where the solution is found numerically using Brent's method [40] for determining roots of equations. As new estimates of the parameters are generated, the expected number of counts in the overall observation interval will change. Thus it may be necessary to recalculate the beginning and ending times of the n observation subintervals.

In summary, the observation vector for the problem of determining k_{sa} and N_{O_3} contains $2n$ elements. The first n are the observed counts for the n subintervals associated with the pulse of wavelength λ_{in}. Similarly, the last half of the vector contain the backscattered counts observed from a probing pulse of wavelength λ_{out}.

3.5.2 A Poisson ML Estimator

To formulate the Maximum Likelihood Estimator for the problem of determining atmospheric parameters from backscattered energy, it is necessary to apply the techniques of section 3.4 to the model developed in section 3.2.2.

Given $2n$ observations, Y_i, of a Poisson process from mutually exclusive time intervals, the log-likelihood function may be written as

$$\ell(\mathbf{Y}) = \sum_{i=1}^{2n} (Y_i \ln \Lambda_i(\mathbf{x}) - \Lambda_i(\mathbf{x}) - \ln Y_i!) \tag{3.40}$$

where this equation may be derived by taking the natural log of equation 3.9. Here, $\Lambda_i(\mathbf{x})$ is the mean of the i^{th} observation interval and is a function of the parameters to be estimated. Where it will cause no confusion, the explicit dependency of Λ_i on $\mathbf{x}$ will be dropped. The ML estimate, $\hat{\mathbf{x}}_{ML}$, is calculated by maximizing $\ell(\underline{X})$ over the range of $\underline{x}$. The necessary condition on $\hat{\mathbf{x}}$ are given by equation 3.27. For the case of a Poisson ML estimator these equations specialize to [50]:

$$\frac{\partial}{\partial \underline{x}}\ell(\underline{Y}) = \sum_{i=1}^{n}\left(\frac{Y_i}{\Lambda_i} - 1\right)\frac{\partial}{\partial \underline{X}}\Lambda_i = 0 \tag{3.41}$$

where $\frac{\partial}{\partial \underline{X}}\Lambda_i$ is a column vector whose j^{th} element is $\frac{\partial}{\partial X_j}\Lambda_i$. In the case of estimating the two atmospheric parameters k_{sa} and N_{O_3} , this column vector contains the two components:

$$\frac{\partial}{\partial N_{O3}}\Lambda_i = -cA_{O3}\alpha\gamma\int_{t=T_{s_i}}^{T_{f_i}}\int_{\tau=t-T_p}^{t}\frac{exp(-k_e c\tau)}{\tau}d\tau dt \tag{3.42}$$

$$\frac{\partial}{\partial k_{sa}}\Lambda_i = -\left(\alpha\beta_a\int_{t=T_{s_i}}^{T_{f_i}}\int_{\tau=t-T_p}^{t}\frac{exp(-k_e c\tau)}{\tau^2}d\tau dt + \alpha\gamma\int_{t=T_{s_i}}^{T_{f_i}}\int_{\tau=t-T_p}^{t}\frac{exp(-k_e c\tau)}{\tau}d\tau dt\right) \tag{3.43}$$

Substitution of equations 3.42 and 3.43 into 3.41 would yield the set of equations which would need to be solved in terms of k_{sa} and N_{O_3} in order to obtain the ML estimates of these parameters. Because no closed form solutions for k_{sa} and N_{O_3} may be obtained easily, the original problem

$$\underline{\hat{x}}_{ML}(\underline{Y}) = \max_{\underline{x}} \ln p_{\underline{y}|\underline{x}}(\underline{Y}|\underline{X}) \tag{3.44}$$

will be solved using a numerical optimization routine. Specifically, the necessary equations have been implemented on a VAX 6800 and the optimization problem has been solved using a quasi-Newton optimization algorithm from the IMSL Fortran

math library.

In addition to the estimate itself, it is not possible to obtain closed expression for the bias and error covariance matrix associated with the estimator. Instead, as will be detailed in the following chapter, Monte-Carlo simulations have been used to obtain approximations of the mean square error and average bias of the estimator as the parameters vary over their full ranges.

While the statistics for the ML estimator cannot be obtained directly, the Cramer-Rao bound may be calculated easily. From equation 3.36 the Cramer-Rao bound is:

$$\Lambda_e(\underline{X}) \geq I_{\underline{Y}}^{-1}(\underline{X}) \tag{3.45}$$

where $\Lambda_e(\underline{X})$ is the error covariance matrix of an unbiased estimator and $I_{\underline{Y}}(\underline{X})$ is the Fisher information matrix which may be calculated according to equation 3.37. While it is impossible to determine *a priori* whether the estimator for k_{sa} and N_{O_3} will be biased, calculation of the CR bound will still give a "best case" indication as to the performance of the estimator. A poor bound may indicate that a different measurement procedure is required to solve the problem. That is, it may be necessary to collect information regarding the transmission parameters in a different manner from the one considered here in order to obtain accurate estimates. Favorable results from the CR bound would suggest that the ML estimator may be sufficient to handle the problem and further investigation is warranted.

For a Poisson ML estimator, the Fisher matrix is [50]:

$$I_{\underline{Y}}(\underline{X}) = \sum_{i=1}^{m} \left\{ (\Lambda_i)^{-1} \left[\int_{T_{s_i}}^{T_{f_i}} \frac{\partial}{\partial \underline{X}} \lambda(\underline{x}, t) dt \right] \left[\int_{T_{s_i}}^{T_{f_i}} \frac{\partial}{\partial \underline{X}} \lambda(\underline{x}, t) dt \right]^T \right\} \tag{3.46}$$

where the index i refers to counts from the i^{th} observation interval. Interchanging the order of integration and differentiation in the summation, allows the Fisher informa-

tion matrix to be rewritten as

$$I_{\underline{Y}}(\underline{X}) = \sum_{i=1}^{m} \left\{ (\Lambda_i)^{-1} \left[\frac{\partial}{\partial \underline{X}} \Lambda_i(\underline{x}) \right] \left[\frac{\partial}{\partial \underline{X}} \Lambda_i(\underline{x}) \right]^T \right\} \tag{3.47}$$

For the specific problem at hand, where the parameter vector is $\underline{x} = [N_{O3} \;\; k_{sa}]^T$, the Fisher information matrix is:

$$I_{\mathbf{Y}}(\mathbf{X}) = \sum_{i=1}^{m} (\Lambda_i)^{-1} \begin{bmatrix} \left(\frac{\partial}{\partial N_{O3}} \Lambda_i\right)^2 & \left(\frac{\partial}{\partial N_{O3}} \Lambda_i\right)\left(\frac{\partial}{\partial k_{sa}} \Lambda_i\right) \\ \left(\frac{\partial}{\partial N_{O3}} \Lambda_i\right)\left(\frac{\partial}{\partial k_{sa}} \Lambda_i\right) & \left(\frac{\partial}{\partial k_{sa}} \Lambda_i\right)^2 \end{bmatrix} \tag{3.48}$$

where the partial derivatives are given in equations 3.42 and 3.43.

3.6 Conclusion

The goal of this chapter has been the development of a Maximum Likelihood Estimator to be employed in the determination of the two transmission parameters of interest. After a brief review of probability theory, a statistical model was developed to describe the photodetection process. This model provides the link between the transmitted pulse and the observations upon which the estimates are to be based. Subsequently it was shown that a Maximum Likelihood method is an appropriate estimation technique for the problem at hand. Finally, the analytical equations associated with the estimator and the Cramer-Rao lower bound were derived from the single scatter propagation model and photodetection model presented in Chapters 2 and 3.

Chapter 4

Performance Analysis of the Maximum Likelihood Estimator

4.1 Introduction

The mathematical structure of the Maximum Likelihood estimator developed in Chapter 3 says little about how this algorithm actually performs in estimating the ozone number density and aerosol scattering coefficient. The quality of the estimates obtained using the the ML scheme is dependent upon a variety of factors. On the one hand, the ability to determine N_{O_3} and k_{sa} is dependent upon the actual quantity of ozone and aerosol present in the atmosphere. Additionally, there are a variety of auxiliary parameters associated with the single scatter model which have an effect upon the accuracy of the estimates. In some cases, these parameters may be set to known quantities. In other cases, it is necessary to assume nominal values for parameters whose actual values are determined exogenously. While it is possible to build an ML estimator for this latter set of quantities, it may be the case that uncertainty in their exact values has little or no impact on the estimator or that the negative effects of this uncertainty may be offset through actions which are under the user's control.

In such cases, the added complexity of a larger dimension ML estimator would be unwarranted.

The goal of this chapter is to explore the performance of the estimator under a variety of configurations of the auxiliary parameter set. This evaluation is carried out in two steps. First, a base configuration is determined in a manner which is consistent with (1) the requirements of the atmospheric monitoring system of which the estimation algorithms are to be a part and (2) the constraints imposed on the values of these parameters by assumptions present in the single scatter model. Second, performance data for the base case and a variety of deviations from this standard are presented and analyzed. This performance information is obtained through calculations of the matrix Cramer Rao lower bound (CRLB) as well as through Monte Carlo runs in which simulated data is fed into the ML algorithm.

4.2 A Base Configuration of the Auxiliary Parameter Set

Evaluation of the ML estimator can only be carried out after numerical values have been chosen for the auxiliary parameters associated with the single scatter pulse response. From equation 3.15 this parameter set is composed of:

1. The transmitter half field of view angle: θ_t (rad)
2. The receiver half field of view angle: θ_r (rad)
3. The duration of the transmitted pulse: T_p (seconds)
4. The power of the transmitted pulse: Q_p (Watts)
5. The start time of observation: T_s (seconds)

6. The end time of observation: T_f (seconds)

7. The area of the receiver: A (m^2)

8. The number of subintervals into which the overall observation time is divided.

9. The wavelengths of the two probing pulses

   (a) The pulse whose wavelength is in the ozone absorption band, λ_{in} (m)

   (b) The pulse whose wavelength is out of the ozone absorption band, λ_{out} (m)

10. The detection efficiency: ξ (dimensionless)

11. The parameters of the Heney-Greenstein aerosol phase function: f and g (dimensionless)

Selection of numerical values for these quantities affects the information (the number of photocounts) upon which the estimates are based thereby impacting on the ability of the ML estimator to determine the values of N_{O_3} and k_{sa} . While the formulae presented in Chapters 2 and 3 describe the manner in which the the set of auxiliary parameters influences the backscatter, these mathematical constructions provide no information regarding realistic values these parameters may to assume.

Two standards are to be employed in the determination of the base set of parameter values. First, they must be chosen in a manner consistent with considerations associated with the type of atmospheric monitoring system in which the estimation algorithms are to be a used. Second, the auxiliary parameter values are to be determined so as to be compatible with the assumptions associated with the single scatter model of atmospheric propagation which lies at the heart of the ML estimator. The remainder of this section is devoted to the choice of a set of auxiliary parameter values which are consistent with these two criteria.

4.2.1 Systemic Restrictions

Systemic restrictions on the values of the auxiliary parameters arise from considerations associated with the form and functionality of the overall system to be used in the estimation of atmospheric transmission parameters. Specifically, the estimation algorithms are to be part of a system whose overall goal is the acquisition of local estimates of the ozone number density and aerosol scattering coefficient using a low energy, pulsed, narrow field of view monostatic receiver/transmitter system operating in the middle ultraviolet. Such a system is similar to light radar (lidar) systems except that the source of radiation is to be incoherent rather than laser. Thus, the parameter values used in typical lidar systems provide a reference point for the corresponding quantities to be defined here.

From the general description of the sensing system of interest, numerous constraints on the values of the auxiliary parameters are apparent:

1. The idea of locality must be quantified. For the purposes of this investigation, it is assumed that local estimates correspond to distances of up to 1 km from the transmitter/receiver. One kilometer has been chosen to satisfy assumptions concerning the homogeneity of the atmospheric constituents. In typical propagation models, the atmosphere is assumed to be a layered medium where the composition of the medium is constant in any given layer and the thickness of each layer is on the order of 1 km [11].

   Given this 1 km constraint, the maximum round trip path of any photon from the transmitter to the receiver is 2 km and the observation interval can last at most

$$T_{f,max} = \frac{2000 \text{ m}}{3.0 \times 10^8 \text{ m/s}} \approx 6700 \text{ ns}.$$

   This definition of locality may be compared to typical, ground based lidar systems which are used to measure atmospheric characteristics corresponding to

System	Q_p (MW)	T_p (ns)	E_p (mJ)
Quantel Model 482 [36]	23.3	15	350
Lambda Physik Model 202-MSC [36]	19.1	35	670
XeCl Excimer [37]	1.4	16	50

Table 4.1: Transmitted Pulse Parameters from Typical Lidar Systems

distances up to 40 km from the receiver/transmitter [36].

2. Low energy pulses are assumed to be less than 10 mJ. Because the pulses are rectangular, the energy in each pulse, E_p, is given by $E_p = Q_p T_p$. Typical figures for lidar systems are given in Table 4.1.

   Because the system to be employed in this investigation is concerned with measurements over a smaller distance from the transmitter/receiver, pulses of relatively small energy are used. Specifically, the initial configuration is:

$$\begin{aligned} T_p &= 100 \text{ ns} \\ Q_p &= 1 \times 10^4 \text{ W} \\ E_p &= 1.0 \text{ mJ} \end{aligned}$$

3. A narrow field of view system is assumed to have a maximum solid angle field of view of 100 mrad. From Equation 2.1 the relationship between solid angle field of view Ω and half field of view angle, θ, is $\Omega = 2\pi(1 - \cos\theta)$. Hence the maximum half field of view angles for the receiver and transmitter for this investigation are $\theta_{r,max} = \theta_{t,max} = \theta_{HFOV} \approx 10°$. For the sake of comparison, lidar systems have typical solid angle fields of view of less than 2 mrad [36]. It is believed that the larger field of views to be considered in this investigation may be used to collect more backscattered photocounts without violating the single scatter assumption which will be shown to depend upon field of view (see

section 4.2.2).

4. Operation of the system in the middle ultraviolet restricts the wavelengths of the probing pulses to be in the range 230 nm to 350 nm.

5. Overall detection efficiency for photocounting systems tends to be in the 1 to 10 percent range [10]. A value of $\xi = 0.01$ is assumed for this investigation.

6. The area of the receiver is taken to be 1 cm^2.

Additionally, constraints upon the values of the auxiliary parameter set arise due to limitations associated with the photon counting processes. For incident photon rates much above 10^{10} photons per second, counting systems will saturate [16] thereby losing their ability to accurately determine the number of photons observed over a given time interval. The monostatic, single scatter pulse response developed in Chapter 2 predicts photon arrival rates on this order of magnitude for times close to the falling edge of the transmitted pulse. To avoid problems with saturation, the start time of the observation interval will be delayed from the falling edge of the pulse. A delay of T_d seconds corresponds to collecting photons which have traveled a minimum distance of $cT_d/2$ meters from the transmitter where c is the speed of light. Typically, ground based lidar systems choose such delay distances to be on the order of 1 km which is about $1/40^{th}$ of the overall path length [36]. For this system, the maximum path length is 1 km. Thus a reasonable range delay is 25 m corresponding to a minimum time at which to begin observation of 80 ns after the falling edge of the pulse. The choice of $T_{d,min} = 80$ ns does not guarantee count rates sufficiently low so as to avoid saturation, but it has been chosen in a manner consistent with present lidar practice thereby providing a reasonable starting point for more rigorous analysis.

4.2.2 Modeling Constraints

A more subtle set of constraints on the configuration of the auxiliary parameter set arises from issues associated with the single scatter assumption of atmospheric transmission. The validity of the single scatter model is dependent upon the state of the atmosphere, the geometry of the receiver/transmitter system, and the observation time interval. Specifically, two quantities, the optical depth, τ, and the receiver field of view, Ω_r, have been used as benchmarks for gauging the validity of the single scatter model [45].

The optical depth is a dimensionless quantity defined as the product of the atmospheric extinction coefficient, k_e, and the distance, r, a photon travels from the transmitter to the receiver:

$$\tau = k_e r \tag{4.1}$$

where k_e is defined as

$$k_e = k_s + k_a \tag{4.2}$$

Van De Hulst [18] specified that in a conservative scattering medium, the single scatter approximation should hold for optical depths less than 0.1. For $0.1 < \tau < 0.3$, the single scatter model may be valid but would probably need to be supplemented by consideration of second and third order scattering effects. Finally for $\tau > 0.3$, a multiple scatter model would be required to accurately describe atmospheric radiative transfer. When the medium displays absorption processes in addition to scattering effects, the Van de Hulst bound may no longer be a valid limit for the single scatter approximation. For example, typical monostatic lidar systems which employ a single scatter approximation in their calculations may examine photocount returns from up to a 40 km range (or an 80 km round trip path length). Under the following assumptions:

1. The probing pulse is at 275 nm

2. The ozone number density is a constant 20 ppb

3. No aerosol is present

4. Molecular scattering is ignored

according to Equation 4.2 the extinction coefficient is

$$k_e = N_{O_3} k_{A,O_3,PURE} = (20 \times 10^{-9})(1.56 \times 10^7 \text{ km}^{-1}) = 0.312 \text{ km}^{-1} \tag{4.3}$$

for a total optical depth of $\tau = (80 \text{ km})(0.312 \text{ km}^{-1}) = 24.96$ which is clearly greater than 0.1. Nevertheless, the calculations and estimates made using the single scatter lidar equation produce accurate results [25, 36, 3, 35]. Thus, the validity of the single scatter model must be determined by more than optical depth considerations.

These additional considerations are related to the geometry of the transmitter and receiver system. Most lidar systems as well as the system under consideration here are of the monostatic, narrow field of view photon counting variety. Photons collected in a monostatic system have either:

1. Been scattered exactly once at a scattering angle of π radians (see Figure 4-1) or

2. Been scattered multiple times such that the final scattering event occurs in the receiver's field of view and in the appropriate direction (see Figure 4-2)

Consider Equation 2.8, the composite phase function when both aerosol and ozone are present in the atmosphere. Even for the case where the ozone number density is high (90 ppb) and the aerosol scattering coefficient is relatively low (0.1 km^{-1}), Figure 4-3 demonstrates that the phase function is strongly forward-peaked. Thus,

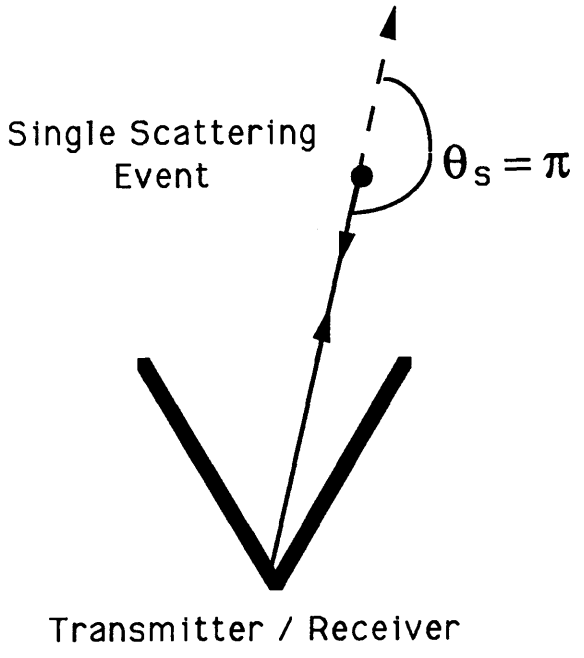

Figure 4-1: Single Scatter Photon Collection

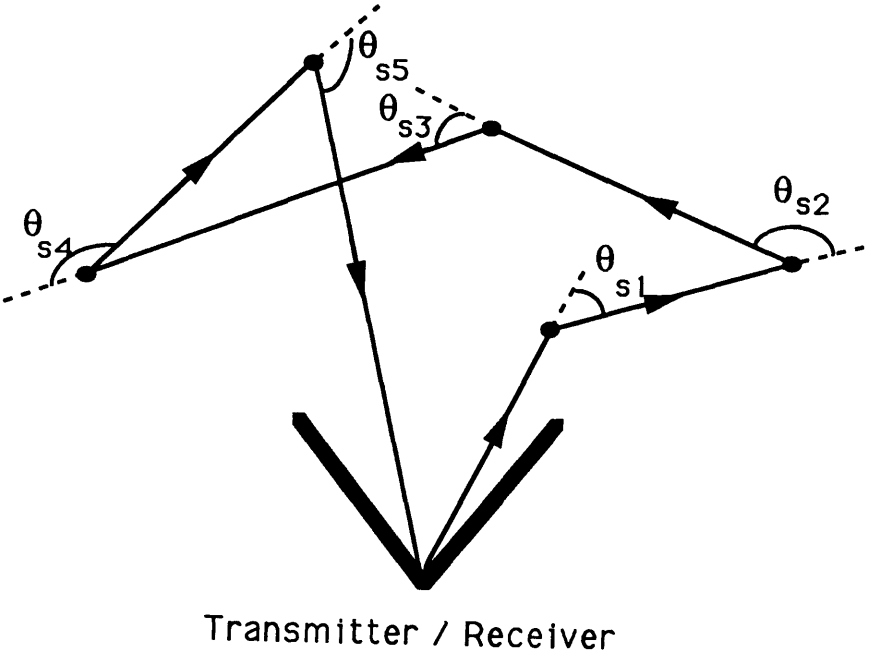

Figure 4-2: Multiple Scatter Photon Collection

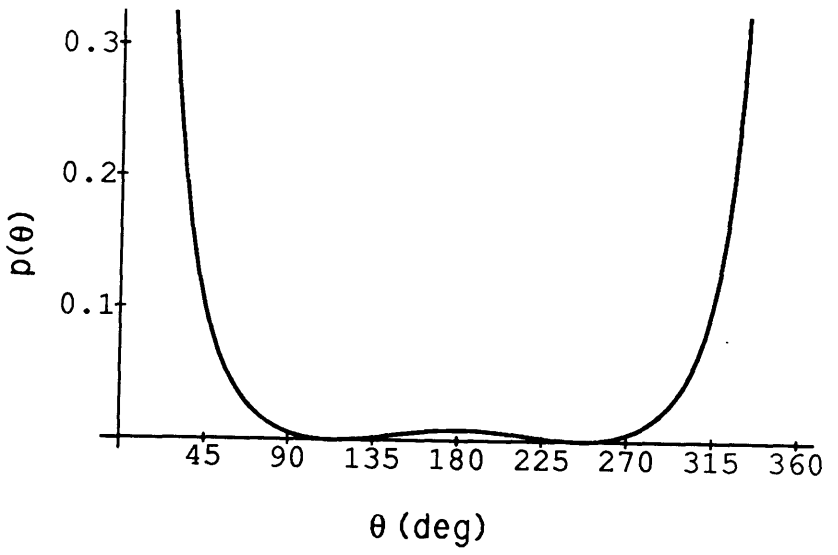

Figure 4-3: Single Scatter Phase Function: High Ozone and Low Aerosol

the vast majority of scattering events result in photons which are redirected into the forward hemisphere relative to their line of motion before the scattering event. Very few are scattered into the rear hemisphere and even fewer are directly backscattered. Furthermore, as the field of view of the system becomes narrower, it will be less probable that multiply scattered photons are detected by the receiver. Even as the extinction coefficient rises and the corresponding optical depth becomes greater than 0.1, it is reasonable to suppose that the forward nature of scattering process will minimize the effects of multiple scatter on a narrow FOV, monostatic photocounting system. Reducing the FOV to limit the number of collected photons does imply lowering the efficiency of the detection system; however it is expected that such action will not have too large an effect on the performance of the estimation algorithms.

The above argument is admittedly non-rigorous, but it is not the purpose of this investigation to examine the conditions under which a single scatter approximation to the radiative transport equation may be considered valid. Rather, the previous discussion, coupled with the nominal optical depth data associated with lidar practice

are to be taken a justification for using the single scatter model for returns corresponding to optical depths greater than 0.1. Specifically, it is assumed for the remainder of this investigation that single scatter approximation holds for monostatic system with a field of view less than 100 mrad and optical depths less than 5.0. Validation of this assumption could be carried out by either

1. Comparing the results of the single scatter model for the transmitter/receiver geometry of interest here to those obtained using a valid multiple scatter model (LOWTRAN or FASCODE) for the same geometry

2. Constructing of a narrow field of view, monostatic, middle-ultraviolet system and measuring actual backscattered photocounts

Unfortunately, neither of these techniques is available at the present time.

Additional modeling considerations arise from the use of the modified Heney-Greenstein phase function to describe the aerosol scattering processes. Specifically, this approximation to the Mie phase function is specified by two parameters, commonly referred to as g and f. Following Zachor [63] initial values for these quantities are:

$$\begin{aligned} g &= 0.72 \\ f &= 0.50 \end{aligned} \tag{4.4}$$

4.2.3 A Reasonable Initial Configuration

Based upon the considerations presented in Sections 4.2.1 and 4.2.2, the initial values assigned to the auxiliary parameter set are given in Table 4.2 where all parameters have been assigned values except T_f, λ_{in} , and λ_{out} .

$\theta_t = 10°$	$\theta_t = 10°$	$Q_p = 10,000$ W
$T_p = 100$ ns	$T_s = 180$ ns	$\xi = 0.01$
$g = 0.72$	$f = 0.5$	Area $= 1$ cm^2

Table 4.2: Initial Values for the Auxiliary Parameter Set

Choosing T_f

While it is certainly desirable to collect photocounts for as long as possible so as to maximize the data available to the estimator, long observation intervals correspond to higher optical depths and decreased validity of the single scatter model. In the interest of avoiding such difficulties, T_f is chosen such that the minimum required observation interval is used in order to obtain a given level of photocount return. Specifically, consider the Equation 3.38 as a function only of T_f. This equation gives the expected number of photocounts, Λ obtained over a given observation interval. Of interest here is the the form of the integral portion of this equation as a function of its upper limit:

$$I(b) = \int_{t=a}^{b} \int_{\tau=t-\gamma}^{t} \frac{e^{-\alpha\tau}}{\tau^2} d\tau \tag{4.5}$$

In Figure 4-4 the function $I(b)$ is plotted for $a = 2$, $\alpha = 1$, $\gamma = 0.5$. It appears that after some value of b, there is no significant increase in $I(b)$. Turning to the case where $I(b)$ represents the integral in Equation 3.38, one may interpret the asymptotic behavior of I as an indication that there exist some value of T_f, to be called $T_{f,100}$, such that the additional photocounts obtained by extending the observation interval beyond $T_{f,100}$ is negligible (the subscript 100 indicated 100% photocount return.) That is there is a maximum length of the observation period such that all the useful data which may be obtained from a given transmitted pulse has been obtained. The object of this section is to find the value of $T_{f,100}$ as a function of N_{O_3} and k_{sa} according to the following procedure.

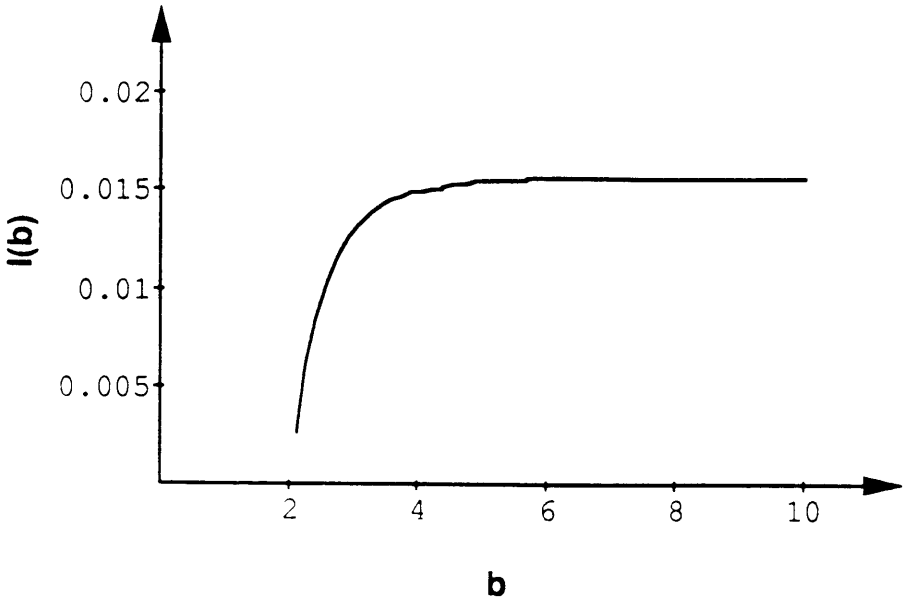

Figure 4-4: Exponential Integral as a Function of Upper Limit of Integration

1. First, it is impractical to find $T_{f,100}$ for all points in the (N_{O3}, k_{sa}) plane. Rather, this parameter space is divided into an evenly spaced, 10 by 10 grid for $N_{O3} \in [0, 100]$ ppb and $k_{sa} \in [0, 3]$ km^{-1}. The values of $T_{f,100}$ are found for the points corresponding to the vertices of the grid.

2. Given the values of N_{O_3} and k_{sa} , it is desired to determine that value of T_f such that $\Lambda(T_f)$ and $\Lambda(T_f + \delta t)$ differ by a to-be-specified negligibly small amount, where the function $\Lambda(T_f)$ is the expected number of photocounts observed over a specified time interval ending at time T_f and is given by Equation 3.38. In other words, we wish to find an end time of the observation interval such that the number of additional photocount seen by increasing T_f some small amount is negligible.

3. Before finding $T_{f,100}$ it is necessary to specify δt and the notion of negligible stated in the above paragraph. For this investigation, δt is taken as 100 ns. This provides a rather course increment but the object of this analysis only is to gain a rough idea of the time scale over which the pulse response yields useful

data. Further, the notion of small is taken to be 10^{-4} photocounts. Given that the total number of photocounts observed over the intervals of interest will be shown to be on the order of thousands, 10^{-4} seems small. Given these quantities, $T_{f,100}$ is that value of T_f for which the following holds:

$$\Lambda(T_f + \delta t) - \Lambda(T_f) < 10^{-4} \tag{4.6}$$

4. To find $T_{f,100}$ for a given point in (N_{O3}, k_{sa}) space the algorithm in Figure 4-5 is used.

5. To express its dependency on N_{O_3} and k_{sa} , the value of $T_{f,100}$ found using the above algorithm is denoted $T_{f,100}(N_{O3}, k_{sa})$. Also, the expected number of observed photocounts for $T_f = T_{f,100}(N_{O3}, k_{sa})$ is given as $N_{100}(N_{O3}, k_{sa})$. Finally, corresponding to each $T_{f,100}(N_{O3}, k_{sa})$ the optical depth, $\tau_{100}(N_{O3}, k_{sa})$ is calculated according to

$$\tau_{100}(N_{O3}, k_{sa}) = cT_{f,100}(N_{O3}, k_{sa})k_e(N_{O3}, k_{sa}) \tag{4.7}$$

where

- c = The speed of light (3.0×10^8 m/s)
- $k_e(N_{O3}, k_{sa})$ is the extinction coefficient calculated according to Equation 4.2

6. While, $T_{f,100}(N_{O3}, k_{sa})$ gives the longest reasonable time to wait in the collection of photocount data, it may be the case that such observation periods violate the single scatter assumption or perhaps the performance of the estimator will not suffer for intervals corresponding to $T_f < T_{f,100}(N_{O3}, k_{sa})$. To explore such possibilities in an organized manner, observation end times and corresponding

```
(* Initialize tf to some value slightly larger than ts *)
tf := ts+ 1

(* Iterate through successive values of tf until the
   condition on the function Λ is met at which point exit the loop *)
DO WHILE ( Λ(tf + 100) - Λ(tf) < 10 - 4)
        tf := tf + 100
END DO

(* The final value of Λ is assigned to the variable
   "fullcount" for later use. *)
fullcount := Λ(tf)

(* Return the two values of interest *)
RETURN(tf , fullcount)
```

Figure 4-5: Algorithm for Determining $T_{f,100}$

```
(* Initialize tf to some value slightly larger than ts *)
tf,95 := ts+ 1

(* Iterate through successive values of tf,95 until the
   value of Λ is 95% of fullcount *)
DO WHILE ( Λ(tf,95) < 0.95*fullcount)
        tf,95 := tf,95 + 1
END DO

(* Return tf,95*)
RETURN(tf,95)
```

Figure 4-6: Algorithm for Determining $T_{f,p}, p \in \{50, 95, 99\}$

optical depths are computed such that the expected number of received photocounts is 50%, 95%, and 99% of that obtained for an observation interval with $T_f = T_{f,100}$ (i.e $0.5N_{100}$,$0.95N_{100}$,and $0.99N_{100}$ respectively). For a given fraction of expected return, $p \in (50, 95, 99)$, and given point (N_{O3}, k_{sa}) the respective end time of observation and optical depth are given by $T_{f,p}(N_{O3}, k_{sa})$ and $\tau_p(N_{O3}, k_{sa})$ respectively. The algorithm for calculating $T_{f,p}(N_{O3}, k_{sa})$ is given in Figure 4-6.

The above procedure was carried out for $\lambda = 255$ nm and for $\lambda = 315$ nm. These two wavelengths were chosen to provide information as to the behavior of the single scatter pulse responses for wavelengths in and out of the ozone absorption band. The peak of this band occurs at 255 nm. By 315 nm, the ozone absorption cross section is less than 1% of its value at 255 nm.

The results of these calculation are displayed in Figures 4-7 and 4-8 and Tables 4.3, 4.4, and 4.5. The graphs are surface plots showing how $T_{f,99}$ and τ_{99} vary as a function of N_{O_3} and k_{sa} . Corresponding figures for the 50%, 95% and 100% cases display similar characteristics and are not presented here. Tables 4.3 and 4.4 give the minimum, mean, and maximum values of $T_{f,p}$ and τ_p for the cases of interest here. Table 4.5 summarizes the minimum, mean, and maximum number of expected photon counts observed for 100% returns at the two wavelengths of interest.

For the $\lambda = 315$ nm cases:

1. The end times and optical depths are relatively insensitive to the quantity of ozone in the atmosphere. Such a situation is to be expected given the weak absorption properties of O_3 at this frequency.

2. The observation period ending times is inversely proportional to the size of the aerosol scattering coefficient. Because k_{sa} appears both as a multiplicative factor and in the exponent of equation 3.15, higher aerosol implies more scattering and a faster pulse response; therefore, less time is required to collect any given percentage of photocounts.

3. The optical depth is directly proportional to k_{sa} for a given percent return and value of N_{O_3} . From equation 4.1, optical depth varies directly with both the extinction coefficient and the time of observation. Furthermore, rising k_{sa} results in a falling T_f and hence a shorter observation interval. Apparently, the rise in the extinction coefficient caused by the change in the aerosol is sufficient to

λ nm	Percent Return	Minimum T_f (ns)	Mean T_f (ns)	Maximum T_f (ns)
255	50	247	261	290
255	95	632	847	1613
255	99	1035	1531	3745
255	100	2030	2675	6379
315	50	260	274	294
315	95	818	1124	1785
315	99	1424	2278	4313
315	100	2230	3848	7229

Table 4.3: Calculated Values for T_f at $\lambda = 255$ nm and $\lambda = 315$ nm for Various Return Percentages

λ nm	Percent Return	Minimum τ_p	Mean τ_p	Maximum τ_p
255	50	0.02	0.26	0.47
255	95	0.13	0.78	1.26
255	99	0.31	1.37	1.98
255	100	0.52	2.43	3.88
315	50	0.01	0.13	0.24
315	95	0.06	.047	0.77
315	99	0.15	0.88	1.33
315	100	0.26	1.44	2.09

Table 4.4: Calculated Values for τ at $\lambda = 255$ nm and $\lambda = 315$ nm for Various Return Percentages

λ nm	Percent Return	Minimum Counts	Mean Counts	Maximum Counts
255	100	1536	2768	4017
315	100	1151	2694	3987

Table 4.5: Expected Photocount Returns

offset the decreasing $T_{f,p}$ thereby driving up the value of τ_p.

4. As the expected return percentage, p, increases, both $T_{f,p}$ and τ_p increase for any given pair (N_{O3}, k_{sa}). Even for 100% return, the overall optical depth is only about 2 which is still considered to be in the single scatter regime.

When $\lambda = 255$ nm the following observations hold:

1. Due to the strong absorption characteristics of ozone at this wavelength as well as the wavelength-independent aerosol effects, both the end time of the observation interval and the optical depth display dependencies on the aerosol scattering coefficient and the ozone number density.

2. Observation end times are inversely related to the quantity of ozone and aerosol in the atmosphere. The reasoning presented for the $\lambda = 315$ nm case holds here as well.

3. Optical depths vary directly with N_{O_3} and k_{sa} for the same reason as in the 315 nm case.

4. The maximum optical depth required to obtain 100% returns is just under 4. While this figure may be somewhat high to guarantee the validity of the single scatter assumption, the corresponding maximum optical depth for 99% is only about 2.

From the observations presented above, a value of $T_f = 1200$ ns is used in the base configuration of the auxiliary parameter set. This value should allow for expected returns within the 95% to 99% range over most combinations of aerosol and ozone.

Finally, the data in Table 4.5 is useful in obtaining a first order estimate of the average photon arrival rate for the auxiliary parameter configuration under consideration. Define the average arrival rate as the total number of photons collected in a

given time interval divided by the length of the interval. Assuming that the interval is about 1000 ns long and from Table 4.5, the average number of counts is on the order of 2000, then a rough estimate of the average photon arrival rate is 2.0×10^9 counts/sec. This result may pose a problem for two reasons:

1. Because present-day photodetectors saturate at roughly 10^{10} counts/sec, an average arrival rate of 2×10^9 counts/sec is pushing the limits of the state of the art in direct detection receivers.

2. Because the pulse response is exponential in nature, the instantaneous arrival rate of photons at the beginning of the interval will be much greater than 2.0×10^9 counts/sec. Thus, the likelihood of constructing a photodetector capable of resolving photocounts obtained in subintervals of the overall observation period is relatively small.

Despite these two results, the configuration of the single scatter parameters developed in this section satisfy all other constraints imposed both by the nature of the detection system and the single scatter model and will be used as the base configuration for analysis of the ML estimator.

Wavelength Selection

A final issue to be resolved before analysis of the estimator may be undertaken is the choice of the two wavelengths to be used for the investigation. The atmospheric analysis presented in Section 4.2.3 was carried out using $\lambda_{in} = 255$ nm and $\lambda_{out} = 315$ nm. It is not clear however that this selection yields better performance from the estimator than other wavelength pair options.

As discussed in Section 3.5.1, a dual wavelength approach is taken as a means of providing a diversity of information to the estimator concerning the state of the

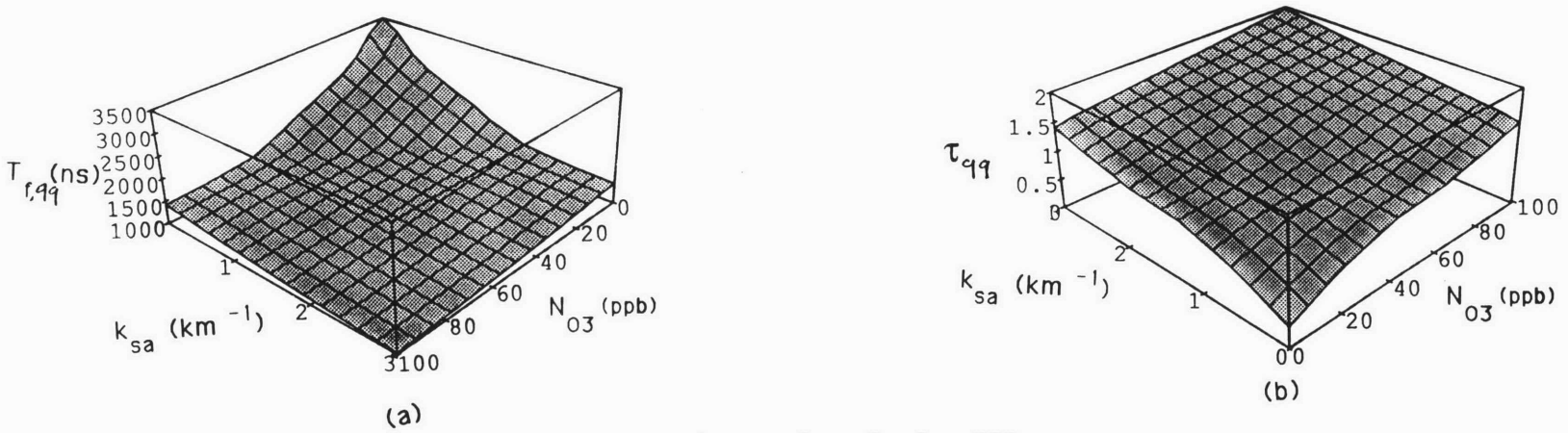

Figure 4-7: $T_{f,99}$ and τ_{99} for $\lambda = 255\ nm$

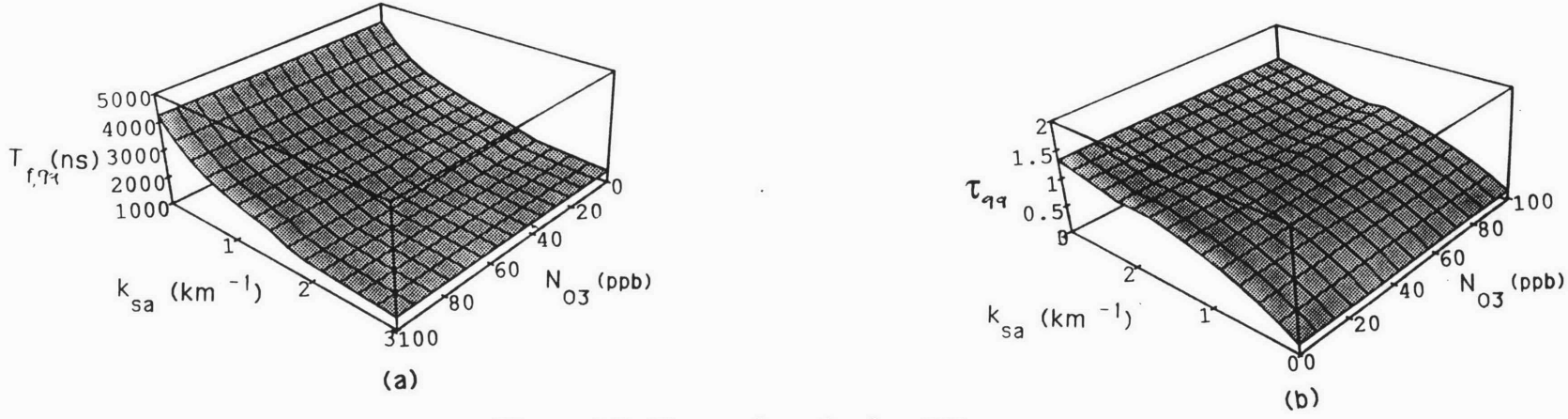

Figure 4-8: $T_{f,99}$ and τ_{99} for $\lambda = 315\ nm$

atmosphere. The strong spectral characteristics of the ozone absorption process indicate that a pulse whose wavelength is far from the peak of the absorption curve (i.e. an "out of band" wavelength) is affected little by the absorption process and more by scattering from aerosols. Thus, the backscattered photocount data from such a pulse conveys much information regarding k_{sa} and relatively little information about N_{O_3} . Alternatively, because an in band pulse is attenuated by both absorption and scattering, backscattered data may say much about the absorption characteristics of the atmosphere; however, this information may be masked by the effects of the aerosol also present at this frequency. Hence, in an effort to determine parameters associated with both ozone absorption and aerosol scattering, an out of band wavelength is used to isolate the effects of the aerosol so that data from an in band wavelength may provide estimates of the molecular absorption parameters. The final choice of a useful wavelength pair reflects a tradeoff between the amount of in band and out of band information necessary to achieve a given level of performance from the estimator.

The exact selection of λ_{in} and λ_{out} is made by examination of Cramer Rao lower bound (CRLB) data for a variety of pair possibilities. Specifically, CRLB results for all pairwise combinations of pulses whose wavelengths are 255 nm, 275 nm, and 315 nm are investigated. The ozone absorption profile is maximum at 255 nm. At 275 nm, the absorption cross section is at 50% of its peak values and at 315 nm, is less than 1% of its 255 nm value. The analysis of the CRLB for the six possible pairings should provide some insight as to how the estimator performs given different degrees of information from in and out of the ozone absorption band.

The following notation is used for CRLB bounds of interest here:

$\sigma^2_{N_{O3},CR}$ The lower bound on the variance of the ozone number density estimate

$\sigma^2_{k_{sa},CR}$ The lower bound on the variance of the aerosol scattering coefficient estimate

$\sigma_{N_{O3},CR}$ The lower bound on the standard deviation of the ozone number density

estimate

$\sigma_{k_{sa},CR}$ The lower bound on the standard deviation of the aerosol scattering coefficient estimate

ρ_{CR} The lower bound on the correlation coefficient between the estimates of N_{O_3} and k_{sa}

The evaluation of possible wavelength pairs is carried out by examination of the minimum, mean and maximum values of $\sigma_{N_{O3},CR}$ and $\sigma_{k_{sa},CR}$ as N_{O_3} is varied between 0 and 100 ppb and k_{sa} assumes values between 0 and 3 km^{-1}.

From Table 4.6, it is evident that the CRLB on the estimate of N_{O_3} is lowest when the in-band pulse is at 255 nm. As the choice of in-band wavelength increases (and the ozone absorption cross section decreases), $\sigma_{N_{O3},CR}$ rises. Thus, the theoretical accuracy of the estimate of the ozone number density appears to be inversely related to the magnitude of the pure absorption coefficient, A_{O3}, associated with the wavelength of the in-band probing pulse. This conclusion makes much sense especially when one considers an alternative problem to the estimation of both N_{O_3} and k_{sa} . If it is assumed that the ozone number density is the only unknown and is to be estimated using a single wavelength system then ${\sigma_{N_{O3},CR}}^2$ is given by:

$$\sigma^2_{N_{O3},CR} = \frac{I_2}{\alpha\gamma c^2 A^2_{N_{O3}} I_1^2} \tag{4.8}$$

where

$$I_1 = \int_{T_s}^{T_f} \int_t^{t-T_p} \frac{\exp\left(-k_e c\tau\right)}{\tau} d\tau dt \tag{4.9}$$

$$I_2 = \int_{T_s}^{T_f} \int_t^{t-T_p} \frac{\exp\left(-k_e c\tau\right)}{\tau^2} d\tau dt \tag{4.10}$$

Hence, the lower bound on the variance varies inversely with A_{O3}. In this case the logical choice for the wavelength is 255 nm. Because the inverse relationship evidently

λ_{in} (nm)	λ_{out} (nm)	Minimum $\sigma_{N_{O3},CR}$ (ppb)	Mean $\sigma_{N_{O3},CR}$ (ppb)	Maximum $\sigma_{N_{O3},CR}$ (ppb)
255	255	4.93	7.07	10.53
255	275	6.04	8.19	11.50
255	315	5.90	7.37	9.57
275	275	10.21	14.02	20.64
275	315	12.08	14.77	19.30
315	315	1478	2017	3123

Table 4.6: Minimum, Mean, and Maximum Values of $\sigma_{N_{O3},CR}$ for Various Wavelength Pairs

λ_{in}(nm)	λ_{out} (nm)	Minimum $\sigma_{k_{sa},CR}$ (ppb)	Mean $\sigma_{k_{sa},CR}$ (ppb)	Maximum $\sigma_{k_{sa},CR}$ (ppb)
255	255	0.055	0.087	0.122
255	275	0.043	0.073	0.106
255	315	0.025	0.049	0.076
275	275	0.045	0.074	0.103
275	315	0.024	0.048	0.073
315	315	0.032	0.058	0.082

Table 4.7: Minimum, Mean, and Maximum Values of $\sigma_{k_{sa},CR}$ for Various Wavelength Pairs

carries over to the two parameter/ two wavelength problem, the in-band wavelength for this investigation is fixed at 255 nm.

The data in Table 4.7 demonstrates that the value of k_{sa} may be estimated with relatively high accuracy regardless of the choice of wavelengths. While the lower bound on the variance of k_{sa} is not overly sensitive to wavelength selection, better performance may result as the distance of the out of band wavelength from 255 nm is increased. Hence, $\lambda_{out} = 315\ nm$ will be the initial choice for the second element of the wavelength pair. From Table 4.8, the use of $(\lambda_{in}, \lambda_{out}) = (255, 315)$ produces estimates for which the lower bound on the correlation coefficient is lowest of all pairs tested.

λ_{in} (nm)	λ_{out} (nm)	Minimum ρ_{CR} (ppb)	Mean ρ_{CR} (ppb)	Maximum ρ_{CR} (ppb)
255	255	0.61	0.72	0.80
255	275	0.58	0.67	0.72
255	315	0.34	0.38	0.40
275	275	0.65	0.74	0.80
275	315	0.42	0.45	0.46
315	315	0.69	0.76	0.82

Table 4.8: Minimum, Mean, and Maximum Values of ρ_{CR} for Various Wavelength Pairs

4.3 Maximum Likelihood Performance

4.3.1 Introduction

Having established reasonable values for the plethora of auxiliary parameters associated with the single scatter propagation model, evaluation of the actual performance of the maximum likelihood estimator may be undertaken. This assessment is made using two tools:

1. Cramer-Rao lower bound data on the variances, standard deviations and correlation coefficient associated with an unbiased ML estimator

2. Data obtained from Monte Carlo simulations using the Maximum Likelihood estimator.

The Cramer Rao lower bound provides an easy to calculate indication of performance under the assumption that the estimator is unbiased. CRLB information is obtained by evaluation of the inverse Fisher matrix, 3.48, for the same grid of points in the (N_{O3}, k_{sa}) plane used to evaluate T_f in section 4.2.3. This calculation is completed in under 2 minutes of computer time on a Vax 6800. Alternatively, the Monte-Carlo approach involves use of the ML algorithm in generating actual estimates of the parameter vector base upon computer generated Poisson data points. For the

set of (N_{O3}, k_{sa}) points used above, slightly more than 24 hours of computer time is needed to generate the Monte-Carlo data. The advantage of the Monte Carlo approach is its ability to demonstrate the "real" performance of the estimator. Bias information is generated so as to justify any conclusions which may be based upon the CRLB calculations which provide information about the performance of unbiased estimators. Furthermore, actual mean square error and correlation data is generated against which the Cramer Rao bound results may be compared.

In addition to the statistical information obtained via the CRLB and Monte-Carlo programs it is useful to define an additional performance measure: relative accuracy. This quantity is defined as the ratio of the standard deviation in the estimate to the actual value of the parameter. The relative accuracies in the estimates of N_{O_3} and k_{sa} are given by:

$$\delta_{N_{O3}} \equiv \frac{\sigma_{N_{O3}}}{N_{O3}} \tag{4.11}$$

and

$$\delta_{k_{sa}} \equiv \frac{\sigma_{k_{sa}}}{k_{sa}} \tag{4.12}$$

where

- $\delta_{N_{O3}}$ is the relative accuracy in the estimate of N_{O_3}
- $\sigma_{N_{O3}}$ is the standard deviation in the estimate of N_{O_3}
- N_{O_3} is the real value of the ozone number density
- $\delta_{k_{sa}}$ is the relative accuracy in the estimate of k_{sa}
- $\sigma_{k_{sa}}$ is the standard deviation in the estimate of k_{sa}
- k_{sa} is the real value of the aerosol scattering coefficient

This calculation normalizes the standard deviation information to the true value of the parameter being estimated in an effort to provide an indication as to the percentage

error one may expect from the estimator. Values of $\delta_{N_{O3}}$ and $\delta_{k_{sa}}$ obtained from CRLB data are denoted by $\delta_{N_{O3},CR}$ and $\delta_{k_{sa},CR}$ respectively.

The remainder of this section is devoted to examination and analysis of CRLB and Monte-Carlo data obtained using a variety of configurations of the auxiliary parameter set. First, the values of the parameters determined in Section 4.2 are used as a reference point against which the performance may be compared for alternative configurations of the parameter set. After this preliminary investigation, some parametric analysis is presented. Here, elements of the auxiliary parameter set are varied from their base values to explore the manner in which the estimator's performance is affected by deviations from the the initial parameter configuration.

4.3.2 The Base Case: A Nice Place to Start

Recall that the base configuration of the auxiliary parameter set is:

$$\begin{array}{ccc} \theta_t = 10^\circ & \theta_t = 10^\circ & Q_p = 10^4 \text{ W} \\ T_p = 100 \text{ ns} & T_s = 180 \text{ ns} & T_f = 1200 \text{ ns} \\ \lambda_{in} = 255 \text{ nm} & \lambda_{out} = 315 \text{ nm} & \xi = 0.01 \\ g = 0.72 & f = 0.5 & \text{Area} = 1 \text{ cm}^2 \end{array}$$

Figure 4-9(a) shows that the value of $\sigma_{N_{O3},CR}$ is relatively constant regardless of variations in N_{O_3} and k_{sa} . Furthermore, for a wide variety of actual atmospheric conditions, Figure 4-10(a) demonstrates that the lower bound on the relative accuracy in the estimates of N_{O_3} is well below 20%. This happy state of affairs is repeated in Figures 4-9(b) and 4-10(b) where the same information regarding the estimates of the aerosol scattering coefficient is presented.

The Monte-Carlo simulations support the conclusion drawn from the Cramer Rao lower bound calculations. The bias surfaces shown in Figures 4-11(a) and 4-11(b) show that the ML estimator is only slightly biased. From comparison of the RMS

error results in Figures 4-12(a) and 4-12(b) to the CRLB on the standard deviations (Figures 4-9(a) and 4-9(b)) it is evident that the ML algorithm produces estimates which are close to the Cramer-Rao bound. In some instances, the mean square error of the ML estimator is slightly less than that predicted by the CRLB. This situation arises due to the bias of the estimator. While the CRLB assumes an unbiased estimator, the ML estimator in this problem does possess some small bias. Thus, there exists points in the (N_{O_3} , k_{sa}) plane where the unbiased-CRLB may not provide an exact lower bound.

Finally, in Figures 4-13(a) and 4-13(b), the variation in the value of the correlation coefficient is graphed as a function of N_{O_3} and k_{sa} . The relatively small values obtained from both the Cramer-Rao bound and the simulation indicates that the choice of using $\lambda_{in} = 255$ nm and $\lambda_{out} = 315$ nm is useful in decoupling the effects of ozone absorption from those of aerosol scattering.

4.3.3 Parametric Analysis: Variations on a Theme

While the performance of the maximum likelihood estimator under the base setup of the auxiliary parameter set is encouraging, it is important to understand how variations from these initial values affect this behavior. Such variations may arise from one of two sources. First, the parameters may be set deterministically by the user of the system to values which yield improved performance over the base set of values. It is assumed that all quantities associated with the transmitter/receiver (T_p, T_s, T_f, ξ, etc.) fall into this category. Alternatively, it may be the case that the user assumes nominal values for some parameters whose actual values are determined by external forces. For example, the values of g and f of the Heney-Greenstein phase function are assumed so as to obtain some approximation to the actual aerosol scattering phase function. In reality, the shape of this function may be better described by different choices for g and f. This incorrect choice in the parameterization of the phase func-

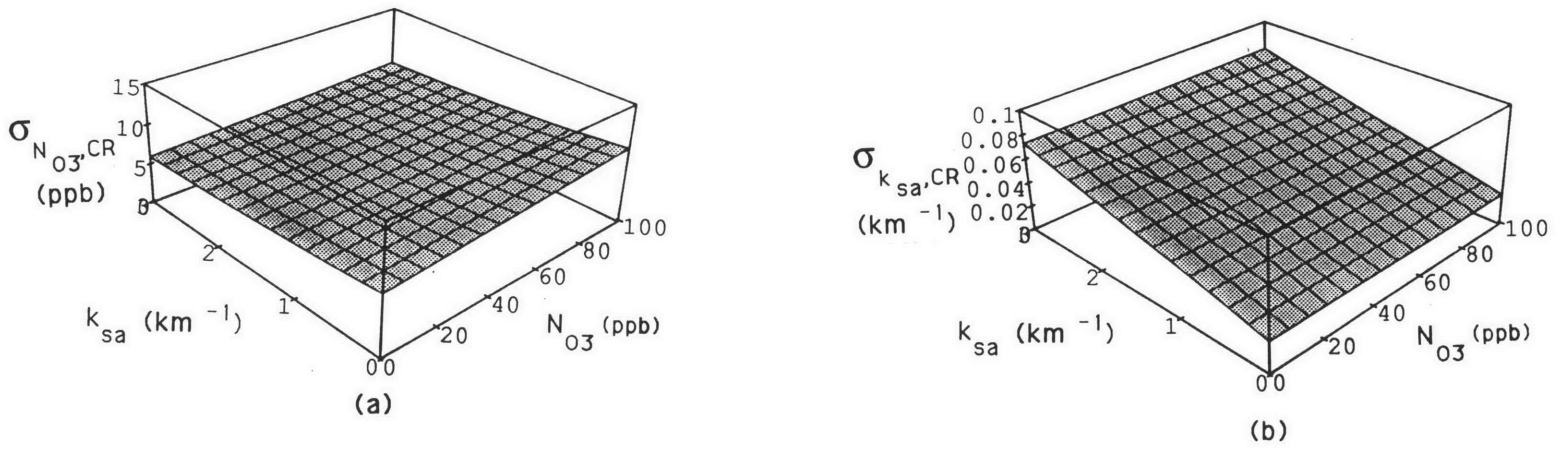

Figure 4-9: CRLB Results for Base Configuration

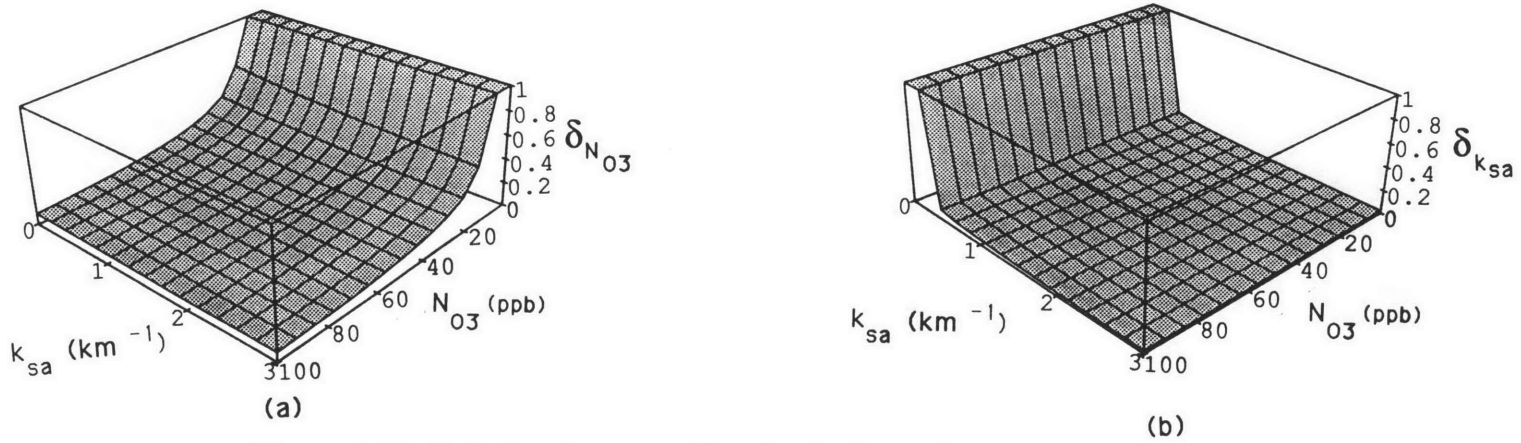

Figure 4-10: Relative Accuracy Results for Base Configuration

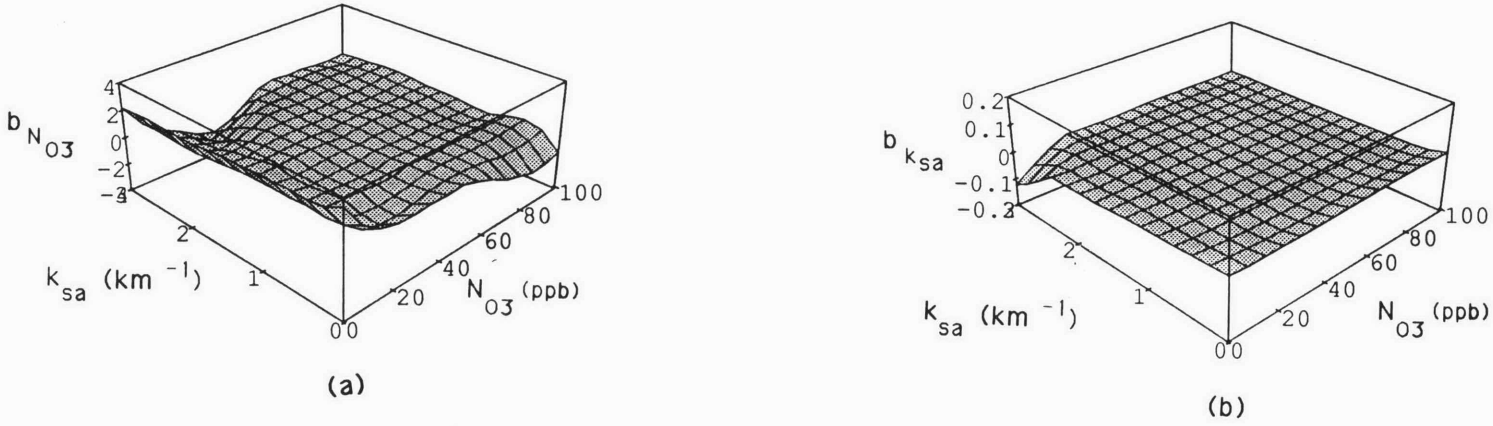

Figure 4-11: Monte Carlo Bias Results for Base Configuration

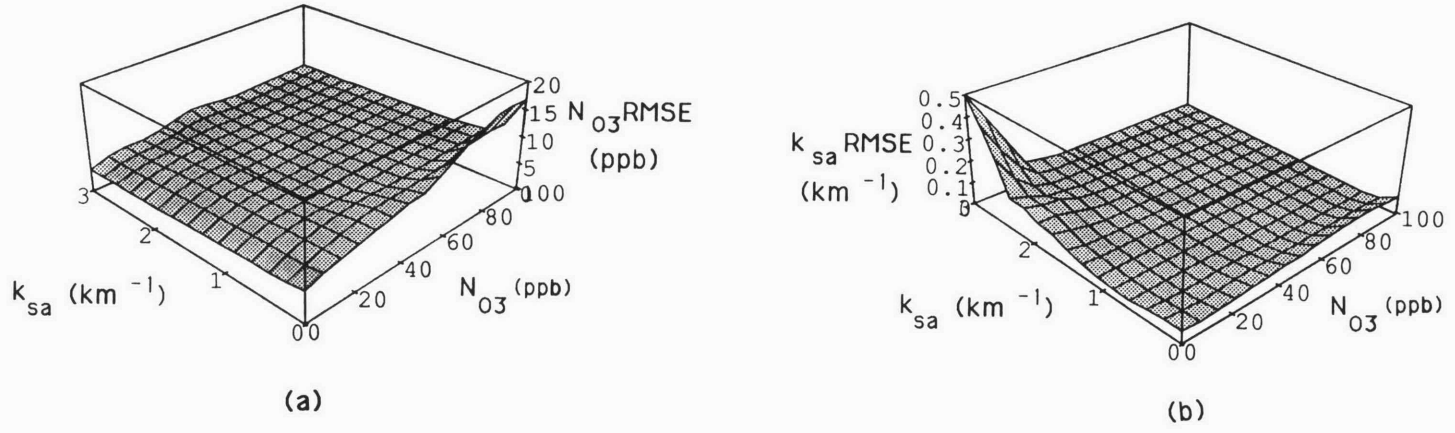

Figure 4-12: Monte Carlo RMSE Results for Base Configuration

tion may affect the ML estimator's performance; however, the errors which result may be overcome without adding the unknown quantity to the vector of parameters being estimated. Such a situation would indicate some robustness in the ML estimator.

In this section, the impact of both forms of auxiliary parameter alteration is explored. Undertaking this analysis for all of the quantities in the auxiliary parameter set is beyond the scope of this thesis. Rather, the effects of changing T_s, T_p, T_f, and g to the values listed in Tables 4.3.3 are presented: From Equation 3.15, the expected

Parameter	Low Value	Base Value	High Value	Units
T_s	16	80	260	ns
T_f	270	1200	3000	ns
T_p	10	100	1000	ns
g	0.66	0.72	0.74	-

Table 4.9: Alternate Values for Auxiliary Parameter Set

number of backscattered photocounts is directly proportional to quantities such as the area of the receiver and the detection efficiency. Variations in these parameters would have somewhat predictable results and are not included in this investigation. The effects of changes in the three timing parameters (T_p, T_s, and T_f) are not quite as clear due to the exponential nature of the atmospheric pulse response. Furthermore, the variation of the Heney-Greenstein g parameter with atmospheric conditions makes it a likely source of error.

The low and high values of the parameters are motivated by the following considerations:

1. The start time of observation was initially chosen to avoid swamping the detector with radiation that has scattered from distances relatively close to the transmitter/receiver as is often done in lidar systems (Section 4.2.1). Changing T_s to 116 ns corresponds to a delay range of 5 m rather than 25 m for $T_p = 100$

ns. In this case the initial count rates will be very high, but many more counts will be collected. On the other hand, doubling T_s to 260 ns should drive down count rates thereby easing the burden on the receiver but forcing the estimator to work with less data.

2. The changes in T_f are suggested by the analysis presented in Section 4.2.3. For $T_f = 270$ ns, around 50% of the expected photocounts should be collected under most atmospheric conditions. The high value of $T_f = 3000$ ns should ensure a 99% collection figure for most values of N_{O_3} and k_{sa} of interest in this investigation.

3. The high and low values for T_p are chosen to see how order of magnitude changes in this parameter affects the estimator

4. The low value of the Heney-Greenstein g parameter corresponds to the phase function found in a rural haze while the high setting represents maritime conditions [63].

The remainder of this section is devoted to the analysis of the many and varied arrangements of the auxiliary parameter set presented in Table 4.3.3. For all changes except those to the phase function parameter, data from both CRLB and Monte-Carlo simulations are available. Alterations in the g parameter are meant to simulate the case where the assumed value of a modeled parameter differs from its real world value. In this case, only Monte-Carlo simulations are performed. The simulated data upon which the ML estimator operates is generated using the high or low values of g. The estimator uses this data but assumes that the values of the auxiliary parameters correspond to the base configuration where $g = 0.72$. Finally, the surface plots of ρ and ρ_{CR} do not vary significantly from the base case for the changes in the auxiliary parameter set to be considered here. Hence, detailed analysis of these quantities is not presented.

Changing T_s: Starting things off right

Because the atmospheric pulse response is singular at time $t = 0$, unusually high numbers of counts may be observed for periods close to this time origin. Alteration in the start time of the observation interval determines how much of this initial surge is made available to the estimator. It would seem that increasing the number counts should yield improved performance of the estimator. Similarly, waiting longer periods of time should produce poorer results.

From Figures 4-14(a) and 4-15(a) it is evident that the CRLB on the standard deviation of the estimate of N_{O_3} is not noticeably affected by alterations in T_s. In both cases, the error surfaces are roughly identical to the base case (Figure 4-9(a).) On the other hand, $\sigma_{k_{sa},CR}$ demonstrates greater sensitivity to selection of T_s. Comparing Figure 4-14(b) to Figure 4-9(b) indicates that starting the observation interval 16 ns after the falling edge of the pulse improves the CRLB on the estimate of the aerosol scattering coefficient. Likewise, doubling T_s to 260 ns has a negative impact on $\sigma_{k_{sa},CR}$ (Figure 4-15(b)).

The Monte-Carlo simulations show little difference in the performance of the estimator from the base case as T_s varies. In both cases, the estimator remains relatively unbiased (Figures 4-16 and 4-17). Moreover, the RMS error data in Figures 4-18 and 4-19 show little change from the corresponding information generated using the base configuration.

The small degree of sensitivity in the CRLB to changes in T_s is understood best in light of the time dependency of the information contained in the backscattered radiation. In Section 3.5.1, it was noted that photocounts collected for times close to the falling edge of the pulse would have suffered little molecular absorption. Instead, they would bear more information concerning the state of the aerosol in the atmosphere. Therefore, modulation of T_s is equivalent to changing the quantity of data relating to k_{sa} available to the estimator. Low values of T_s result in more "aerosol

photocounts" in the observation vector and better estimates of this parameter. The converse holds true as T_s is increased.

While $\sigma_{k_{sa},CR}$ is sensitive to changes in the start time of the observation interval, $\sigma_{N_{O3},CR}$ is not affected by alterations in T_s. Again, from Section 3.5.1, information regarding atmospheric ozone is obtained by collecting photons for periods long after T_p. Keeping T_f fixed as T_s changes ensures that about the same quantity of ozone information was available in this case as in the base case. Hence, variations in T_s had little impact on ability to estimate N_{O_3} .

Lowering T_s may improve the performance of the estimator, at the price of a greater burden on the detection capabilities of the receiver. The choice of T_s was motivated initially by a desire to avoid saturating the receiver with photocounts for times close to the falling edge of the probing pulse. Using the definition for mean count rate presented in Section 4.2.3, Table 4.10 presents the minimum, mean, and maximum count rates for the base case, low T_s, and high T_s configurations of the auxiliary parameter set as N_{O_3} varies between 0 and 100 ppb and k_{sa} assumes values from 0 to 3 km^{-1}. In most cases, expected counts rates are in the range of 10^9 to 10^{10} counts per second. These figures are pushing the limit of existing detector technology but are not outrageous. Thus, lowering T_s in order to improve the estimates of k_{sa} may be accomplished at a reasonable price with respect to detector requirements.

Alterations in T_f: When will it all end?

In addition to varying T_s, modification of T_f may be used to alter information available to the estimator. Increasing the value of this parameter increases the number of collected photocounts and should improve the quality of the estimates. Alternatively, shorter collection times are likely to result in poorer performance. These anticipated results are borne out by both the CRLB calculations and Monte-Carlo simulation.

Figure 4-20 demonstrates that decreasing T_f negatively impacts the CRLB on the

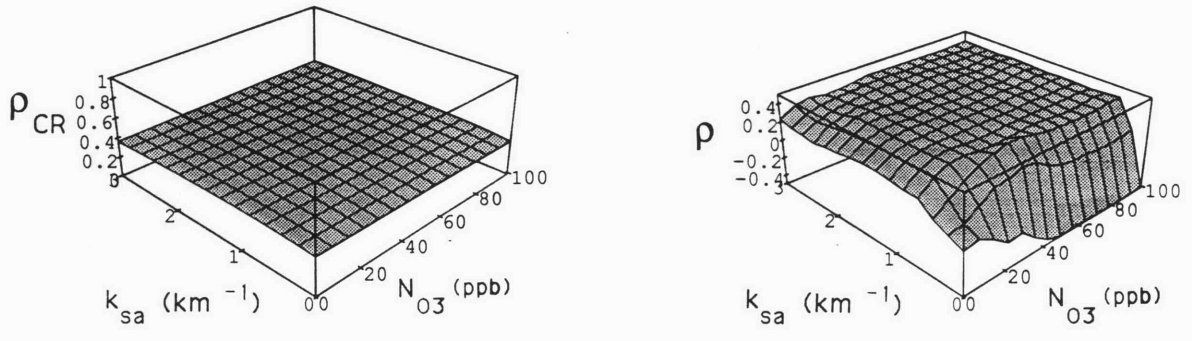

(a) (b)

Figure 4-13: CRLB and Monte Carlo Correlation Coefficient Results for Base Configuration

T_s (ns)	λ (nm)	Minimum Rate 10^{10} counts/sec	Mean Rate 10^{10} counts/sec	Maximum Rate 10^{10} counts/sec
116	255	0.15	0.27	0.39
	315	0.10	0.25	0.38
180	255	0.42	0.76	1.11
	315	0.26	0.68	1.08
260	255	0.08	0.14	0.20
	315	0.06	0.14	0.20

Table 4.10: Counts Rate Data For Different Values of T_s

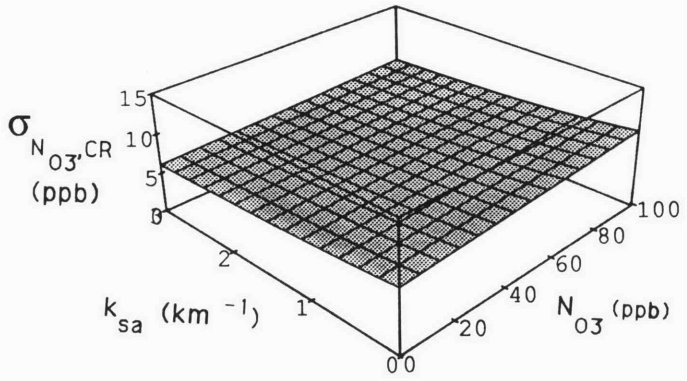

(a)

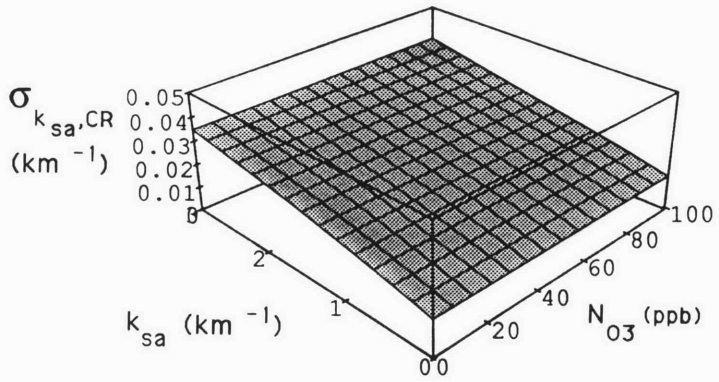

(b)

Figure 4-14: Cramer Rao Bound Results for $T_s = 116\ ns$

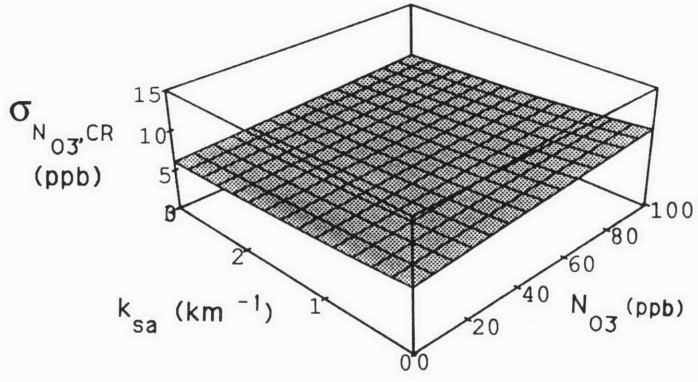

(a)

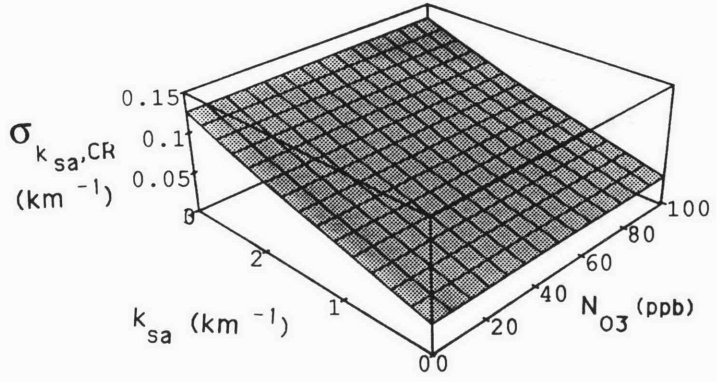

(b)

Figure 4-15: Cramer Rao Bound Results for $T_s = 260\ ns$

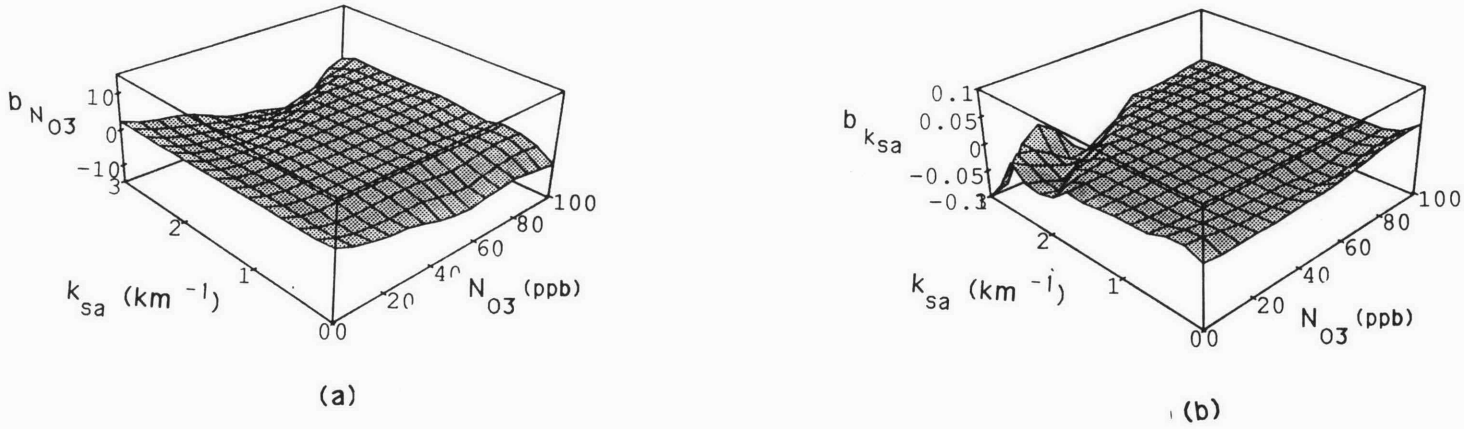

Figure 4-16: Monte Carlo Bias Results for $T_s = 116\ ns$

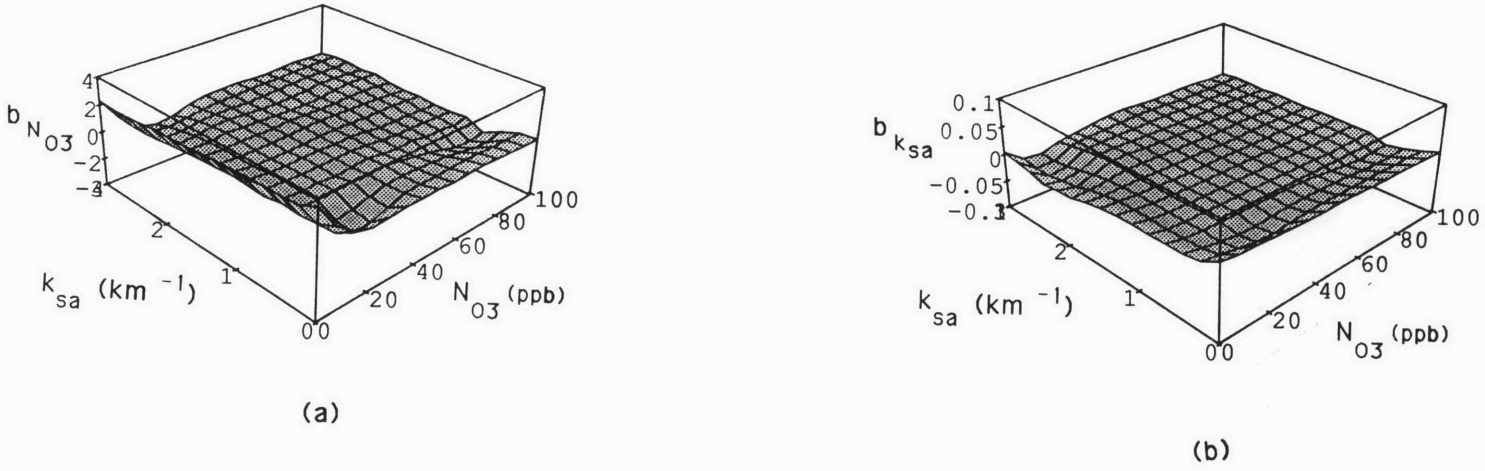

Figure 4-17: Monte Carlo Bias Results for $T_s = 260\ ns$

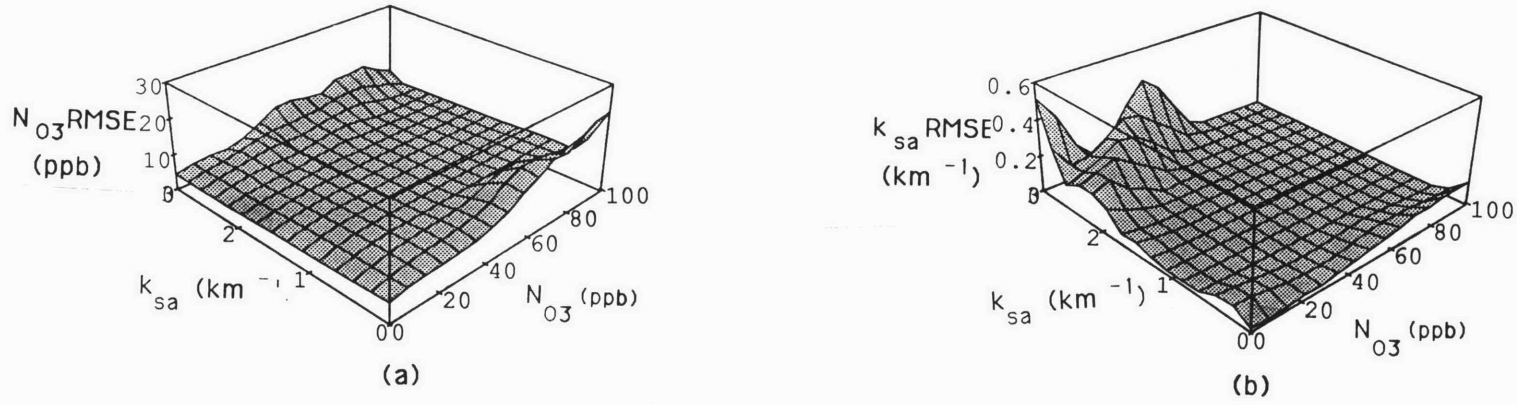

Figure 4-18: Monte Carlo RMS Error Results for $T_s = 116\ ns$

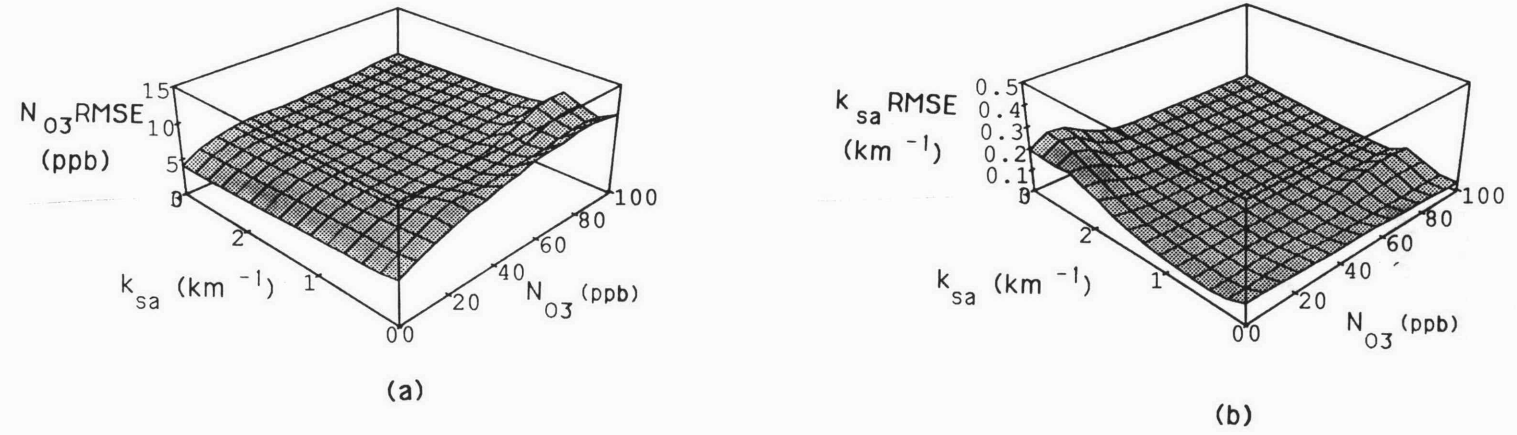

Figure 4-19: Monte Carlo RMS Error Results for $T_s = 260\ ns$

estimates of both N_{O_3} and k_{sa} . The standard deviation in the estimate of the ozone number density roughly triples from the base case. While the corresponding bound on k_{sa} is not as severely affected, it is worsened by the short observation interval. Comparison of Figure 4-21 to 4-9(a,c) show that increasing T_f to 3500 ns improves the ability to estimate N_{O_3} but has relatively little effect on the aerosol estimates.

As expected, Monte-Carlo simulations demonstrate that lowering the value of T_f has an adverse effect upon the performance of the estimator while the higher value of this parameter leads to both lower bias as well as a decrease in the root mean square error. From Figure 4-23, setting $T_f$to 270 ns increases the bias of the N_{O_3} estimates as much as fivefold over the base case while leaving the aerosol bias relatively unchanged. Similarly, the root mean square error in the ozone number density estimate (Figure 4-24(a)) is doubled in comparison to the base case for the low value of T_f. Furthermore, lowering the end time of the observation interval has significant effects upon the RMS error in the estimate of the aerosol scattering coefficient. Comparing Figure 4-24 to 4-12 and 4-20(b) clearly shows that for higher values of k_{sa} :

1. The error in the estimate of this quantity increases in comparison to the base case

2. The efficiency in the estimate of k_{sa} suffers

Shortening the observation interval results in less data being made available to the estimator. This effect in conjunction with the higher extinction coefficient associated with larger values of k_{sa} appears to have a larger impact on the error in the estimates of the aerosol scattering coefficient than any seen in the preceding analysis and experiments.

For the higher value of T_f, the Monte-Carlo simulations show some improvement in performance over the base configuration of the auxiliary parameter set. The bias data in Figure 4-23 is about the same in this case as in the base case. Moreover, the

root mean square error results generated by the simulations is slightly better as $T_f$is increased to 3000 ns (compare Figures 4-12 an 4-25.)

The effects of changing T_f on the estimates of N_{O_3} and k_{sa} are somewhat dual to those of changing T_s. Altering the start time of the observation was tantamount to changing the quantity of aerosol information available to the estimator. Similarly, changing T_f may be viewed as a way of controlling the quantity of ozone-related information contained in the observation vector while keeping the data about k_{sa} relatively constant. Lowering T_f results in fewer ozone photocounts and worse estimates of the number density. The converse holds true as T_f is raised.

As was discussed in Section 4.2.3, the observation interval needs to be kept short enough to guarantee the validity of the single scatter assumption. Higher values of T_f mean that more multiply scattered photons are collected. Because these additional counts are not factored into the ML estimator's propagation model, the estimates may be negatively impacted. To avoid analysis of this situation, it was assumed that the single scatter model could be considered accurate for optical depths less than 5. Increasing T_f to 3000 ns results in a maximum optical depth of just under 1.5 as N_{O_3} and k_{sa} are varied over their respective domains of interest. From this, it may be concluded that values of T_f greater than 1200 ns may be used without worry as to compromising the validity of the single scatter assumption.

Variations in T_p: A Probing Investigation.

Changing the length of the transmitted pulse affects the estimator in two ways. First, because the number of transmitted photons is dependent upon T_p, the absolute quantity of collected backscattered photons rises and falls with variations in the duration of the pulse. More subtly, changing T_p requires alterations in both T_s and T_f. If $T_p = 1000$ ns, then assigning values of 180 ns and 1200 ns to T_s and T_f would not be possible in the first case nor prudent in the second. Thus, variations in the pulse

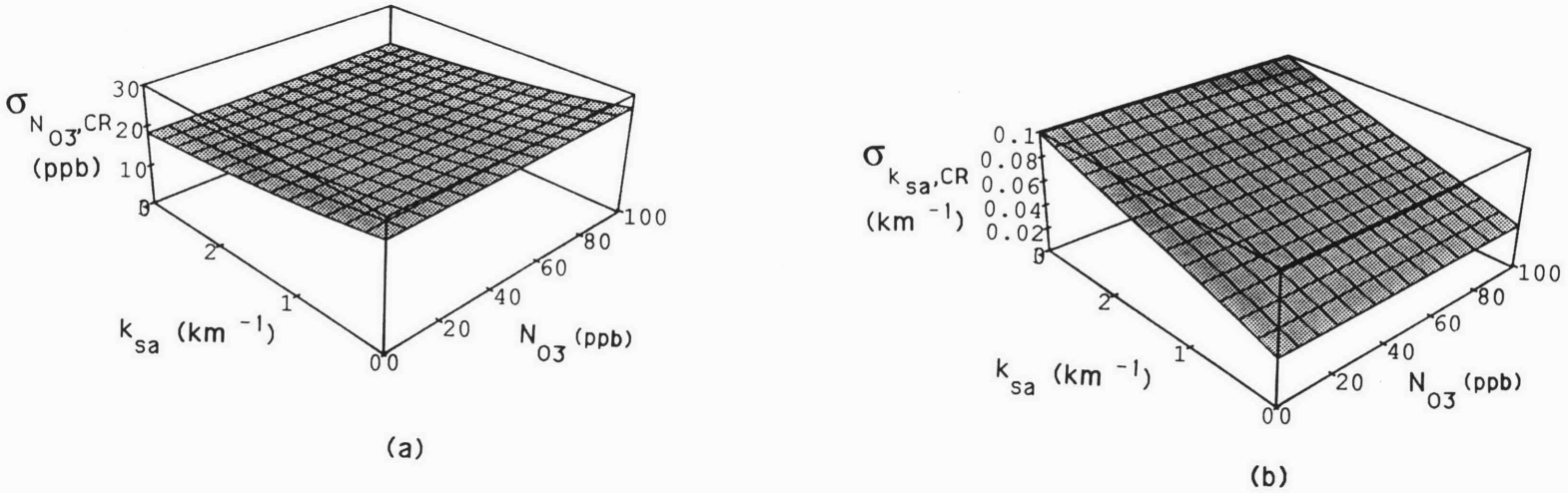

Figure 4-20: Cramer Rao Bound Results for $T_f = 270\ ns$

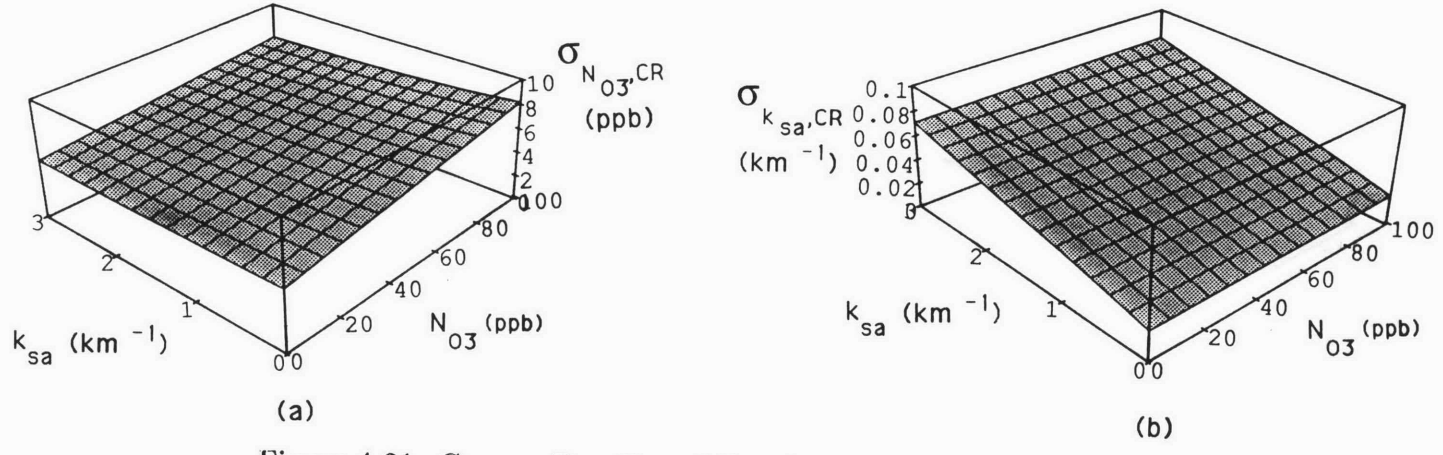

Figure 4-21: Cramer Rao Bound Results for $T_f = 3000\ ns$

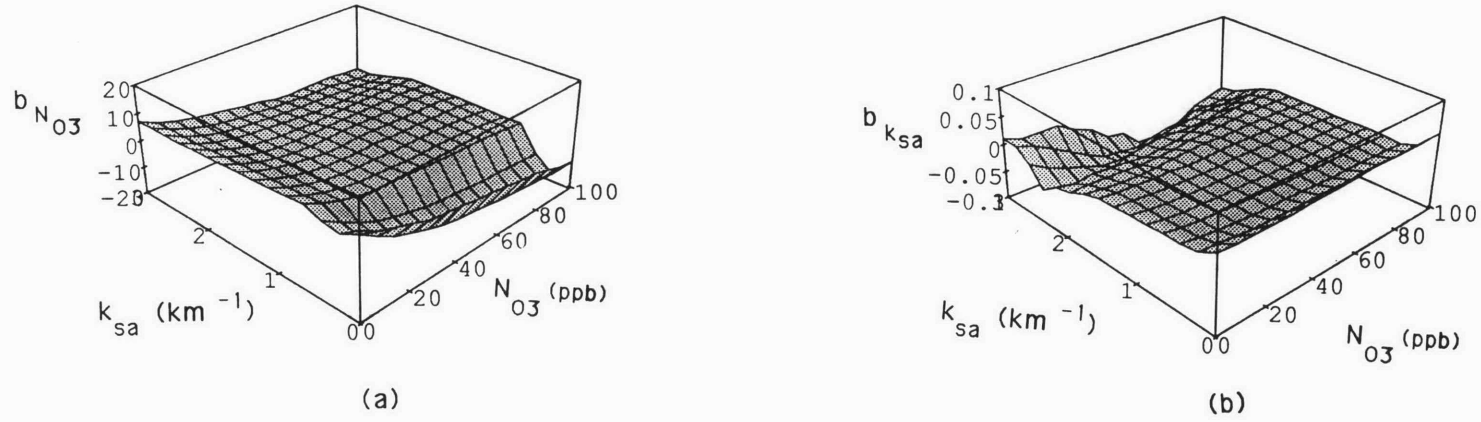

Figure 4-22: Monte Carlo Bias Results for $T_f = 270\ ns$

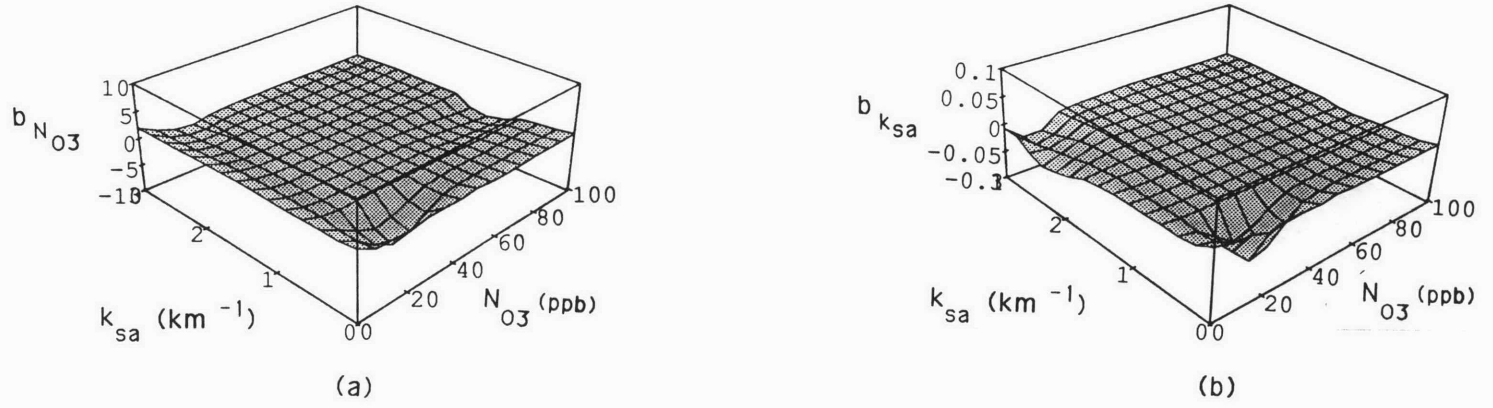

Figure 4-23: Monte Carlo Bias Results for $T_f = 3000\ ns$

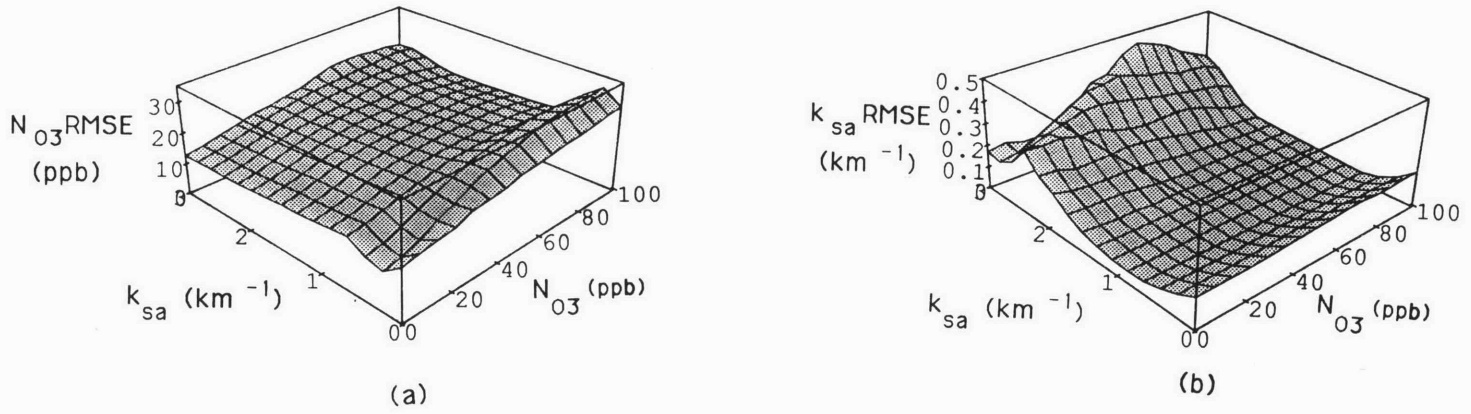

Figure 4-24: Monte Carlo RMS Error Results for $T_f = 270\ ns$

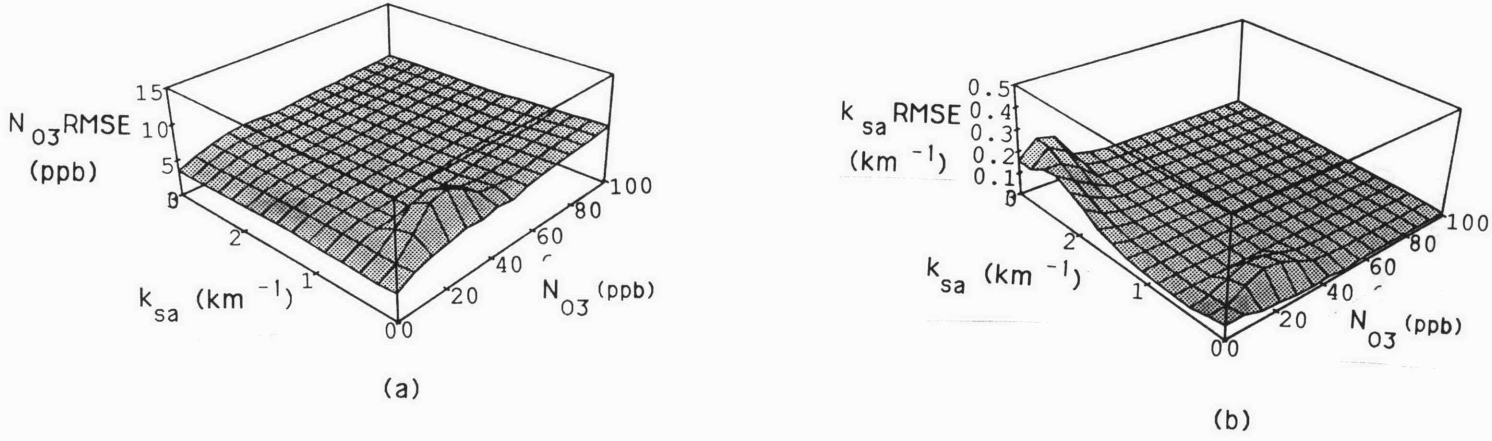

Figure 4-25: Monte Carlo RMS Error Results for $T_f = 3000\ ns$

length require that the observation interval also be adjusted.

From Section 4.2, the choices of T_s and T_f were influenced by the choice of T_p. The start time was chosen so that transmitted photons could travel a distance of at least 25 m from the transmitter/receiver. Furthermore, T_f was selected to ensure that approximately 95% of the backscattered photons that would arrive at the receiver as $t \rightarrow \infty$ actually were collected. To achieve these two criteria as T_p is varied above and below its base values, T_s and T_f are altered according to Table 4.11.

T_p	T_s	T_f
10	90	1200
1000	1080	3500

Table 4.11: Configurations of T_s and T_f as T_p Is Varied

When T_p is shortened to 10 ns, the ability to estimate N_{O_3} and k_{sa} deteriorates as shown in Figure 4-26. This degeneration is attributed to two causes. First, as was put forth previously, fewer photons are available for collection. Second, by waiting the full 80 ns to start the observation interval, the pulse response has dropped to a much lower point than was the case for the initial configuration of the auxiliary parameters. Further investigation using a shorter delay time with shorter pulses may result in a (T_p, T_s) combination for which performance measures are not so badly affected. In this case, sufficiently accurate estimates could be generated using a lower power transmitter.

Figure 4-27(a) demonstrates that increasing T_p to 1000 ns greatly aids in estimating N_{O_3} . Comparison of Figures 4-21(a) and 4-27(a) show that greater improvement in estimating N_{O_3} results from altering both T_p and T_f than is seen when only T_f was raised. This result may be attributed to the higher number of backscattered photocounts obtained by raising T_p as well as increasing the length of the observation interval by elevating T_f. Table 4.12 provides photocount statistics for the base case as well as the situations where only T_f is raised and when both T_f and T_p are increased.

Configuration	λ (nm)	Minimum Counts	Mean Counts	Maximum Counts
Base	255	1509	2714	3999
	315	1053	2600	3917
Only T_f increased	255	1536	2769	4073
	315	1126	2689	3994
Both T_f and T_p	255	3320	6038	8854
increased	315	3236	6519	8776

Table 4.12: Counts Rate Data For Different Values of T_s

A higher value of T_f results in a slightly greater number of backscattered photocounts than in the base case. This was reflected in a modest improvement in the estimate of the ozone number density when T_f was elevated. When both T_f and T_p are increased, roughly, a threefold increase is seen in the expected number of collected photocounts resulting in $\sigma_{N_{O3}}$ dropping to about one third of its initial value. Thus, collecting backscattered photons for longer periods of time (by raising T_f) and having more counts collected in these intervals (by augmenting T_p) is a most effective means of improving the estimates of the ozone number density.

Figure 4-27(b) indicates that the estimate of k_{sa} is affected only marginally by raising T_p. Apparently, no significant increase in information regarding the state of aerosol results when the duration of the pulse is increased. As seen in Section 4.3.3, the aerosol estimate is most sensitive to changes in the delay between T_p and T_s. As T_p was altered, T_s was set so that a constant 80 ns delay existed between the falling edge of the pulse and the start of the observation interval. Perhaps decreasing the delay while increasing T_p would yield improved performance in the estimate of the aerosol scattering coefficient.

The Monte-Carlo simulations for the two parameterizations considered here both support the conclusions drawn based upon the CRLB analysis. Figures 4-28 and 4-29

show that the bias in the estimates of both N_{O_3} and k_{sa} is inversely proportional to the pulse length. As has been the case before, the statistics for the ozone number density seem to be more sensitive to the changes in the parameter configuration than those of the aerosol scattering coefficient. The root mean square error results shown in Figures 4-30 and 4-31 demonstrate that alterations in the pulse length yield an estimator with fairly small root mean square error. The only exception to this observation is in the RMSE of the k_{sa} estimate in the case of the low T_p parameterization. Under these circumstances, the error in the estimate of k_{sa} is much higher than the CRLB. This phenomenon was seen previously when T_f was decreased. It is assumed that the same explanation described in the low T_f case holds here as well.

The Heney-Greenstein Phase Function Parameter

The above three sections have dealt with deliberate variations of parameter values so as to achieve improved performance from the estimator. A different situation may occur for those parameters whose values are determined by forces other than the will of the user. Here, the nominal values assumed in the model may differ from the true value as they exist in nature. In this case, the photocount data upon which the estimates are based is generated from a process defined by the correct parameter values. The ML algorithm uses this data in conjunction with a model parameterized by false values. Thus, this test is intended to examine the robustness of the ML estimator to unavoidable modeling errors.

To be explored here is the case when an incorrect choice of the g parameter in the Heney-Greenstein phase function is assumed. In the case of the single scatter model, the Heney-Greenstein function is used as an approximation to the aerosol phase function for a variety of atmospheric conditions. Throughout this investigation, g has taken the value of 0.72 which corresponds to atmospheric conditions between rural and maritime hazes [63]. Rural hazes are best described by $g = 0.67$ while

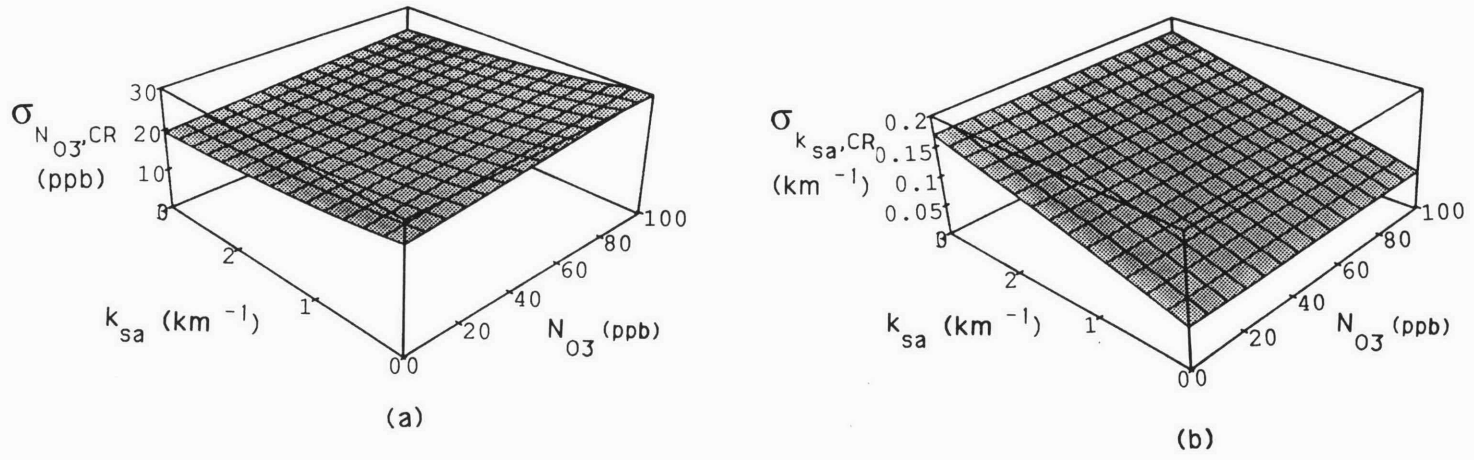

Figure 4-26: Cramer Rao Bound Results for $T_p = 10\ ns$

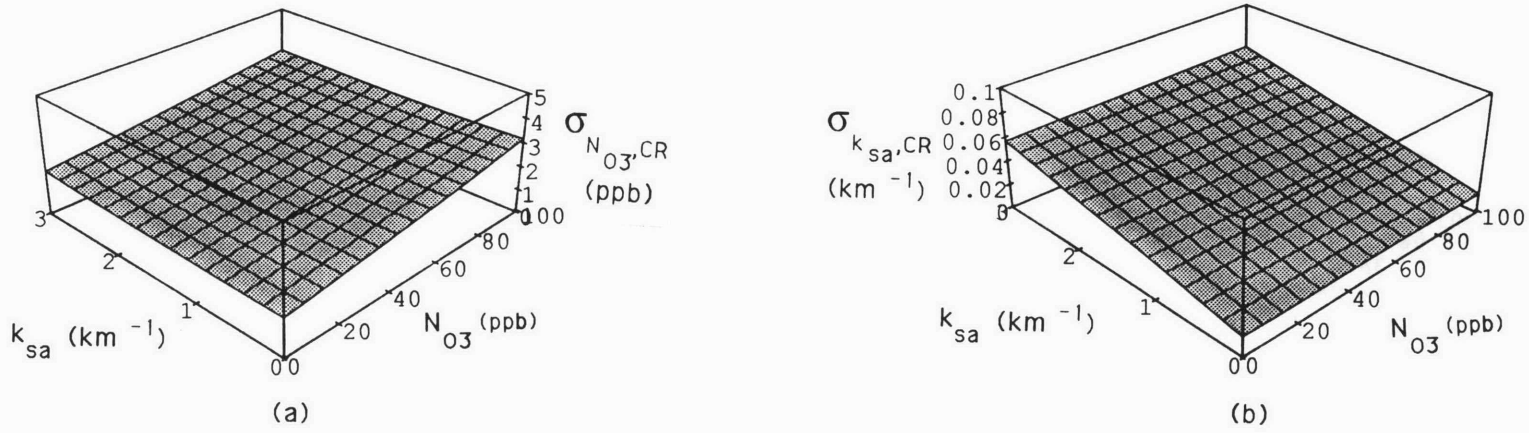

Figure 4-27: Cramer Rao Bound Results for $T_p = 1000\ ns$

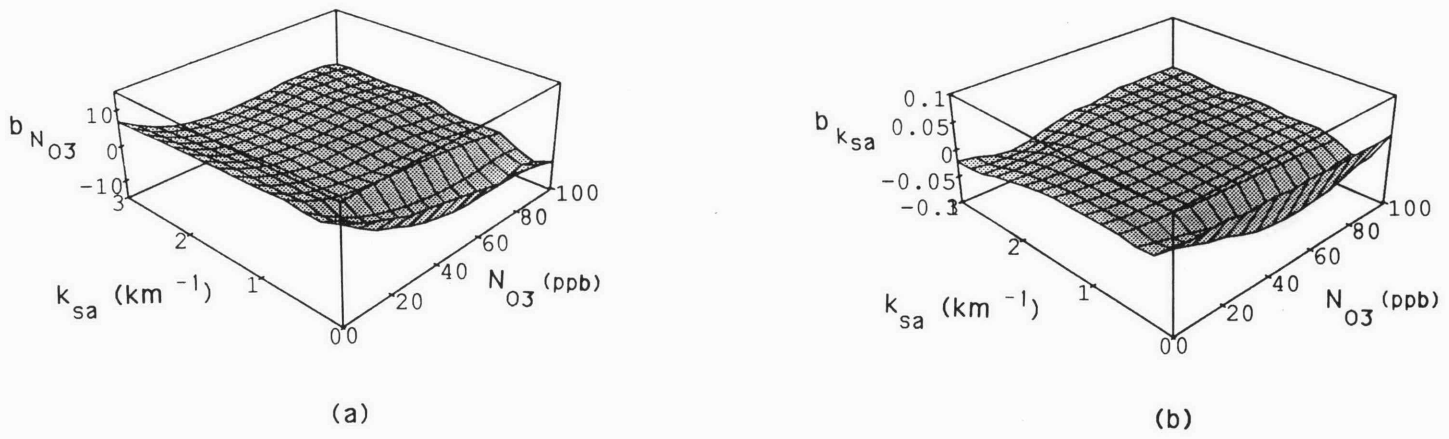

Figure 4-28: Monte Carlo Bias Results for $T_p = 10\ ns$

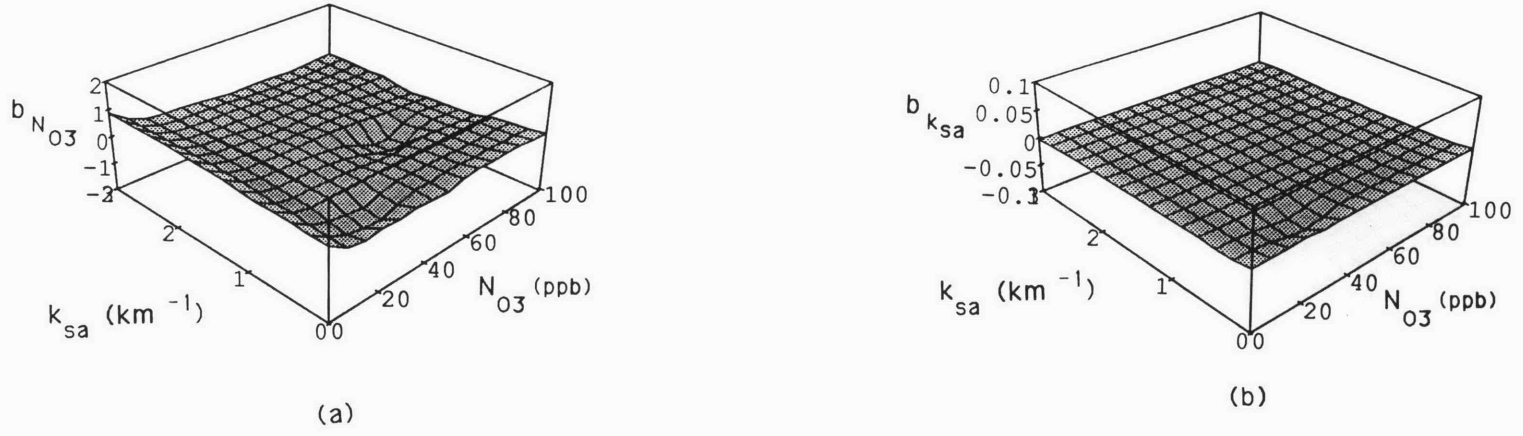

Figure 4-29: Monte Carlo Bias Results for $T_p = 1000\ ns$

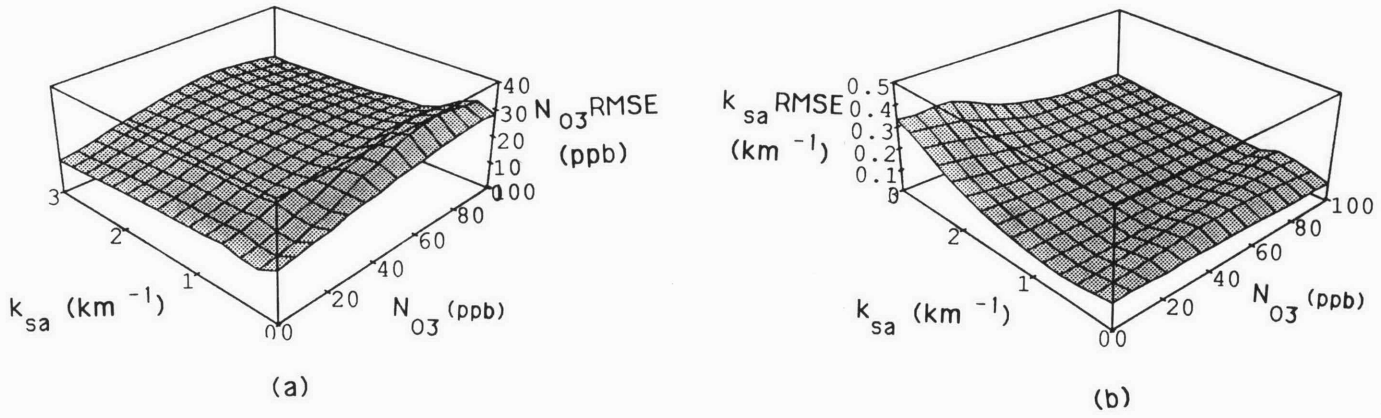

Figure 4-30: Monte Carlo RMS Error Results for $T_p = 10\ ns$

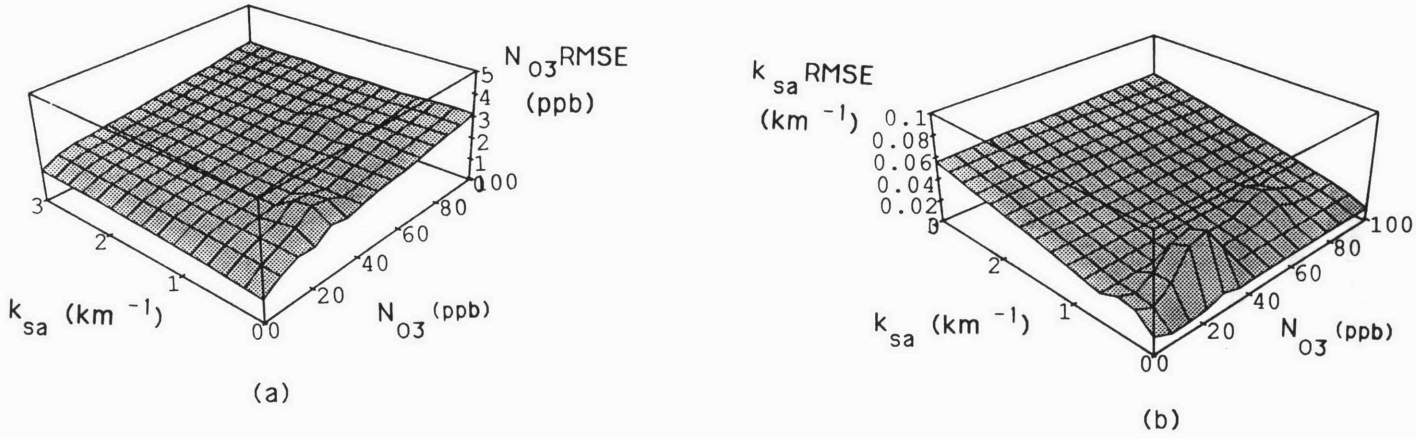

Figure 4-31: Monte Carlo RMS Error Results for $T_p = 1000\ ns$

maritime hazes correspond to $g = 0.78$ [63].

The performance of the estimator for an incorrect choice of g is carried out through the use of Monte Carlo simulations. The photocount data upon which the ML estimator operates is generated using the high, 0.78, or low, 0.67, values of g. The estimator uses this data but assumes that the values of the auxiliary parameters correspond to the base configuration where $g = 0.72$.

Even the relatively small deviations in g from is true value cause the estimator to fail miserably using the initial configuration of the auxiliary parameter set. To obtain decent results, the values is Table 4.13 are employed. The differences between the

$\theta_t = 10°$	$\theta_t = 10°$	$Q_p = 10 \times 10^4$ W
$T_p = 100$ ns	$T_s = 3000$ ns	$T_f = 6000$ ns
$\lambda_{in} = 255$nm	$\lambda_{out} = 315$ nm	$\xi = 0.01$
$g = 0.72$	$f = 0.5$	Area $= 1$ cm^2

Table 4.13: Values for the Auxiliary Parameter Set for Variations in g

values in Table 4.13 and those of the base case are as follows:

- The power in the transmitted pulse, Q_p has been increased from 10^4 Watts to 10×10^4 Watts.
- The beginning of the observation interval has been increased from 180 ns to 3000 ns.
- The ending time of the observation interval has been extended to 6000 ns from 1200 ns

The results of the Monte-Carlo simulations for $g = 0.67$ are presented in Figures 4-32 through 4-35. The bias data is still small and the RMS error results demonstrate that the estimator can be made somewhat robust in the face of unmodeled uncertainty.

Similarly, the results for the $g = 0.78$ case (Figures 4-33 and 4-35) show small bias and acceptable values for the root mean square error in estimates of both N_{O_3} and k_{sa} .

More interesting than the results of the simulations are the required values of the auxiliary parameters needed to obtain these results. First, it is necessary to increase the height of the transmitted pulse by an order of magnitude. Thus, a 10 mJ rather than a 1 mJ pulse is needed. Second the timing of the observation interval is very different from the base case. The observation interval is constructed so as to ignore the initial high rate of backscatter produced by the singularity in Equation 3.15. Furthermore, the the end time of the interval has been greatly extended.

In essence, performance has been maintained by adjusting the content of the observation vector. Photocount data from times close to T_p have been replaced by data from times far from T_p. In other words, the observation vector has been biased in favor of that data which contains the most information about the ozone absorption process. Given the results presented for the other configurations of the auxiliary parameter set, this conclusion is not surprising. The estimates of k_{sa} have been more accurate than those of the ozone number density. Furthermore, altering the values of the auxiliary parameters consistently has had a greater impact (both negatively and positively) on the estimates of N_{O_3} than on the estimates of k_{sa} . Thus, because the estimate of the ozone number density is more sensitive to auxiliary parameter values than the estimates of the aerosol scattering coefficient, it is logical that incorrect choices in these parameter values should require that more information be presented to the estimator concerning the state of the ozone as opposed to the aerosol.

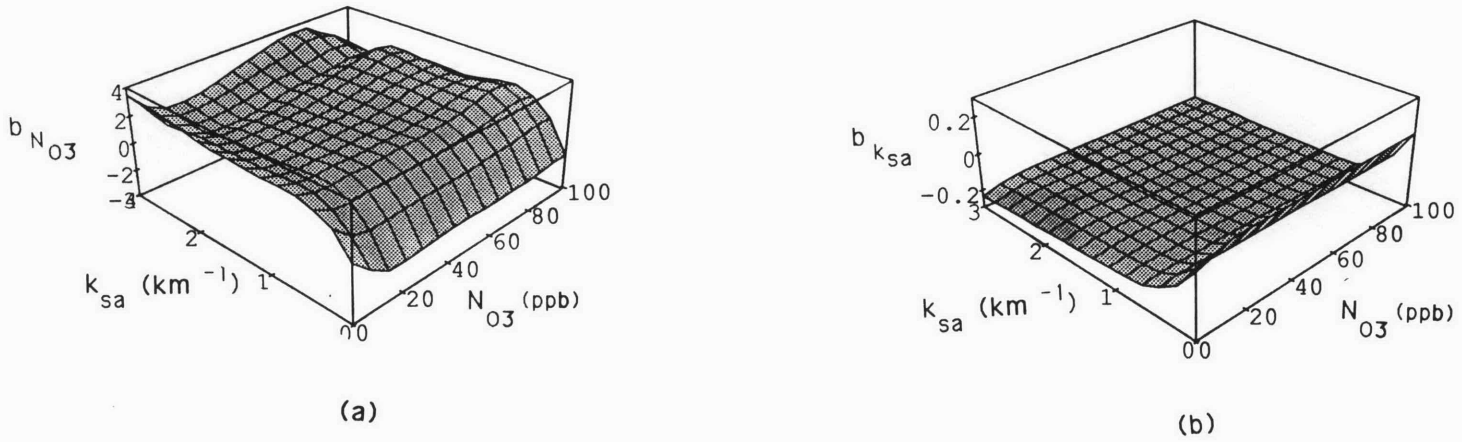

Figure 4-32: Monte Carlo Bias Results for $g_{true} = 0.67$

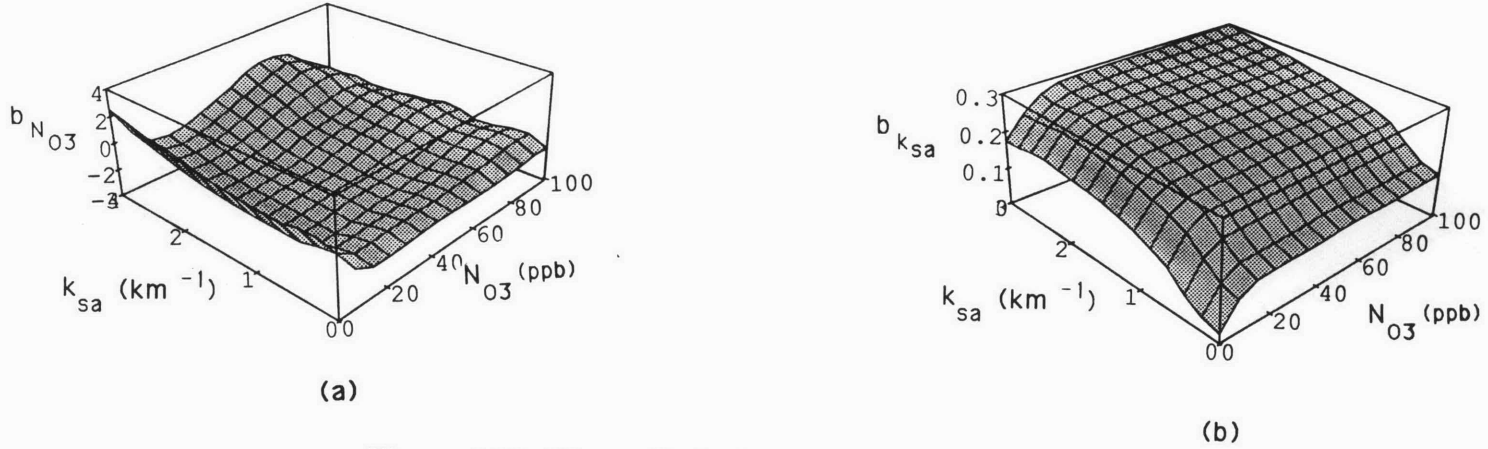

Figure 4-33: Monte Carlo Bias Results for $g_{true} = 0.78$

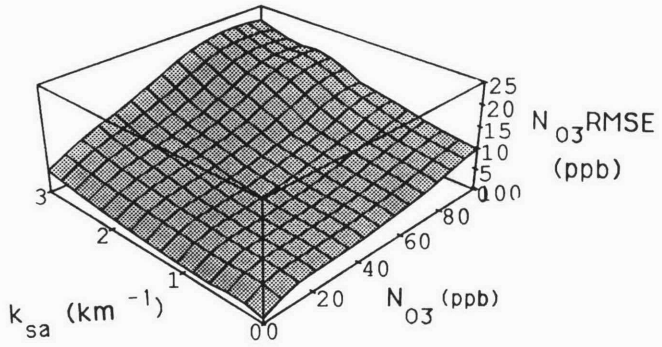

(a)

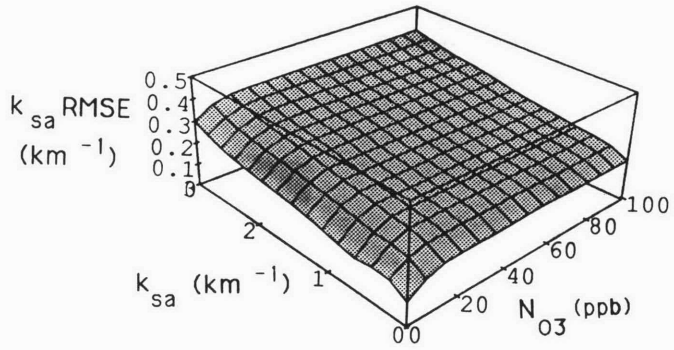

(b)

Figure 4-34: Monte Carlo RMS Error Results for $g_{true} = 0.67$

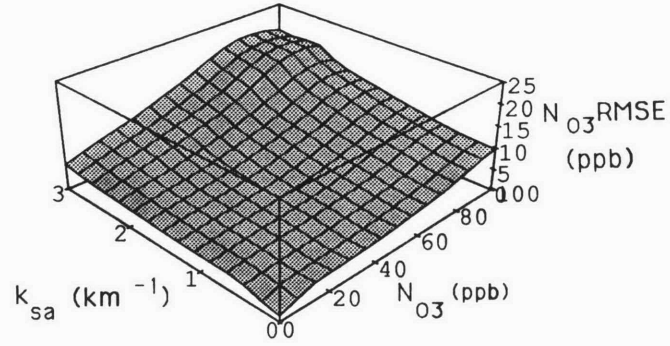

(a)

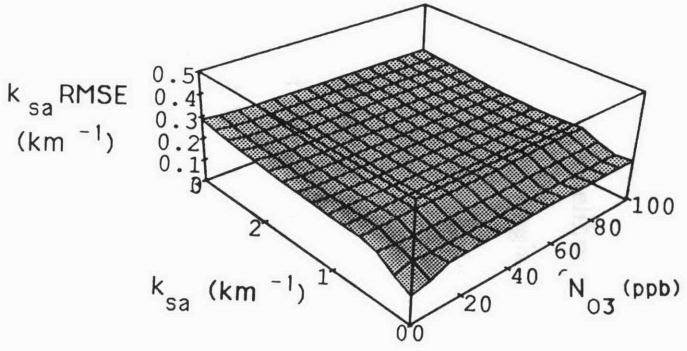

(b)

Figure 4-35: Monte Carlo RMS Error Results for $g_{true} = 0.67$

4.4 Conclusions

Issues associated with the performance of the Maximum Likelihood estimator have been explored in this chapter. Before formal analysis could begin, values for a set of auxiliary parameters associated with the single scatter propagation model were specified. Given this initial configuration, Cramer Rao lower bound and Monte Carlo data were generated and examined as a means of gauging the ability of the ML estimator to ascertain the ozone number density and aerosol scattering coefficient. Finally, the estimator's performance was investigated as the auxiliary parameters were altered in a systematic manner from their base values. While the overall behavior of the ML algorithm was encouraging, further study is warranted to determine the sensitivity of the estimator to unmodeled noise and error sources.

Choices for the initial auxiliary parameter values were motivated by two concerns. On the one hand, the nature of the atmospheric sensing system of which the algorithms are to be a part was the source of some restriction. Additionally, care was taken to ensure that the single scatter assumption was not violated as a result of the chosen parameterization. The resulting configuration had but one difficulty: the expected photocount arrival rate of roughly 10^9 counts/sec may be somewhat high for present detector technology.

Having settled upon a reasonable set of auxiliary parameter values, the performance of the ML estimator was examined. The Cramer Rao lower bound and Monte Carlo data indicated that the ML scheme could easily meet the 20% desired accuracy in the estimates for most points of interest in the $N_{O3} - k_{sa}$ plane. For both N_{O_3} and k_{sa} , the bias was relatively small and the Cramer Rao bound provided an excellent indication as to actual root mean square error behavior.

In Section 4.3.3, two types of parametric analysis were examined. In the first case, auxiliary parameters whose values are controllable by the user were altered from their

base assignments. In the second case, the effects of modeling error on the estimator were explored by creating a discrepancy between the value of an auxiliary parameter assumed in the model and the value used to create the simulated data which acted as input to the ML algorithm.

Variations in the three timing parameters, T_s, T_f, and T_p yielded results which were interpreted easily in light of the physics behind the single scatter propagation model. In general, performance tended to improve as the observation interval was lengthened. The use of a smaller value for the start time of this period aided slightly in the estimation of k_{sa} as increased information concerning the state of the atmospheric aerosol was included in the observation vector. Alternatively, extending T_f lowered the standard deviation in the estimate of N_{O_3} by increasing the quantity of data relating to the ozone. Finally, lengthening both the duration of the pulse and observation end time caused a factor of three improvement in the estimation of the ozone number density.

The effects of modeling error on the estimator were much less encouraging than previous results. Creating a difference between the assumed and true values of the g parameter in the Heney-Greenstein phase function produced disastrous results using the initial configuration of the auxiliary parameter set. Adequate performance could be obtained only by increasing the energy in the transmitted pulse to 10 mJ and extending the observation interval to 6000 ns. While neither of these difficulties are catastrophic[1], the fact that such radical alterations from the initial parameterization were required for a relatively small error in modeling points to problems with the ML estimator.

The sensitivity of the ML estimator to modeling errors may be indicative of diffi-

[1]The 10 mJ pulse is at the high extreme of the energy desired for this atmospheric monitoring system. Further, the optical depths associated with a 6000 ns photon collection period may be pushing the limits of the single scatter model.

culties with the overall system under consideration in this thesis. It may be the case that *any* estimation scheme utilizing data from a low-power, direct-detection monitoring system is not robust to the type of situations analyzed here. In addition to the phase function parameters, it is often the case that the detection efficiency, ξ, is known with only low precision. Furthermore, because photocount noise sources have been absent from the present investigation, the effects of detector shot noise, multiple scatter noise, etc. on performance are unknown. Inclusion of these error factors may require alteration of the estimator in one or both of the following ways:

1. Use of a multiple scatter model to describe atmospheric propagation

2. Expansion of the vector of parameters to be estimated

Only after these additional scenarios have been explored utilizing one or more estimation techniques may a final conclusion be drawn as to the success or failure of the atmospheric monitoring system in determining the transmission parameters of interest in this investigation.

Chapter 5

Recursive Estimation of Atmospheric Transmission Parameters

5.1 Introduction

While the Maximum Likelihood technique provides an effective means of determining model parameters whose values are constant, a rich body of algorithms exists for estimating parameters which are functions of time and space. Recent works by Rye and Hardesty [46, 47] have focused on the application of recursive techniques to problems of Doppler lidar velocity estimation and the determination of the power collected at the receiver of a monostatic lidar system in the presence of additive and multiplicative channel noise. In [58], Warren constructs an adaptive, recursive filter to estimate transmission parameters based on lidar returns in the case where the atmosphere is modeled as an inhomogeneous medium. The goal of this chapter is to explore how one recursive estimation algorithm, the Extended Kalman Filter, may be

applied to the problem of estimating k_{sa} and N_{O_3} when variations of these parameters are strictly temporal.

As in preceding chapters, the atmosphere is assumed to be spatially homogeneous. Thus, the single scatter model developed in Chapter 2 and used in the ML estimator may be employed here as well. Clearly, it is highly unlikely (if not impossible) for the transmission parameters to vary with time and not space. A more realistic situation would have temporal changes accompanied by spatial variations as would arise in the event of a cloud entering and then leaving the atmospheric monitoring system's field of view. In this case however, the assumption of atmospheric homogeneity is removed and modifications to the single scatter model would be required in order to accurately describe the radiative transfer process. Such effort may be of value should the EKF algorithm prove useful in determining N_{O_3} and k_{sa} under the supposition that these parameters vary only with time.

In the instance of time-varying parameters the Maximum Likelihood Estimator still could be used. Assume that pulse pairs are transmitted once every T seconds. The collected photocounts from the i^{th} pair result in a new estimate of the parameter vector, $\underline{\hat{x}}_i$ where each new estimate is made without regard to previous estimates. Over time, it is expected that these estimates would reflect the temporal variation in the actual parameters. While such a system would work, there exist numerous algorithms specially tailored for solving time-varying parameter estimation problems which exploit the relationship between $\underline{x}$ at time i and $\underline{x}$ at times less than i. These techniques are based upon models (called state-space models) which capture the manner in which the parameter vector evolves over time. The consequence of this modeling paradigm is that estimator possesses a recursive structure in that the i^{th} estimate is based upon past estimates as well as data collected during the i^{th} time interval. The most celebrated of these algorithms is the Kalman Filter which is used when the parameter vector of interest is the state vector in a linear state-space model

of the system under consideration. For the problem to be faced in this chapter, the parameter vector is composed of N_{O_3} and k_{sa} which is incorporated into a nonlinear model describing atmospheric transmission. The estimation algorithm to be used in this case is the Extended Kalman Filter (EKF) which is a Kalman Filter built around a linearized form of the non-linear state-space model.

In this chapter, both the theory and performance of the Extended Kalman Filer are examined. First, the state-space model necessary for implementing the EKF is constructed. The temporal variations of N_{O_3} and k_{sa} are assumed to be those of independent first order Gauss-Markov process while the measurements process is based heavily upon the photodetection theory from Section 3.3. Second, the mechanics of the filtering algorithm are briefly discussed. Derivation of this algorithm is not presented here but may be found in [12, 61]. Finally, the ability of the EKF algorithm to determine N_{O_3} and k_{sa} is examined.

5.2 The State Space Model

The implementation of a Kalman Filter or any of its derivatives requires that the parameter vector to be estimated corresponds to a subvector of the state vector in a state-space model of the system under investigation. (It is assumed that the reader is familiar with state-space formulations. Detailed treatments of this topic are found in [12, 61].) For the problem to be addressed here, the state vector, $\underline{x}$, is composed of two elements, N_{O_3} and k_{sa} . In this section, the dynamics equation and observation equation for the state-space model describing the evolution of N_{O_3} and k_{sa} is presented.

5.2.1 The System Dynamics Equation

Under that state-space paradigm, the evolution of the ozone number density and aerosol scattering coefficient is modeled by a state dynamics equation. As discussed in Chapter 2, the state of the atmosphere is dependent upon a host of conditions making exact models of this medium difficult to obtain. For the purposes of implementing a recursive estimation algorithm, such detailed descriptions are unnecessary. In [46] and [47], Kalman filters were designed for Doppler lidar velocity estimation and estimation of lidar power returns using first order Gauss-Markov processes to describe the system dynamics. This model was deemed to be useful due to its simplicity and statistical properties [46]. The first order Gauss-Markov model provides a simple model for describing phenomena where correlation between the variables of interest at times t and s $(s > t)$ is only significant for $s - t < \tau_c$ where τ_c is a constant known as the correlation time. Intuitively it seems logical to believe that to first order, the values of N_{O_3} and k_{sa} at some time s are correlated significantly with previous values only so far into the past. Thus, first order Gauss-Markov models are used to describe the time evolution of the atmospheric transmission parameters.

The dynamic equation for a continuous time first order Gauss-Markov model is of the form:

$$\dot{x}(t) = -ax(t) + bn(t) \tag{5.1}$$

where

$x(t)$ is a 1 dimensional state vector

$n(t)$ is a zero-mean, unit variance, white Gaussian noise process.

a **and** b are two constants related to the correlation structure of the process $x(t)$

It can be shown [12] that $x(t)$ is a zero mean process with correlation function given

by:

$$E[x(t+\tau)x(t)] = K_x(\tau) = \frac{b^2}{2a}e^{-a\tau} \tag{5.2}$$

From Equation 5.2 the constant $1/a$ is taken as the correlation time of the process and $\frac{b^2}{2a}$ is the steady state variance of $x(t)$.

For the problem of determining N_{O_3} and k_{sa} in this thesis, N_{O_3} and k_{sa} are modeled as first order Gauss-Markov processes evolving according to the matrix equation:

$$\begin{bmatrix} \dot{N_{O3}}(t) \\ \dot{k_{sa}}(t) \end{bmatrix} = \begin{bmatrix} -a_{N_{O3}} & 0 \\ 0 & -a_{k_{sa}} \end{bmatrix} \begin{bmatrix} N_{O3}(t) \\ k_{sa}(t) \end{bmatrix} + \begin{bmatrix} b_{N_{O3}} \\ b_{k_{sa}} \end{bmatrix} n(t) \tag{5.3}$$

$$\dot{\underline{x}}(t) = A_c\underline{x}(t) + B_c n(t) \tag{5.4}$$

where the components of A_c and B_c are constants whose values are to be specified at a later point. Because the off-diagonal elements in the A matrix are 0, the two state variables evolve independently of one another.

While the model in Equation 5.4 is given in continuous time, implementation of the EKF requires a discrete time version of this system. Assuming that $\underline{x}(t)$ is sampled once every T seconds, the variations of constants solution to the state dynamics equation for a continuous time, linear, time invariant system gives the state vector at time $(k+1)T$ in terms of the state at time kT for $k = 1, 2, 3, \ldots$ [61]. Letting $\underline{x}(kT) \equiv \underline{x}(k)$ represent the discrete time state vector at time k results in the following first order difference equation:

$$\underline{x}(k+1) = e^{A_c T}\underline{x}(k) + \int_{kT}^{(k+1)T} e^{-A_c[T(k+1)-\tau]}B_c n(\tau)d\tau \tag{5.5}$$

$$= A\underline{x}(k) + \underline{w}(k) \tag{5.6}$$

where

$$A = \begin{bmatrix} e^{-a_{N_{O3}}T} & 0 \\ 0 & e^{-a_{k_{sa}}T} \end{bmatrix} \tag{5.7}$$

and $\underline{w}(k)$ is a discrete time, zero mean white Gaussian noise process with

$$E[\underline{w}(m)\underline{w}(n)^T] = \begin{bmatrix} \frac{b_{N_{O3}}^2}{2a_{N_{O3}}}(1 - e^{-2a_{N_{O3}}T}) & 0 \\ 0 & \frac{b_{k_{sa}}^2}{2a_{k_{sa}}}(1 - e^{-2a_{k_{sa}}T}) \end{bmatrix} \delta(m-n) \tag{5.8}$$

$$= Q\delta(m-n) \tag{5.9}$$

where $\delta(k)$ is the Kronecker delta function.

5.2.2 The Measurement Process

In addition to the state dynamics equation, a state-space model requires an equation describing the measurement, or observations, process which provides the relationship between the state variables and the output of the system. For a discrete time system, a general form of this equation is:

$$\underline{y}(k) = \underline{h}(\underline{x}(k)) + \underline{v}(k) \tag{5.10}$$

where

$\underline{y}(k)$ is the p dimensional vector of observations

$\underline{h}(\underline{x}(k))$ is a p dimensional nonlinear function of the state variables

$\underline{v}(k)$ is a p dimensional discrete white Gaussian noise process with covariance matrix $R(k)$

As with the Maximum Likelihood estimator, the Extended Kalman Filter is to generate estimates of N_{O_3} and k_{sa} based on observations of backscattered photocounts from the atmospheric monitoring systems described in Chapters 2 and 3. Thus, the observations process from Section 3.5.1 provides a basis for constructing the measurement equation to be used here.

From Section 3.5.1, the vector of observations contains $2b$ elements representing the photocounts collected in each of b time intervals associated with 2 transmitted pulses. Furthermore, all members of the observations vector are mutually independent, Poisson random variables with rate parameters given by:

$$\Lambda_{i,j} = \int_{t_{s_{i,j}}}^{t_{f_{i,j}}} \lambda_i(t)dt \tag{5.11}$$

where

$\Lambda_{i,j}$ is the mean and variance of the Poisson process corresponding to the j^{th} observation interval of the i^{th} pulse ($j = 1, 2, \ldots, b$ and $i = 1, 2$)

$t_{s_{i,j}}$ **and** $t_{f_{i,j}}$ are the starting and ending times for the j^{th} observation interval of the i^{th} pulse

λ_i is the Poisson rate function for the i^{th} pulse given by Equation 3.15

To obtain the measurement equation for the state-space model, it is assumed that the Central Limit Theorem may be used to approximate the Poisson random variables described above as Gaussian random variables with equal means and variances. This assumption holds if the number of counts collected in each subinterval is sufficiently high. From the expected count rates for the base configuration of the model given in Table 4.5, it is evident that the CLT approximation is valid. The resulting output

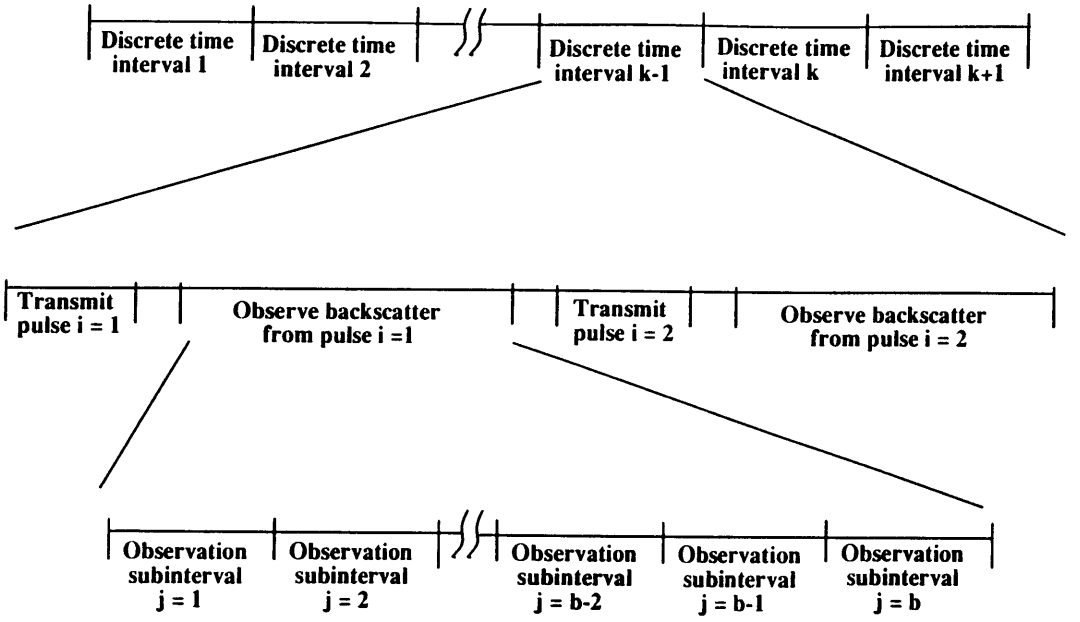

Figure 5-1: Timing Diagram for the Measurement Process

equation is:

$$\begin{bmatrix} y_{1,1}(k) \\ y_{1,2}(k) \\ \vdots \\ y_{1,b}(k) \\ y_{2,1}(k) \\ y_{2,2}(k) \\ \vdots \\ y_{2,b}(k) \end{bmatrix} = \begin{bmatrix} \Lambda_{1,1}(\underline{x}(k)) \\ \Lambda_{1,2}(\underline{x}(k)) \\ \vdots \\ \Lambda_{1,b}(\underline{x}(k)) \\ \Lambda_{2,1}(\underline{x}(k)) \\ \Lambda_{2,2}(\underline{x}(k)) \\ \vdots \\ \Lambda_{2,b}(\underline{x}(k)) \end{bmatrix} + \begin{bmatrix} v_{1,1}(k) \\ v_{1,2}(k) \\ \vdots \\ v_{1,b}(k) \\ v_{2,1}(k) \\ v_{2,2}(k) \\ vdots \\ v_{2,b}(k) \end{bmatrix} \tag{5.12}$$

$$\underline{y} = h(x(k)) + \underline{v}(k) \tag{5.13}$$

where Figure 5-1 is useful in visualizing the physical significance of the following quantities:

$y_{i,j}$ is the number of photocounts observed in the j^{th} observation interval of the i^{th} pulse ($j = 1, 2, \ldots, b$ and $i = 1, 2$)

$\Lambda_{i,j}$ is the expected number of counts for the $(i,j)^{th}$ time interval

$\underline{v}(k)$ a $2p$ dimensional, zero-mean, white Gaussian noise process with a covariance matrix given by:

$$E[\underline{v}(m)\underline{v}(n)^T] = diag[\Lambda_{1,1}(x(k)), \cdots, \Lambda_{2,b}(x(k))]\delta(m-n) \quad (5.14)$$

$$= R(m)\delta(m-n) \quad (5.15)$$

The only difficulty with this observations model is that the covariance of the observation process depends on the state vector; however, $\underline{x}(k)$ is an unknown quantity, To overcome this problem in the implementation of the Extended Kalman Filter, when $R(k)$ is required in a calculation, it is evaluated using the best estimate of $\underline{x}(k)$ available at time k.

5.2.3 Summary

In summary, the state-space model to be used here is given by the following two equations:

$$\underline{x}(k+1) = A\underline{x}(k) + \underline{w}(k) \quad (5.16)$$

$$\underline{y}(k) = h(x(k)) + \underline{v}(k) \quad (5.17)$$

where the matrices A and $\underline{\Lambda}(k)$ are given in Equations 5.7 and 5.12 respectively. The noise process $\underline{w}(k)$ is a zero mean, white, stationary, Gaussian process with covariance matrix Q specified in Equation 5.10. The process $\underline{v}(k)$ is a zero mean, white, non-stationary, Gaussian process with covariance matrix $R(k)$ given by Equation 5.15.

The initial state of the system, $\underline{x}(0)$ is drawn from a Gaussian distribution with mean $\underline{x}_0$ and covariance P_0. Finally, it is assumed that $\underline{w}(k)$, $\underline{v}(k)$, and $\underline{x}(0)$ are mutually independent.

5.3 The Extended Kalman Filter Algorithm

Using a white-noise driven state-space model, the Extended Kalman Filter algorithm is used to generate estimates of the state vector at time k based upon the observations made at time k and the estimate generated at time $k-1$. When the system is modeled by a pair of linear state-space equations, the Kalman Filter produces minimum variance estimates of the state vector with the estimate at any time embodying *all* of the information available from the observations collected from time $k = 0$ to the present. For a nonlinear model, as is the case in this thesis, the Extended Kalman Filter may be viewed as a regular Kalman Filter operating upon a linearized form of the non-linear state-space model. As such, the estimates produced by the EKF are suboptimal in the sense that they do not possess the minimum variance property of the linear Kalman Filter. Despite these characteristics, the Extended Kalman Filter has been chosen for use in this investigation because it is computationally efficient and has been applied successfully to a variety of problems in the fields of guidance and control [27] as well as in the estimation of lidar power returns [47].

The mechanics of the EKF algorithm are best understood by considering Figure 5-2 in conjunction with the following discussion. It is assumed that just after time k, an estimate of the state exists which is based upon the previous $k-1$ measurements. This estimate is denoted as $\underline{\hat{x}}(k|k-1)$[1]. Furthermore, assume that at the same time,

[1]In this thesis, the notation for an estimate at time i based upon data collected through time j is $\underline{\hat{x}}(i|j)$

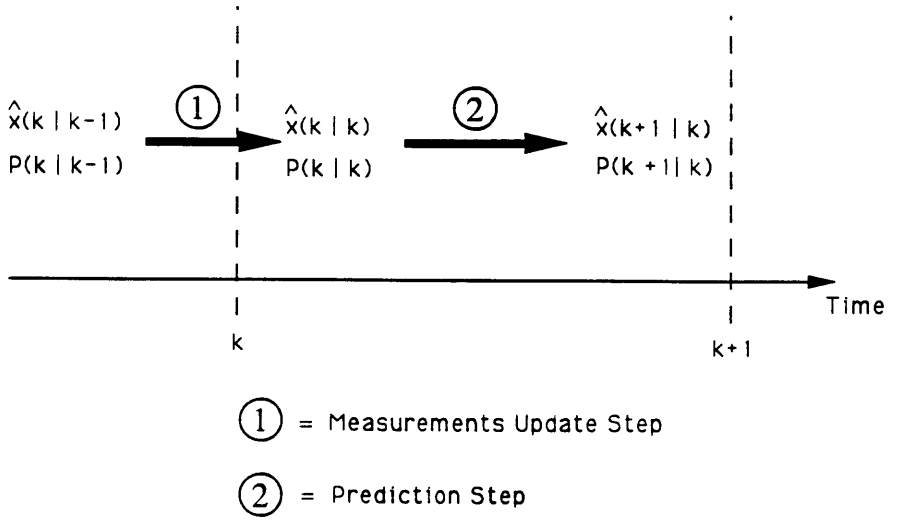

Figure 5-2: Timing Diagram for the Extended Kalman Filter Algorithm

the EKF has computed the one-step error covariance matrix, $P(k|k-1)$ given by

$$P(k|k-1) = E[(\underline{x}(k) - \underline{\hat{x}}(k|k-1))(\underline{x}(k) - \underline{\hat{x}}(k|k-1))^T] \tag{5.18}$$

The Extended Kalman Filter takes these two one-step predicted quantities and uses them in a two step procedure. The first step incorporates the new measurement into the estimate and the error covariance matrix and is given by the following formulae:

$$\underline{\hat{x}}(k|k) = \underline{\hat{x}}(k|k-1) + K(k)[\underline{y}(k) - \hat{h}(k)] \tag{5.19}$$

$$\begin{aligned} P(k|k) &= P(k|k-1) \\ &\quad -P(k|k-1)C^T(k)[C(k)P(k|k-1)C^T(k) + R(k)]^{-1}P(k|k-1) \end{aligned} \tag{5.20}$$

where

- The matrix $K(k)$ is the Kalman gain matrix to be described below

- The vector $\underline{y}(k)$ is the observation obtained at time step k.
- The vector $\hat{h}(k)$ is the expected value of the observation vector at time k based upon the $\underline{\hat{x}}(k|k-1)$ and is given by:

$$\hat{h}(k) = h(x(k))|_{\underline{x}=\underline{\hat{x}}(k|k-1)} \tag{5.21}$$

- The Jacobian matrix, $C(k)$, associated with the function $h(x)$ is given by:

$$C(k) = \begin{bmatrix} \frac{\partial \Lambda_{11}}{\partial N_{O3}} & \frac{\partial \Lambda_{11}}{\partial k_{sa}} \\ \vdots & \vdots \\ \frac{\partial \Lambda_{1b}}{\partial N_{O3}} & \frac{\partial \Lambda_{1b}}{\partial k_{sa}} \\ \frac{\partial \Lambda_{21}}{\partial N_{O3}} & \frac{\partial \Lambda_{21}}{\partial k_{sa}} \\ \vdots & \vdots \\ \frac{\partial \Lambda_{2b}}{\partial N_{O3}} & \frac{\partial \Lambda_{2b}}{\partial k_{sa}} \end{bmatrix} \tag{5.22}$$

  The explicit formulae for the partial derivatives are given in Equations 3.42 and 3.43.

The formula for the gain matrix, $K(k)$, is

$$K(k) = P(k|k-1)C(k)^T[C(k)P(k|k-1)C(k)^T + R(k)]^{-1} \tag{5.23}$$

where the matrix $R(k)$ is the covariance matrix of the observation noise process

After incorporating the new measurements, the second step in the algorithm predicts ahead one time unit so that the filter will be ready to utilize the next measurement. The equations for the prediction step are as follows:

$$\underline{\hat{x}}(k+1|k) = A\underline{\hat{x}}(k|k) \tag{5.24}$$

$$P(k+1|k) = AP(k|k)A^T + Q \tag{5.25}$$

where A is the matrix specified in Equation 5.7 and Q is the covariance matrix of the white noise driving the state dynamics equation.

Finally, this recursive algorithm is begun with initial estimates of the state and error covariance at time $k = 0$. That is, the user starts by specifying the two quantities $\underline{\hat{x}}(0|-1)$ and $P(0|-1)$.

5.4 EKF Testing Procedure

5.4.1 Introduction

As with the Maximum Likelihood estimator, the Extended Kalman Filter is evaluated under a variety of configurations of the auxiliary parameter set. In addition to the parameters described in Section 4.2, the EKF algorithm requires specification of the following parameters found in in the state dynamics model, Equation 5.7:

1. The pulse repetition period: T
2. The parameters $a_{ksa}$and $b_{k_{sa}}$found in the state space description of the aerosol scattering coefficient
3. The parameters $a_{N_{O3}}$and $b_{N_{O3}}$found in the state space description of the ozone number density

The initial configuration of the auxiliary parameters used in Chapter 4 as specified in Table 4.2 is used in the evaluation of the Extended Kalman Filter. The remainder of this section is devoted to (1) specification of the auxiliary parameters given in the above list and (2) a description of the procedure used in the evaluation of the EKF as a tool for estimating atmospheric transmission parameters.

5.4.2 EKF Auxiliary Parameters

In this thesis, the values of the free parameters in the state dynamics equation are determined based on a desire to tune the EKF. Under the assumption that the atmospheric parameters are described accurately by Equation 5.4, rigorous determination of the a_i's and b_i's for $i \in \{N_{O3}, k_{sa}\}$ would require a careful investigation of the true dynamics of the atmosphere. Such an undertaking is beyond the scope of this thesis. Furthermore it is not clear that the the true, detailed dynamics are reflected by the first order Gauss-Markov approach. However, it is hoped that values of $a_{N_{O3}}$, a_{ksa}, $b_{N_{O3}}$, $b_{k_{sa}}$, and T can be chosen so as to achieve adequate performance from the filter.

To simplify matters, the following, arbitrary assignment is made:

$$a_{N_{O3}} = a_{ksa} = 1 \tag{5.26}$$

Furthermore, restrictions imposed by the nature of the transmitter provide an upper bound upon the value for the sampling rate T. It is assumed that the pulse repetition rate of the source used in the transmitter is on the order of kilohertz. Thus, the low value for T is 0.001 seconds. The high value for T is taken as 0.01 seconds in an effort to see how an order of magnitude change in this quantity affects the performance of the estimator.

The choices of $b_{N_{O3}}$and $b_{k_{sa}}$are motivated by a desire to establish the steady state variance of N_{O_3} and k_{sa} . Given that $a_{N_{O3}}$, a_{ksa}, and T have been determined, Equation 5.10 indicates that the standard deviation of the noise for each component of the state vector is directly proportional to the value of the associated b parameter. The values for $b_{N_{O3}}$and $b_{k_{sa}}$provide the filter with *a priori* knowledge concerning the expected behavior of the parameter vector. Because the Equation 5.4 is zero mean, small values for the b_i are interpreted by the filtering algorithm as an indication that the actual value of the state varies little from its mean of zero. Alternatively, large

Parameter	Low Value	High Value	Units
$b_{N_{O3}}$	1.0	10.0	ppb
$b_{k_{sa}}$	0.03	0.30	km^{-1}

Table 5.1: Low and High Values for $b_{N_{O3}}$ and $b_{k_{sa}}$

values of b_i suggest to the filter that the parameters are not necessarily restricted to values close to zero.

By determining the steady state variances, the values of $b_{N_{O3}}$ and $b_{k_{sa}}$ also influence the bandwidth of the Extended Kalman Filter. Higher values of the b_i (i.e. higher steady state variances) should make the filter more responsive to changes in state than lower values because the filter would expect large variability. With this increased responsiveness should come somewhat noisier estimates because the EKF would be more accepting of high frequency noise as honest to goodness signal. On the other hand, lowering the b_i parameters would clamp down on the bandwidth. The filter would reject rapid state changes because it expects the state to remain close to the zero mean value of the Gauss-Markov model. This lower bandwidth leads to smoother estimates but somewhat slower response times due to the fact that high frequency noise as well as high frequency signal components is effectively ignored in a low pass situation.

The values of the b_i parameters are given in Table 5.1. The low value of b_i is taken as 1% of the maximum value of the i^{th} component of the state vector and the high value of b_i is 10% of the maximum value of the i^{th} component of the state vector[2]. Furthermore, these choices for $b_{N_{O3}}$ and $b_{k_{sa}}$ yielded interesting behavior from the simulations.

[2]From Chapter 2 it should be recalled that the maximum assumed value for N_{O_3} is 100 ppb and for k_{sa} is 3 km^{-1}

Run Number	T (s)	$b_{N_{O3}}$ (ppb)	$b_{k_{sa}}$ (km^{-1})	Number of Iterations	Total Time Simulated (s)
1	0.01	1.0	0.03	450	4.5
2	0.01	10.0	0.3	450	4.5
3	0.01	1.0	0.3	450	4.5
4	0.01	10.0	0.03	900	0.9
5	0.001	1.0	0.03	900	0.9
6	0.001	10.0	0.3	900	0.9
7	0.001	1.0	0.3	900	0.9
8	0.001	10.0	0.03	900	0.9

Table 5.2: Auxilary Parameter Configuration for EKF Testing

5.4.3 EKF Testing Procedure

The Extended Kalman Filter is evaluated via simulations involving a variety of configurations of the parameter values specified in the Section 5.4.2. Specifically, there are eight unique combinations of the high and low parameter values for the set $\{T, b_{N_{O3}}, b_{k_{sa}}\}$. Thus, there are eight simulations used to examine the performance of the Extended Kalman Filtering algorithm. The configuration for each of these runs is given in Table 5.2. Note that for the runs where the sampling rate is 0.1 kHz a total of 4.5 seconds of simulation is examined. In the case where the rate is 1 kHz only 0.9 seconds of simulation is presented. Despite these differences, both cases adequately allow for evaluation of the algorithm.

The time functions for the parameters N_{O_3} and k_{sa} are taken to be the step functions as shown in Figures 5-3(a - d). Such profiles permit examination of the filter's performance for steady state situations as well as in the case of sudden changes in the state.

For each of the eight configurations of the parameters, the filter was run 100 times using different photocount data for each iteration. The state estimate at time k is

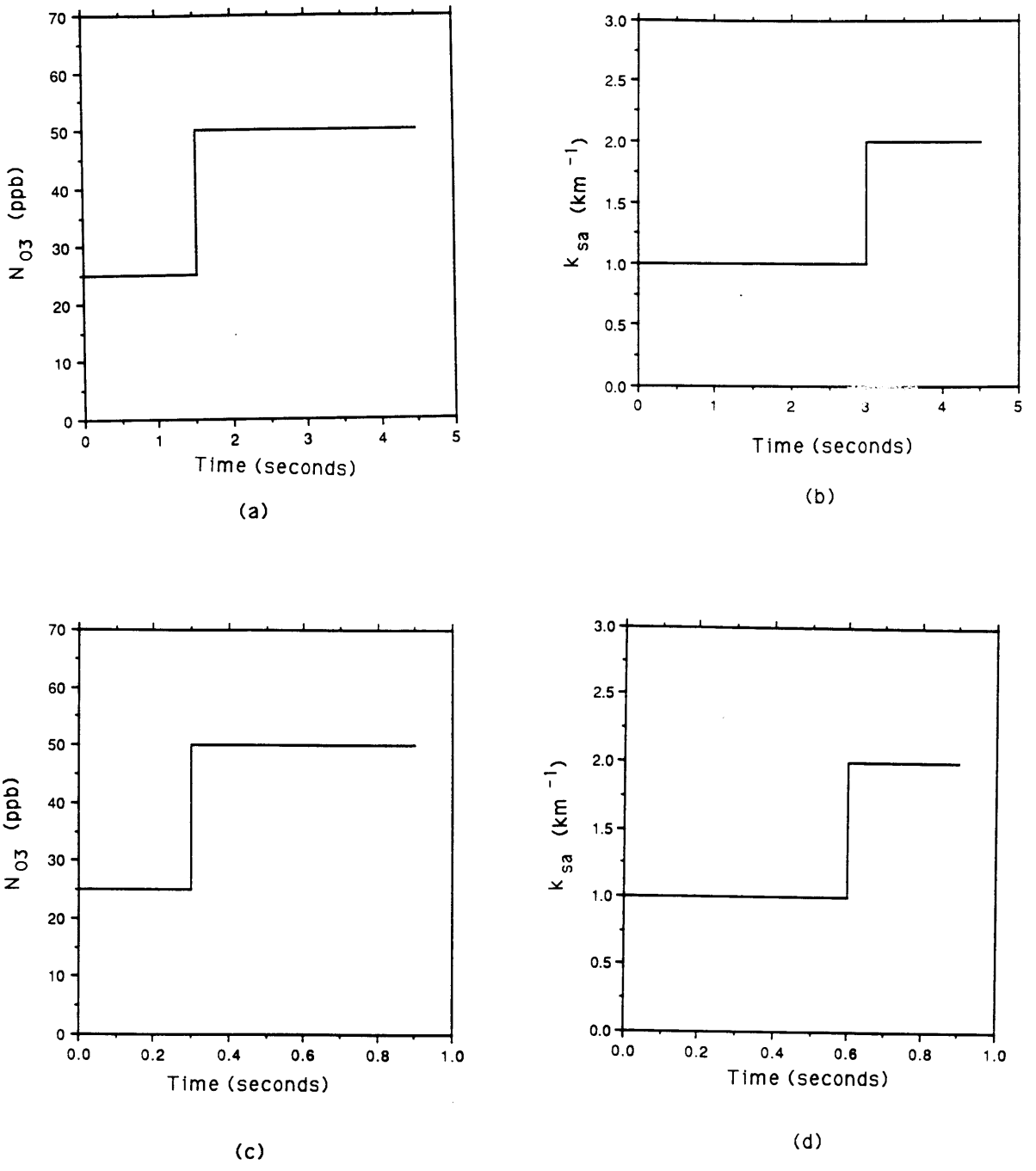

Figure 5-3: Profiles for Ozone Number Density and Aerosol Scattering Coefficient

the average of the estimates generated for each of the 100 iterations:

$$\hat{\underline{x}}(k) = \frac{1}{100}\sum_{i=1}^{100}\hat{\underline{x}}_i(k) \tag{5.27}$$

Finally, the performance is evaluated by examination of the averaged root mean square error of the estimates generated by the algorithm. That is, the quantity $E_{RMS}(k)$ defined as

$$E_{RMS}(k) = \sqrt{\frac{1}{100}\sum_{i=1}^{100}(\hat{\underline{x}}_i(k) - \underline{x}(k))^2} \tag{5.28}$$

is of interest.

In all cases, the filter was initialized according to the following procedure. The initial estimate of the state vector was determined randomly. Specifically, $\hat{N_{O3}}(0|-1)$ and $\hat{k_{sa}}(0|-1)$ were drawn from a Gaussian distribution with mean vector

$$m = \begin{bmatrix} 20 \text{ ppb} \\ 1 \text{ km}^{-1} \end{bmatrix} \tag{5.29}$$

and covariance matrix

$$P = \begin{bmatrix} 40 \text{ ppb}^2 & 0 \\ 0 & 1 \text{ km}^{-2} \end{bmatrix} \tag{5.30}$$

Finally, $P(0|-1)$ was set equal to P in Equation 5.30. This initialization procedure is far from standard and should be altered for future analysis. Most importantly, it may be of use to make the diagonal entries of $P(0|-1)$ much larger. As it stands, the initialization procedure used in this investigation starts the filter with a good guess as to the actual state of the atmosphere.

5.5 Extended Kalman Filter Performance

This section is devoted to analysis of the data obtained from the eight simulations of the EKF under the various configurations of the auxiliary parameter set. The root mean square error results are displayed in Figures 5-4 through 5-11. In examining these cases it is useful to break the eight runs into two groups of four where the first group corresponds to the case of $T = 0.01$ seconds and the second group corresponds to $T = 0.001$ seconds.

For the cases where the sampling rate is 100 Hertz, a few general remarks are in order. From Figures 5-4 through 5-7, some overall trends exist regardless of the exact values for the auxiliary parameters. First, for times sufficiently far after the start of the simulation and sufficiently far after the step, the RMS error settles to a steady state value and this settling process occurs with an exponential-type time dependency. In some sense, the EKF is acting like a low pass filter.

Secondly, in most every case, there exists some degree of coupling between the estimates of N_{O_3} and k_{sa} . This phenomenon is most clearly seen in the estimates of one variable at the time when the other steps. In all cases, the step in one variable causes some disturbance in the estimate of the other variable. The magnitude and duration of the disturbance is dependent upon the exact run.

Finally, $b_{N_{O3}}$and $b_{k_{sa}}$do seem to affect the bandwidth of the EKF in the manner predicted in Section 5.4.2. The lower the value of the b_i, the smoother is the RMS error curve and the slower is the response of the filter to the step. If the filter were a simple one pole low pass filter, such behavior would be indicative of a narrow bandwidth centered about DC. Alternatively, as b_i is raised, the RMS error curves become noisier; however, the decay times after the steps is sharply reduced. Again, in the one pole filter case, this response would indicate a wider bandwidth centered about DC.

Given the above general observations, it is useful to compare Run 1 to Run 2 and Run 3 to Run 4. In Run 1, both $b_{N_{O_3}}$and $b_{k_{sa}}$are set to their low values while in Run 2 both parameters are set to their higher values according to Table 5.2. In these cases, differences in the b values affects the steady state RMS error of the filter. While it was observed that the filter does in fact settle to a steady state after the step, this steady state is not necessarily the true value of the parameter being estimated. For example, in Run 1 the steady state error in k_{sa} is about 0.2 km^{-1} while in Run 2, this value drops to about 0.03 km^{-1}. Similarly, the RMS error in N_{O_3} falls from slightly above 10 ppb to slightly below 2.5 ppb from Run 1 to Run 2. Thus, turning up the magnitude of the white noise driving he state dynamics equation has the effect of increasing, on average, the accuracy of the steady state estimates (at least for the step function case). The only drawback to this is that the RMS error curves for Run 2, are much noisier than their counterparts for Run 1. In both cases however, the steady state error is within 20% of the true value of the corresponding parameter.

The steady state bias effect may be understood by considering the information provided to the filter through the choice of the b_i. The filter believes that both N_{O_3} and k_{sa} are first-order Gauss-Markov processes with means equal to zero and steady state variances given by $b_i^2/2a_i$. Because the $a_i = 1$, the values of $b_{N_{O_3}}$and $b_{k_{sa}}$determine the steady state variances of N_{O_3} and k_{sa} . The variance of a random variable or stochastic process may be interpreted as a measure of inverse information. That is, high variance indicates a certain lack of knowledge concerning the behavior of the process while low variance suggests that the process varies slightly from its mean. Thus, the low values of the b_i cause the EKF to believe that the parameters should be found close to the mean of the first order Gauss Markov models (i.e. close to zero). Information from the observation vector regarding the true, non-zero mean values of N_{O_3} and k_{sa} then is discounted because it contradicts the prior expectation built into the filter via the low b_i. The steady state bias arises as a compromise

between the weights placed on the observations (which tend to increase the values of the estimates) and the prior expectation that the state should be close to zero (which tend to lower the estimates). Alternatively, the higher values of the b_i parameters ameliorate the bias because they are taken by the algorithm as an indication that little is actually known about how N_{O_3} and k_{sa} vary with time. Because the filter is more responsive to the information in the observation vector which conveys the true values of the transmission parameters, the steady state bias is reduced.

For Runs 3 and 4, Figures 5-6 and 5-7 show that mismatching of the $b_{N_{O_3}}$ and $b_{k_{sa}}$ can severely degrade the performance of the Kalman Filter. In each of these runs, one of the b parameters assumes its high value while the other takes on its low value (see Table 5.2). In general, comparison of these plots with the corresponding figures for Runs 1 and 2 show that mismatching the b_i's corrupts performance in the following ways:

1. Increased coupling between the estimates of N_{O_3} and k_{sa} . Compare Figures 5-5(a) and 5-7(a) for an example of this phenomenon.

2. Worsened steady state error (especially for the high b simulations.) Compare the steady state values of k_{sa} in Runs 2 and 3 or the estimates of N_{O_3} in Runs 2 and 4.

While the degradation in the steady state error is not terrible in that the estimates remain within the 20% bound, the increased coupling is rather marked. Thus, based upon these simulations it seems reasonable to conclude that the EKF is best used in a configuration where the noise driving each of the states is of comparable magnitude.

For those simulation corresponding to $T = 0.001$ seconds (Figures 5-7 through 5-11), the results parallel the observations made above for the $T = 0.01$ second case. Qualitatively, the shape of the plots corresponding to identical values of $b_{N_{O_3}}$ and $b_{k_{sa}}$ are roughly identical although the time scales are distinct (the $T = 0.001$ runs

correspond to 0.9 seconds of time while the $T = 0.01$ runs simulate about 4.5 seconds of data.) Thus, the lower T results in faster filter response. Furthermore, the steady state error values are somewhat lower when the sampling period is reduced. The only drawback to the faster sampling rate is that the error at the time of the steps is higher in the cases where $T = 0.001$ seconds.

The improvement in performance due to the faster sampling arises from the fact that more data is made available to the EKF over any given length of time as T decreases. Thus, the time required for the filter to converge to the steady state also will decrease. Finally, aside from the hardware limitations discussed in Section 5.4.2, the sampling rate could not be made arbitrarily small. At some point, the number of photocounts collected in an observation interval would be reduced sufficiently to violate the Central Limit Theorem approximation to the Poisson process used in the construction of the EKF.

5.6 Conclusions

Issues associated with the use of an Extended Kalman Filter as a tool for estimating atmospheric transmission parameters have been explored in this chapter. The chapter began with the construction of a state space model describing the time evolution and method of observation of the parameters N_{O_3} and k_{sa} . Using this model, the recursive algorithm known as an Extended Kalman Filter (EKF) was described. As in the case of the ML Estimator, before actual testing of the EKF could begin, values for a set of auxiliary parameters were determined and a testing procedure was described. Finally, the EKF's performance was investigated via the examination of root mean square error results from each of eight simulations.

The state space model for use with the EKF algorithm consisted of two equations. The state dynamics equation described the manner in which the state vector evolve

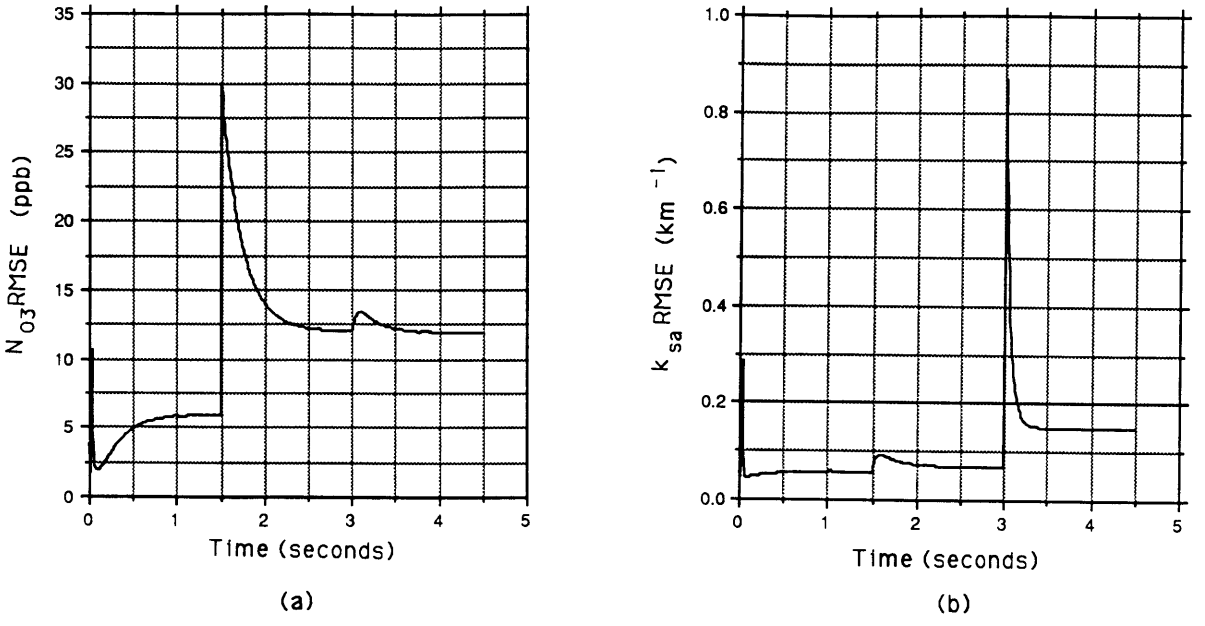

Figure 5-4: EKF Root Mean Square Error Results, Run Number 1

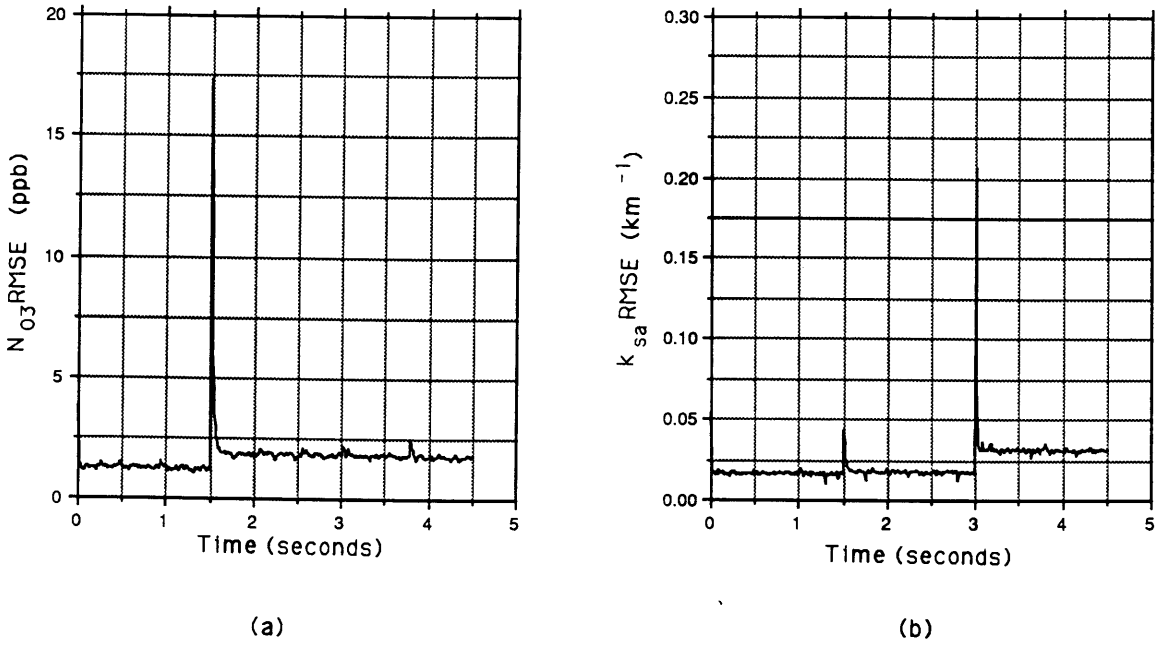

Figure 5-5: EKF Root Mean Square Error Results, Run Number 2

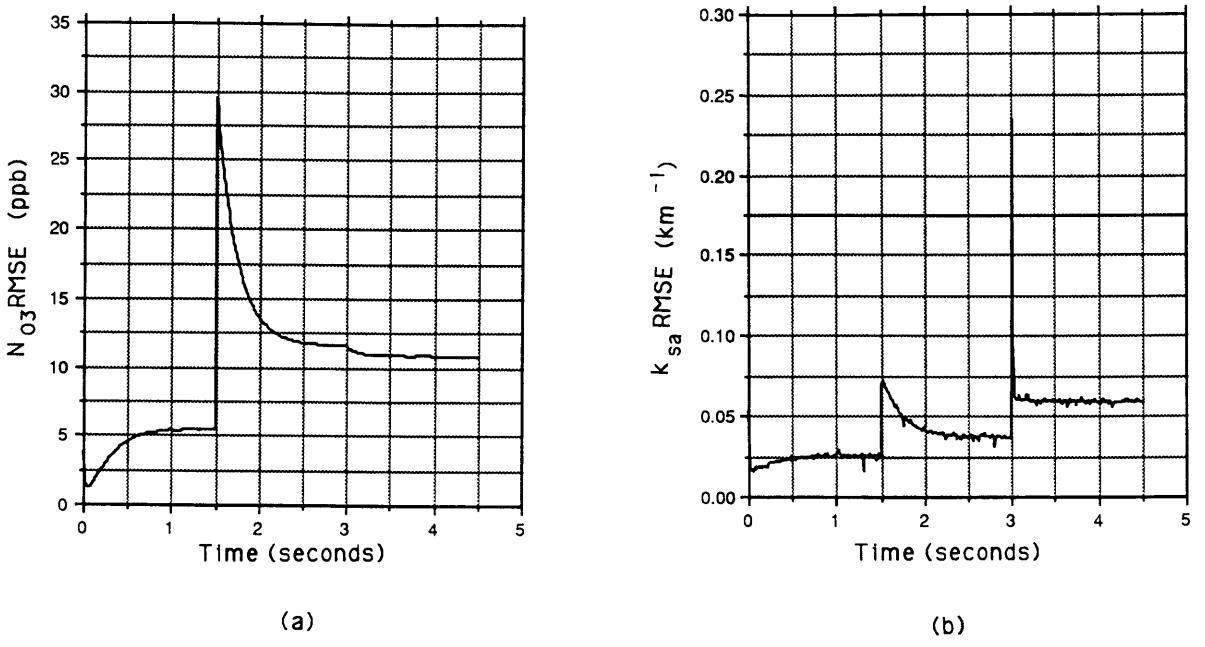

Figure 5-6: EKF Root Mean Square Error Results, Run Number 3

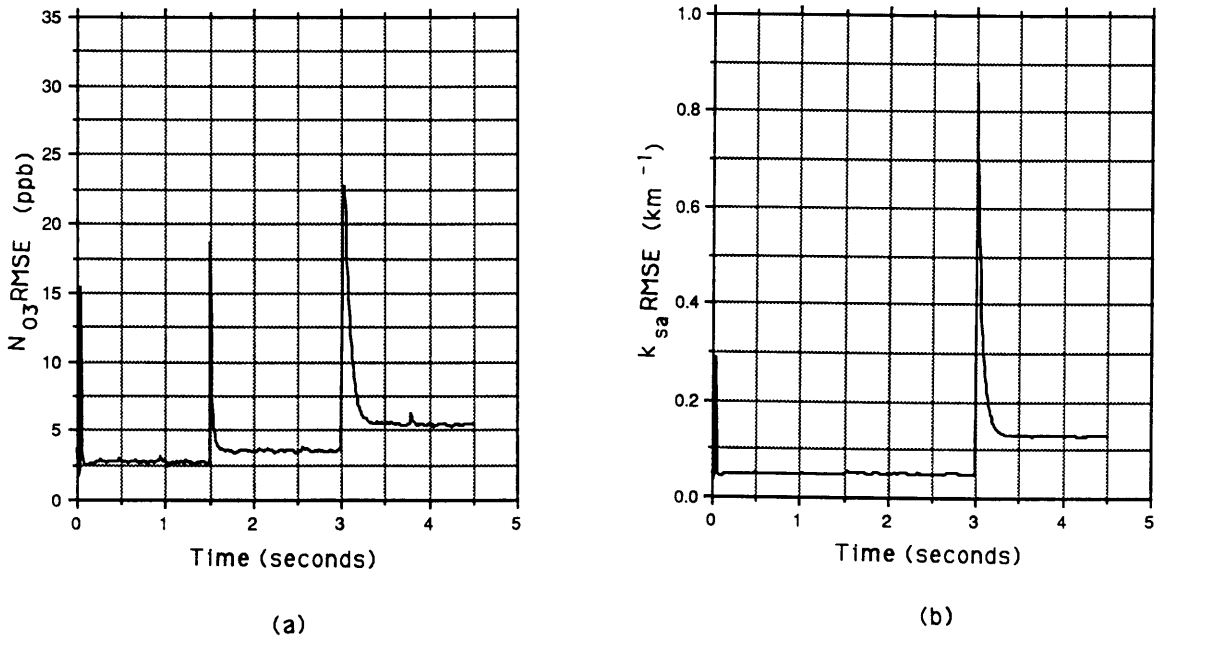

Figure 5-7: EKF Root Mean Square Error Results, Run Number 4

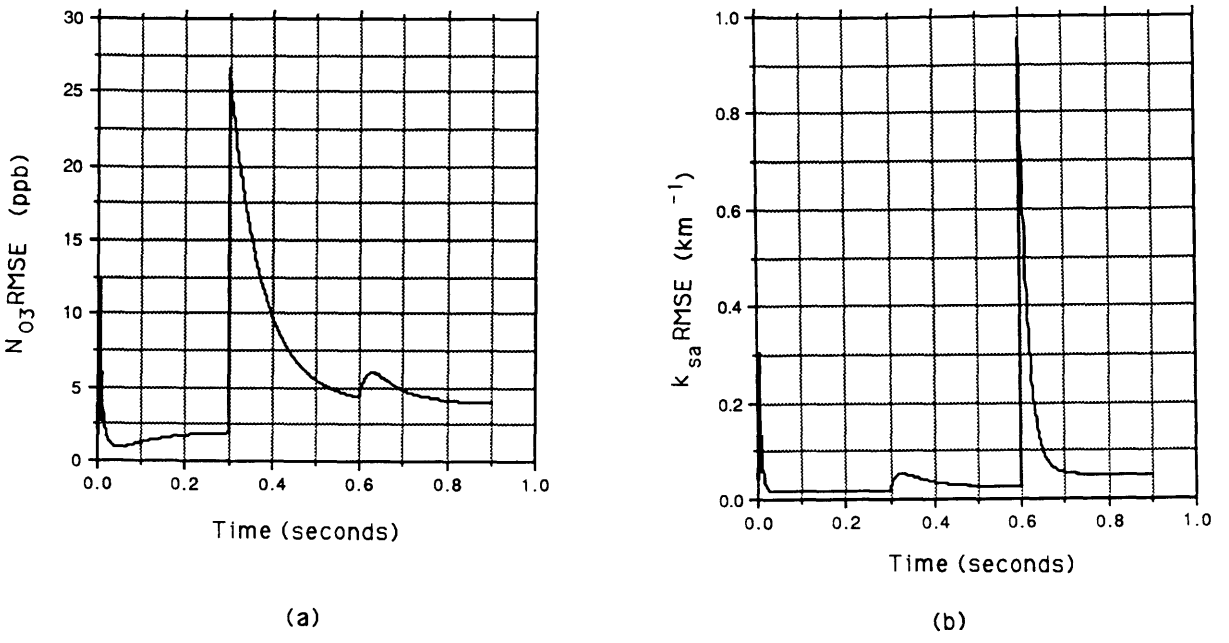

Figure 5-8: EKF Root Mean Square Error Results, Run Number 5

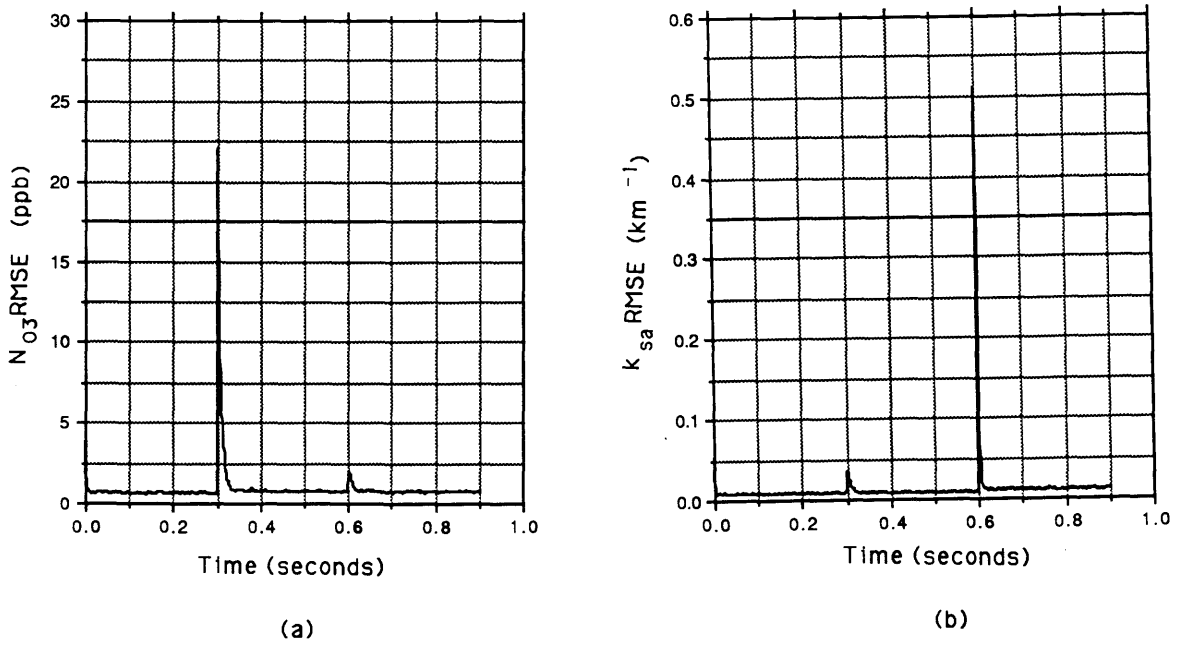

Figure 5-9: EKF Root Mean Square Error Results, Run Number 6

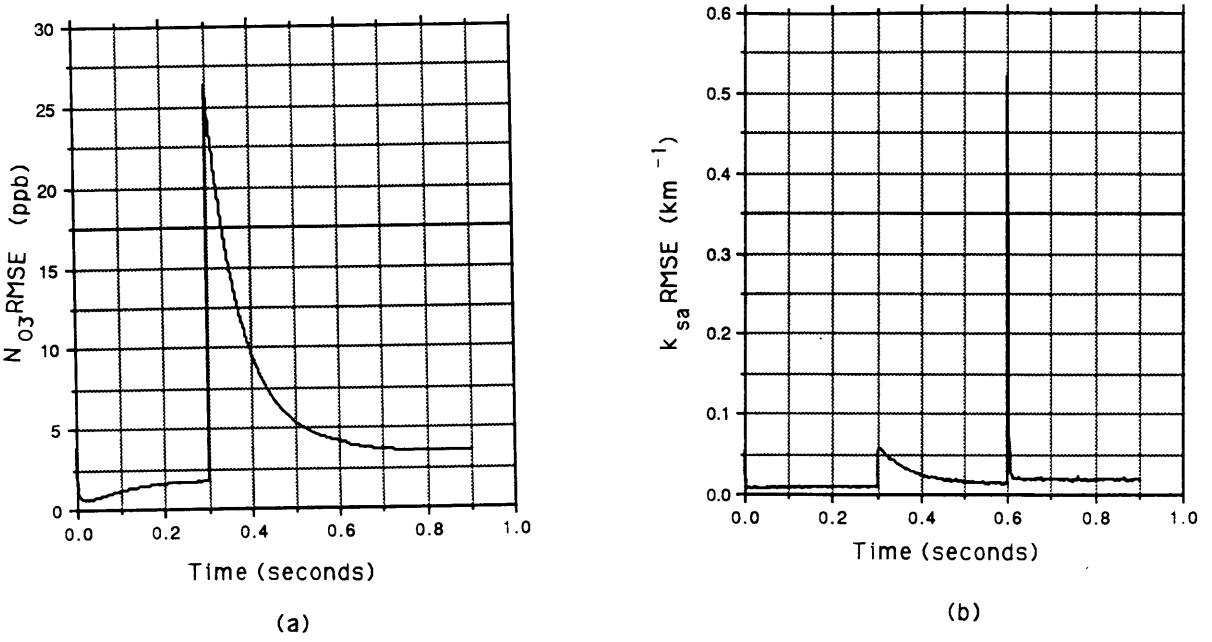

Figure 5-10: EKF Root Mean Square Error Results, Run Number 7

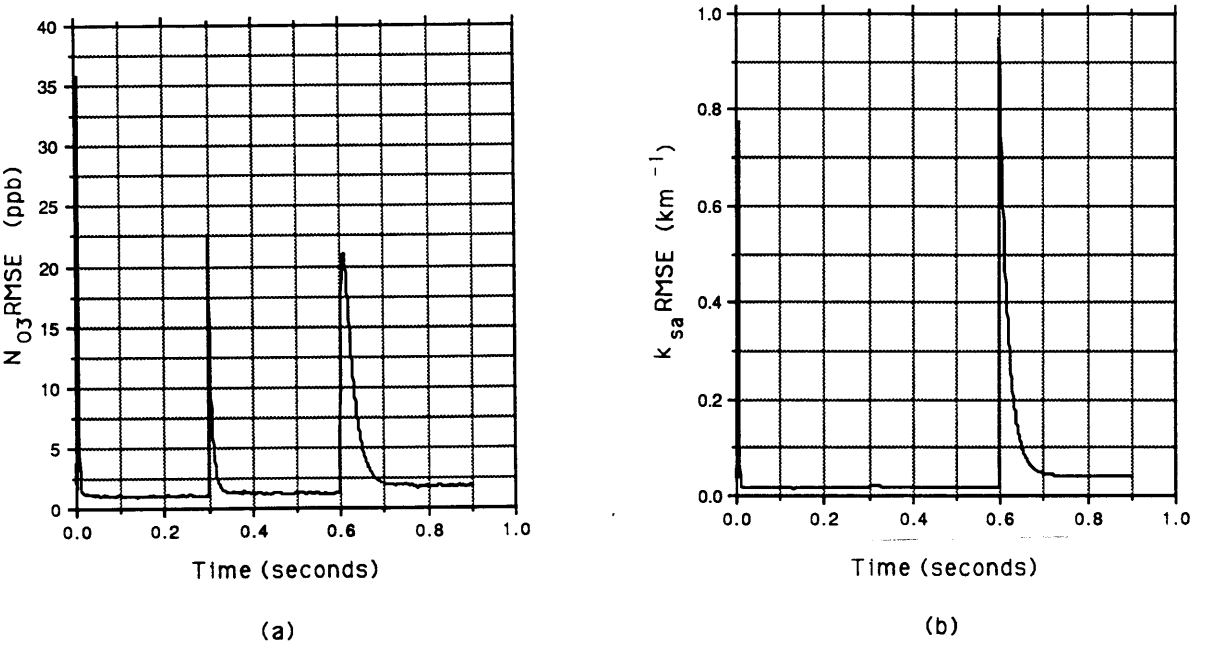

Figure 5-11: EKF Root Mean Square Error Results, Run Number 8

with time. Given no *a priori* model specifying the time dependency of N_{O_3} and k_{sa} and due to the success of other researchers working on related problems, a discrete time first order Gauss-Markov state dynamics equation was developed. The second portion of the model consisted of the measurement equation which determined how the state variables are observed. In this case, a Central Limit Theorem approximation to the Poisson photodetection process explored in Chapters 3 and 4 was employed.

Because the measurement equation is nonlinear in the variable N_{O_3} and k_{sa} , a regular Kalman Filter could not be employed as an estimator. Thus, the Extended Kalman Filter was chosen. While a brief description of the algorithm was presented in this chapter, a more extensive treatment of the EKF can be found in [12, 61].

The auxiliary parameter set for the EKF consisted of the same parameters used in the ML algorithm as well as some additional quantities. Where possible, parameter values used in the initial configuration of the ML estimator were employed in the EKF as well. Where new values were chosen, one of two motivations influenced their specification. In the case of the sampling period, system restrictions associated with the nature of the transmitter placed an upper bound on the pulse repetition rate. For the parameters $a_{N_{O3}}$, $b_{N_{O3}}$, a_{ksa}, and $b_{k_{sa}}$detailed knowledge of atmospheric processes would be needed to obtain accurate values. Lacking such resources, "reasonable" assumptions were made regarding the numerical values assigned these quantities. Clearly, more analysis in this area may useful.

The testing of the Extended Kalman Filter yielded rather encouraging results. In the case where the parameters N_{O_3} and k_{sa} were constant over a long period of time, the steady state values of the estimates were within the 20% desired accuracy. Moreover, abrupt changes in either of the transmission parameters (i.e. step-like variations) resulted in exponential-type responses from the estimator where the decay rate of the exponential can be made quite fast. Finally, the complexity associated with calculating the estimate from the EKF was much lower than was the case with the

ML estimator. Rather than minimizing a complicated non-linear function of N_{O_3} and k_{sa} , each iteration of the EKF required a relatively small number of matrix multiplications and additions as well as a number of function calls to evaluate quantities such as the Jacobian matrix and $h(\hat{x})$, the measurement function evaluated at the current estimate. In the case here of a two dimensional state vector and a ten dimensional observation vector, the most costly matrix vector multiplication required 40 operations (20 multiplies and 20 additions). Alternatively, just to evaluate the log-likelihood function once during the minimization procedure, the ML estimator had to perform a numerical integration which required more computations than the matrix-vector operation described above.

In some respects the performance advantage of the EKF arises from the fact that it is given an inherently less burdensome task than that of the ML estimator. First, the Gaussian approximation to the Poisson process would have reduced the complexity of the optimization problem solved by the ML estimator. Furthermore, each iteration of the EKF is analogous to a single gradient step in an optimization routine so that the very structure of the EKF algorithm makes it inherently less intensive than a single iteration of the ML estimator. Still, given its acceptable performance and its low computational overhead, the Extended Kalman Filter seems to be a better candidate for use in determining the state of the atmosphere than the ML estimator.

Before any solid conclusions may be draw regarding the EKF, additional work is required. First, the performance of the EKF should be examined using more realistic profiles of the parameters N_{O_3} and k_{sa} . Second, the EKF should undergo some robustness analysis similar to that carried out for the ML estimator in Chapter 4. It may be the case here as it was in Chapter 4 that this algorithm is sensitive to modeling errors. Finally, should the EKF still be considered a viable tool it may be useful to consider developing a more accurate dynamics equation in the state space model which may incorporate spatial as well as temporal variation of N_{O_3} and k_{sa} .

Chapter 6

Conclusion

This thesis has explored the application of a variety of statistical estimation techniques to the problem of determining a vector of parameters whose values govern the manner in which propagating radiation interacts with the atmosphere. The investigation was motivated by the belief that knowledge of the state of the atmosphere would have wide application in a variety of contexts including optical communication systems, remote sensing systems, and some position/motion detection systems. The purpose of this chapter is to summarize the results obtained in the body of the thesis and indicate some directions for future effort.

6.1 Thesis Contributions

The first task addressed in this thesis was the construction of an analytical model describing the propagation of radiation through the atmosphere. First, the nature of the atmospheric monitoring system (i.e. the characteristics of the transmitter and receiver) as well as the atmospheric physics relevant to the middle ultra-violet waveband were defined. Next, the propagation equation was formulated where this equation described the power incident upon the receiver as a function of time and

encompassed the set of parameters to be estimated. The form of this model drew heavily upon previous work done by Reilly [43] and Luettgen [27] in the development of single scatter atmospheric pulse responses.

The power incident upon the detector yields a series of voltage pulses as the output of the receiver. The number of pulses observed over a set time interval formed the data set upon which the estimates of the transmission parameters were based. The output of the receiver was modeled as an inhomogeneous Poisson process with a rate function proportional to the power function previously discussed. Given the stochastic model parameterized by the quantities to be estimated, a Maximum Likelihood estimator was explored.

Having settled on a reasonable set of auxiliary parameter values (i.e values for quantities found in the model which were not being estimated), the ML estimator was evaluated based upon Monte Carlo simulations and Cramer-Rao lower bound analysis. It was shown that the bias of the ML estimator was reasonably small in most situations. The Maximum Likelihood estimator also proved to be fairly efficient in that its mean square error was close to the CR lower bound over a wide range of transmission parameter values and configurations of the auxiliary parameter set. Moreover, the RMS error was often well within 20% of the true parameter values. The one drawback to this estimation technique was its sensitivity to modeling errors. Even small errors in assumed values for the auxiliary parameter set caused large degradation in the estimator's performance. Adequate behavior was only regained through a configuration of the auxiliary parameters which may violate the single scatter assumption present in the underlying propagation model. Further work is needed here before strong conclusions may be drawn.

Next, a recursive estimation scheme for estimating the transmission parameters of interest was developed and analyzed. Rather than being mere constants, these quantities were assumed to be functions of time. Their behavior was described via

a state space formulations where the state dynamics equations was taken to be a discrete-time first-order Gauss Markov process and the measurements equation was a Central Limit approximation to the Poisson process developed earlier in the thesis. Given that the observation equation was non-linear in the parameters of interest, an extended Kalman Filter (EKF) was chosen as the recursive estimation algorithm.

The results of the EKF were quite encouraging. The response time of the filter to abrupt changes in the parameters could be made rather fast without violating any modeling or systemic restrictions. Furthermore, in steady state situations where the parameters assumed constant values, the error in the filter was consistently less than 20%. Finally, from a computational standpoint, the EKF was less intensive than the ML estimator and produced comparable if not better results. Thus, this recursive technique would probably be a better choice than the static scheme for actual implementation.

6.2 Future Work

Additional effort on this project is needed in a variety of areas. A multiple scatter propagation model would be beneficial for two reasons. On the one hand, it could be incorporated directly into the estimation schemes. Also, such a model would provide a useful tool for verification of the single scatter model under the variety of circumstances of interest in this thesis.

The vector of estimated parameters should be expanded. This thesis has focused upon the determination of but two quantities describing atmospheric transmission processes: the ozone number density and the aerosol scattering coefficient. As was discussed in Chapter 4, the parameters associated with the aerosol scattering phase function also may be unknown. Thus, it may be useful to estimate the f and g parameters of the Heney-Greenstein phase function. Alternatively, a series represen-

tation of the Mie phase function may be employed so that the first n coefficients are included in the parameter vector. In an effort to gain information regarding the aerosol scattering process at a variety of scattering angles, it may prove advantageous to alter the structure of the receiver/transmitter system and the atmospheric model in the following ways

1. Utilization of a bistatic monitoring system
2. Construction and use of a multiple scatter model
3. Subdivision of the receiver's field of view into an array of pixels and counting photons in each of these spatial bins

Additional scattering and absorption effects may be analyzed. While ozone is the prominent absorber in the middle UV, absorption effects due to other molecular species and aerosols exist and have been ignored throughout this thesis. Further, it may be necessary to explore the properties of specific aerosols rather than settling for knowledge of their composite effects. These additional transmission processes may be most prominent in describing observed photocounts for pulses whose wavelengths lie outside of the ozone absorption band. As with the aerosol phase function, the end result of this analysis may be the expansion of the parameter vector.

Construction of the actual monitoring system would be necessary to obtain real data upon which the algorithms could operate. While the simulations have shown that the performance of the various estimators is encouraging, for the most part, these tests have been performed under the assumption that all facets of the model are correct. As was shown with the ML estimator, errors in modeling can sharply affect the estimator. Thus, real data needs to be obtained for proper verification of the algorithms under investigation.

More extensive evaluation of the EKF algorithm is warranted. Preliminary results have shown that this particular scheme may be a very viable option for actual imple-

mentation; however a firm conclusion cannot be drawn at least until some robustness analysis has been performed. It could be the case here as it was with the ML estimator that modeling errors severely degrade performance in which case some remedy would be required such as inclusion of a subset of the auxiliary parameters in the vector to be estimated. Additional variations on the EKF may include (1) a revised state space model which better reflects the nature of the underlying atmospheric physics including spatial variations of the parameters of interest (2) a second order Kalman filter, (3) an adaptive filter along the lines of Warren [58].

Bibliography

[1] Isam S. Ayoubi and Paul Nelson. Concentration profiles from lidar measurements in the presence of multiple scattering: The two stream approximation. *Applied Optics*, 28(19):4133–4140, 1 October 1989.

[2] Israel Bar-David. Communication under the poisson regime. *IEEE Transactions on Information Theory*, IT-15(1):31–37, January 1969.

[3] Edward V. Browell. Differential absorption lidar sensing of the ozone. *Proceedings of the IEEE*, 77(3):419–432, March 1989.

[4] James H. Churnside. Optical communications through dispersive medium: A performance bound for photocounting. *Applied Optics*, 20(4):573–578, 15 February 1981.

[5] William C. Clark and Edward L. O'Neill. Photoelectron count distributions due to periodic irradiance modulation. *Journal of the Optical Society of America*, 61(7):934–938, July 1971.

[6] Paul Diament and M.C. Teich. Photodetection of low-level radiation through the turbulent atmosphere. *Journal of the Optical Society of America*, 60(11):1489–1494, November 1970.

[7] Paul Diament and M.C. Teich. Photoelectron-counting distributions for irradiance-modulated radiation. *Journal of the Optical Society of America*, 60(2):682–689, May 1970.

[8] Alvin Drake. *Fundamentals of Applied Probability Theory.* McGraw-Hill, 1968.

[9] L. Elterman. UV, visible, and IR attenuation for altitudes to 50 km. Technical report, Air Force Cambridge Research Laboratories, April 1968.

[10] Dr. Ralph Engstrom. *Photomultiplier Handbook: Theory, Design and Application.* RCA Corporation, 1980.

[11] F.X. Kneizys et. al. *Users Guide to LOWTRAN 7.* Air Force Geophysics Laboratory, 16 Auguat 1988.

[12] Gelb. *Applied Optimal Estimation.* MIT Press, 1974.

[13] A.E.S. Green, editor. *The Middle Ultraviolet: Its Science and Technology.* John Wiley and Sons, 1966.

[14] M.Z. Hansen. Atmospheric particulate analysis using angular light scattering. *Applied Optics*, 19(20):3441–3448, 15 October 1980.

[15] Carl W. Helstrom. The minimum variance of estimates in quantum signal detection. *IEEE Transaction on Information Theory*, IT-14(2):234–242, March 1968.

[16] Roderick Hinman. Dynamic range behavior of a microchannel plate detector utilizing a hybrid measurement scheme. Master's thesis, Masachusetts Institute of Technology, 1989.

[17] Estil V. Hoversten, R. O. Harger, and S. J. Halme. Communication theory for the turbulent atmosphere. *Proceedings of the IEEE*, 58(10):1626–1650, October 1970.

[18] Van De Hulst. *Light Scattering From Small Particles.* Dover Press, 1957.

[19] E.C.Y. Inn and Y. Tanaka. Absorption coefficients of ozone in the ultraviolet and visible region. *Journal of the Optical Society of America*, 43, 1953.

[20] Akira Ishimaru. *Wave Propagation and Scattering in Random Media.* Academic Press, 1978.

[21] S. Karp, E. L. O'Neill, and R. M. Gagliardi. Communication theory for the free-space optical channel. *Proceedings of the IEEE*, 58(10):1611–1626, October 1970.

[22] Sherman Karp and John B. Clark. Photon counting: A problem in classical noise theory. *IEEE Transactions on Information Theory*, IT-16(6):672–680, November 1970.

[23] Robert S. Kennedy and Estil V. Hoversten. On the atmosphere as an optical communications channel. *IEEE Transactions on Information Theory*, IT-14(5):716–725, September 1968.

[24] Kenneth F. Klenk. Absorption coefficients of ozone for the backscatter uv experiment. *Applied Optics*, 19(2):236–242, 15 January 1980.

[25] James D. Klett. Stable analytical inversion solution for processing lidar returns. *Applied Optics*, 20(2):211–220, 15 January 1980.

[26] James D. Klett. Lidar inversion with variable backscatter / extinction ratios. *Applied Optics*, 24(11):1638–1643, 1 June 1985.

[27] Mark Leuttgen. Trajectory estimation of optically radiating sources. Master's thesis, Massachusetts Institute of Technology, 1990.

[28] James Scott Linnell. Boundary effects of singly scattered ultraviolet pulses. Master's thesis, Massachusetts Institute of Technology, October 1979.

[29] A.E.S. Green L.M. Garrison, D.D.Doda. Total ozone determination by spectroradiometry in the middle ultraviolet. *Applied Optics*, 18(6):850–855, 15 March 1979.

[30] L.Mandel. Fluctuations of photon beams and their correlations. *Proceedings of the Physics Society*, 72(6):1037–1048, 1958.

[31] L. Mandel. Fluctuations of photon beams. *Proceedings of The Physics Society*, 74(3):233–243, 1959.

[32] L. Mandel and E. Wolf. Coherence properties of optical fields. *Reviews of Modern Physics*, 37(2):231–287, April 1965.

[33] Earl J. McCartney. *Optics of the Atmosphere: Scattering by Molecules and Particles.* John Wiley and Sons, 1976.

[34] N. J. McCormick. Inverse methods for remote determination of properties of optically thick atmospheres. *Applied Optics*, 22(17):2556–2558, 1 September 1983.

[35] I. Stuart McDermid, Sophie M. Godin, and T. Daniel Walsh. Lidar measurements of stratospheric ozone and intercomparisons and validation. *Applied Optics*, 29(33):4914–4923, 20 November 1990.

[36] Raymond M. Measures. *Laser Remote Sensing.* John Wiley and Sons, Inc, 1984.

[37] G. Mengie, Gerard Ancellet, and Jaques Pelon. Lidar measurements of ozone vertical profiles. *Applied Optics*, 19(7):1173–1183, 1 April 1980.

[38] G. Mengie and R.T. Menzies. Complementarity of uv and ir differential absorption lidar for global measurements of atmospheric species. *Applied Optics*, 19(7):1173–1183, 1 April 1980.

[39] John F. Potter. Two-frequency lidar inversion techniques. *Applied Optics*, 26(7):1250–1256, 1 April 1987.

[40] William H. Press, Brian P. Flannery, Saul A. Teukolsky, and William P. Vetterling. *Numerical Recipes.* Cambridge University Press, 1986.

[41] Paul R. Pruncal. Receiver performance evaluation using photocounting cumulants with application to atmospheric turbulence. *Applied Optics*, 19(21):3611–3616, 1 November 1980.

[42] Paul R. Pruncal and Malvin C. Teich. Statistical properties of counting distributions for intensity-modulated sources. *Journal of the Optical Society of America*, 69(4):539–544, April 1979.

[43] D. M. Reilly and C. M. Warde. Atmospheric optical communication in the middle ultraviolet. *Journal of the Optical Society of America*, 69:464–470, 1979.

[44] David Reilly. Atmospheric optical communication in the middle ultraviolet. Master's thesis, Massachusetts Institute of Technology, May 1976.

[45] Warren S. Ross. *Point Source Optical Propagation in a Multiple Scattering Medium.* PhD thesis, Massachusetts Institute of Technology, September 1980.

[46] Barry J. Rye and Michael Hardesty. Nonlinear kalman filtering techniques for incoherent backscatter lidar: Return power and log power estimation. *Applied Optics*, 28(18):3908–3917, 15 September 1989.

[47] Barry J. Rye and Michael Hardesty. Time series identification and kalman filtering techniques for doppler lidar velocity estimation. *Applied Optics*, 28(5):879–891, 1 March 1989.

[48] B. E. Saleh. *Photoelectron Statistics.* Springer-Verlag, 1968.

[49] Takashi Shibata, Terunobu Fukuda, et al. Evaluation of the solar-blind effect in ultraviolet ozone lidar with raman lasers. *Applied Optics*, 26(13):2604–2608, 1 July 1987.

[50] Donald L. Snyder. *Random Point Processes.* John Wiley and Sons, Inc, 1975.

[51] Steven Vincent Sperry. Propagation of ultraviolet light through the lower atmosphere. Master's thesis, Massachusetts Institute of Technology, February 1978.

[52] Wolfgang Steinbrecht, Karl W. Rothe, and Herbert Walther. Lidar setup for daytime and nighttime probing of stratospheric ozone and measurements in polar equatorial regions. *Applied Optics*, 28(17):3616–3624, 1 September 1989.

[53] Malvin C. Teich and Howard C. Card. Photocounting distributions for exponentially decaying sources. *Optics Letters*, 4(5):146–148, May 1979.

[54] Malvin C. Teich, Paul R. Prucnal, and Giovanni Vannucci. Optimum photon detection with a simple counting processor. *Optics Letters*, 1(6):208–210, December 1977.

[55] Malvin C. Teich and Rainfeild Y. Yen. Photon counting receiver performance of multimode laser or scattered radiation. *IEEE Transactions on Aerospace and Electronic Systems*, AES-8(1):13–18, January 1972.

[56] M.C. Teich and S. Rosenberg. Photocounting array receivers for optical communication through the lognormal atmospheric channel. 1: Optimum and suboptimum receiver structures. *Applied Optics*, 12(11):2616–2624, November 1973.

[57] Eli Trakovsky and Uri P. Oppenheim. Determination of aerosol size distribution from observation of the aureole around a point source. *Applied Optics*, 23(7):1003–1008, 1 April 1984.

[58] Russell E. Warren. Detection and discrimination using multiple-wavelength differential absorption lidar. *Applied Optics*, 24(21):3541–3545, 1 November 1985.

[59] Russell E. Warren. Adaptive kalman-bucy filter for differential absorption lidar time series data. *Applied Optics*, 26(22):4755–4760, 15 November 1987.

[60] James A. Weinman. Tomographic lidar to measure the extinction coefficients of atmospheric aerosols. *Applied Optics*, 23(21):3882–3888, 1 November 1984.

[61] Alan S. Willsky. Recursive estimation. Class notes for MIT Course 6.433, 1991.

[62] Alan S. Willsky and Jeffery Shapiro. Stochastic processes, detection and estimation. Class notes for MIT Course 6.432, 1988.

[63] Alexander S. Zachor. Aureole radiance field about a source in a scattering-absorbing medium. *Applied Optics*, 17(12):1911–1922, 15 June 1978.

[64] V. E. Zuev. *Differential Lidar Inversion Techniques.* Springer-Verlag, 1980.

[65] V.E. Zuev, Yu S. Marichev, et al. Lidar differential absorption and scattering technique: Theory. *Applied Optics*, 22(23):3733–3741, 1 December 1983.